Dynamic Nuclear Polarization for Magnetic Resonance Imaging: An In-bore Approach

Dissertation
zur Erlangung des Doktorgrades
der Naturwissenschaften

vorgelegt beim Fachbereich 14
der Johann Wolfgang Goethe-Universität
in Frankfurt am Main

von

Jan G. Krummenacker
aus Völklingen

Frankfurt, 2012

D30

vom Fachbereich 14 der

Johann-Wolfgang Goethe-Universität als Dissertation angenommen.

Dekan: Prof. Dr. Thomas F. Prisner

Gutachter: Prof. Dr. Thomas F. Prisner, Prof. Dr. Laura M. Schreiber

Datum der Disputation:

Contents

Chapter 1

Introduction

Nuclear **M**agnetic **R**esonance ("NMR") is a powerful and versatile technique relying on nuclei that posses a spin. Since its discovery more than 6 decades ago,[1–3] NMR and related techniques has become a tool with innumerable applications throughout the fields of Physics, Chemistry, Biology and Medicine. Numerous Nobel Prizes have been awarded for work in the field[4] and a multi billion dollar industry has developed on its basis.[5,6]

One of NMR's major shortcomings is its inherent lack of sensitivity. Because it relies on the Boltzmann populations of spin states with a minuscule Zeeman splitting, this is particularly true for room temperature experiments. As a result, in an enormous technological effort to enlarge the Zeeman splitting NMR magnets have been moving to higher and higher magnetic fields. However, even for proton spins possessing the largest magnetic moment of all nuclei, the degree of polarization that can be achieved in the strongest spectroscopic magnets available today ($\approx$ 24 T) at room temperature is merely $\approx 8 \cdot 10^{-5}$. In other words, this low polarization theoretically allows a sensitivity enhancement of 10^4 towards full polarization.

Since **M**agnetic **R**esonance **I**maging ("MRI") is based on the same principle, it shares this problem with NMR. Furthermore, for technical and physiological reasons full body MRI tomographs do not reach the magnetic field strengths of spectroscopic NMR magnets, making this even more of an issue for MRI.

In consequence, MRI is chiefly restricted to detecting protons, while both MRI and NMR detection of ^{13}C (or other low γ nuclei) under physiological conditions, i.e. low natural abundance of ^{13}C and a low concentration of the respective substance, suffer from long acquisitions times that are necessary to obtain adequate signal to noise ratios ("SNR").

However, this drawback of NMR can be overcome. The enormous potential sensitivity increase of four orders of magnitude can - at least partially - be exploited by several hyperpolarization techniques, creating entirely new applications and fields of research.
These hyperpolarization techniques comprise chemical approaches like **P**ara-**h**ydrogen **I**nduced **P**olarization ("PHIP")[7–9] or Photo**c**hemically **I**nduced **D**ynamic **N**uclear **P**olarization ("Photo-CIDNP"),[10–12] as well as physical techniques like optically pumped (noble) gases[13,14] or **D**ynamic **N**uclear **P**olarization ("DNP"), which will be the focus of this work. A hyperpolarized substance will render a larger signal without being physically or chemically altered in any other way. It is therefore "marked" without any marker, making it an agent free contrast agent for MRI.

DNP is a technique, in which hyperpolarization of nuclear spins is achieved by microwave ("MW") irradiation of unpaired electron spins in radicals, which are coupled to these nuclei, e.g. ^{1}H, ^{13}C or ^{15}N. The electron spin population is perturbed if the microwave irradiation is resonant with the electron spin transition, which affects the polarization of hyperfine-coupled close nuclei. For large microwave power (i.e. saturating the electron spin transition) the orders of magnitude larger thermal electron spin polarization is effectively transferred to these nuclear spins in the sample. For proton spins the maximum polarization gain amounts to 660, whereas for ^{13}C the sensitivity gain can be as large as 2600. In contrast to e.g. PHIP, which is restricted to specific reaction precursors, DNP is not limited to specific nuclei or hyperpolarization target molecules, making it a very versatile technique.

DNP has been first proposed by Overhauser in 1953,[15] and experimentally observed shortly thereafter in metals[16] and liquids,[17] both being systems with mobile electrons. In the 1960s and 70s, DNP was used as a spectroscopic tool in liquids, thoroughly mapping the effect in the low field regime.[18–21] As well, several other transfer mechanisms were discovered, which are active in the solid state with localized electrons, namely the solid effect[22,23] the cross effect[24,25] and thermal mixing.[26] The theory for all three of these mechanisms predicts reduced transfer efficiencies at higher magnetic fields.[26,27] This fact and the lack of high frequency microwave sources to excite electron spins at magnetic field strengths above 1 T, effectively relegated DNP to a position of an interesting scientific curiosity.[28]
In the early 1990s, DNP came to a renaissance, when DNP was performed at high field in solid state magic angle spinning ("MAS") experiments using high power gyrotron microwave sources.[29,30] This pioneering work sparked a

surge of new developments and applications.[31–34]
As well, this success triggered attempts to investigate also the potential of DNP in the liquid state at high magnetic fields, e.g. at 3.4 T[35–38] and 9.2 T.[39–41] To date, DNP can be considered one of the "hot topics" in the field of magnetic resonance, bringing about special issue in magnetic resonance journals and DNP sections on magnetic resonance conferences.

This thesis deals with the development of an in-bore liquid state DNP polarizer for MRI applications operating in flow through mode at a magnetic field strength of 1.5 T. Following this introductory chapter, the theoretical background necessary to understand and interpret the experimental results is explained in chapter 2. Subsequently, chapter 3 deals with the issue of performing liquid state DNP at high magnetic fields and its challenges. The chapter comprises a quick overview of the necessary hardware, the experimental findings for various samples and the interpretation of these findings, along with the ramifications for the aim of this work. Chapter 4 deals with the issue of increasing sensitivity and contrast in MRI, in particular by means of DNP. The chapter illustrates the development of our polarizer by presenting the hardware that was developed and demonstrating its performance under various conditions. As well, several alternative approaches are introduced and compared to our approach. Finally, chapter 5 summarizes the findings and gives an outlook on further developments.

Chapter 2

Theoretical Background

This chapter briefly introduces the theory behind DNP that is necessary to understand and interpret the DNP data in this thesis. It is comprised of theoretical fundamentals that can be found in numerous textbooks, reviews and publications.[20,42–45] A strong focus will be on DNP in the liquid state, i.e. the Overhauser Effect. This chapter is divided into four parts:
Firstly, a brief introduction into the principles of NMR is given. Secondly, **E**lectron **P**aramagnetic **R**esonance ("EPR") is introduced, since both these fields are of fundamental importance for DNP. Thirdly, the fundamentals of DNP are explained; comprehensively for the Overhauser Effect in the liquid state and as a brief summary for the other DNP mechanisms active in solids, which will not be treated in this thesis. Finally, a short overview into alternative hyperpolarization methods, namely PHIP and optical pumping of noble gases, is given.

2.1 NMR Basics

Any magnetic resonance method, including NMR, is based on the quantum mechanical particle property of *spin*. As Fermions, electrons, neutrons and protons posses a nonzero spin, which is a characteristic constant of each of these particles. A spin with spin angular momentum $\hat{\mathbf{S}}$ has an angular magnetic moment $\hat{\boldsymbol{\mu}}$ associated with it, hence all spin bearing particles also posses and magnetic moment:

$$\hat{\boldsymbol{\mu}} = \gamma \cdot \hat{\mathbf{S}} \tag{2.1}$$

The constant γ is called the *gyromagnetic ratio*, which is characteristic for each kind of particle. Because nuclei consist of protons and neutrons, they also bear a magnetic moment, i.e. the total magnetic moment of the nucleus.

In the special case of the hydrogen atom, this is the spin magnetic moment of the proton.
It is common to rewrite this expression by introducing the g-factor g, e.g. for a nuclear spin commonly denoted by $\hat{\mathbf{I}}$:

$$\hat{\boldsymbol{\mu}}_I = \frac{g\mu_N}{\hbar} \cdot \hat{\mathbf{I}} \quad , \tag{2.2}$$

$\mu_N = \frac{e\hbar}{2m_p}$ being the nuclear magneton, or for a free electron spin commonly denoted by $\hat{\mathbf{S}}$:

$$\hat{\boldsymbol{\mu}}_S = \frac{g\mu_B}{\hbar} \cdot \hat{\mathbf{S}} \quad , \tag{2.3}$$

μ_B being the Bohr magneton.

In a quantum mechanical system the time evolution of the states is given by the *Schrödinger equation*:

$$\partial_t |\Psi(t)\rangle = -i\hat{H}|\Psi(t)\rangle \quad , \tag{2.4}$$

where $|\Psi(t)\rangle$ is the time dependent (spin) state, and $\hat{H}$ is the Hamiltonian. The spin Hamiltonian for sample of nuclei $\mathbf{I}$ in a magnetic field can be written as

$$\hat{H} = \hat{Z}_I + \hat{H}_{RF} + \hat{H}_{chem.} + \hat{H}_{param.} + \hat{H}_{II} + \hat{H}_{quad.} \tag{2.5}$$

with $\hat{Z}_I$ being the nuclear Zeeman term, $\hat{H}_{RF}$ the interaction with an additional oscillating radiofrequency ("RF") field, $\hat{H}_{chem.}$ the chemical shift term, $\hat{H}_{II}$ representing intermolecular dipolar spin-spin interactions and $\hat{H}_{quad.}$ containing quadrupolar interactions.
Only nuclei with a spin quantum number ≥ 1 exhibit a quadrupolar moment $\neq 0$. Within the scope of this thesis, only protons as nuclei with spin $\frac{1}{2}$ will be closely discussed, so $\hat{H}_{quad.}$ will be neglected. Dipolar interactions between different molecules are significantly smaller than electron-nuclear interactions, so the corresponding term $\hat{H}_{II}$ will be neglected as well.[46]
The chemical shift $\hat{H}_{chem.}$ and the paramagnetic shift $\hat{H}_{param.}$ give relatively small contributions and will be discussed later in this chapter. Ignoring these two terms for the moment, one is left with the two external contributions from the static ($\hat{Z}_I$) and the RF field ($\hat{H}_{RF}$).

2.1.1 The Zeeman Term: Thermal Polarization

The nuclear Zeeman part of the Hamiltonian corresponds to the interaction energy of the static magnetic field $\mathbf{B}_0$ with the nuclear magnetic moment $\hat{\boldsymbol{\mu}}_I$:

$$\hat{Z}_I = -\hat{\boldsymbol{\mu}}_I \cdot \mathbf{B}_0 = -\gamma_I \cdot \hat{\mathbf{I}} \cdot \mathbf{B}_0 \tag{2.6}$$

Since $\mathbf{B}_0$ is static, this operator is time independent. Solving 2.4 with the well-known product ansatz renders the stationary Schrödinger equation

$$\hat{\mathbf{H}}|\Psi\rangle = E|\Psi\rangle \quad , \tag{2.7}$$

where $|\Psi\rangle$ is an eigenstate of $\hat{\mathbf{H}}$ and E is the corresponding eigenvalue.
By convention, $\mathbf{B}_0$ is aligned with the z-direction of the laboratory frame of reference: $\mathbf{B}_0 = B_0\mathbf{e}_z$. The Zeeman term of the Hamiltonian can therefore be written as

$$\hat{Z}_I = -\gamma_I B_0 \hat{I}_z \quad . \tag{2.8}$$

In the simple case of a spin $\frac{1}{2}$ nucleus, such as a proton, two eigenstates of $\hat{I}_z$ exist, commonly referred to as the *"up"* and the *"down"* state, often labeled $|+\rangle$ and $|-\rangle$, or $|\uparrow\rangle$ and $|\downarrow\rangle$. They are characterized by the corresponding spin quantum number $|m_I| \leq \frac{1}{2} \Leftrightarrow m_I = \pm\frac{1}{2}$ and feature the corresponding eigenvalues

$$E_m = \gamma_I m_I \hbar B_0 \quad . \tag{2.9}$$

This spin $\frac{1}{2}$ case is analogous to the case of a free electron (see section 2.2). Without a magnetic field, the two spin states are degenerated; they are on the same energy level. By applying $\mathbf{B}_0$ they are split to two energy levels. By defining the *Larmor frequency*,

$$\omega_0 := -\gamma_I \cdot B_0 \quad , \tag{2.10}$$

the expression for the energy gap between the two states, the *Zeeman splitting*, simplifies to

$$\Delta E = E_- - E_+ = \gamma_I \hbar B_0 = \hbar\omega_0 \quad , \tag{2.11}$$

while the Zeeman Hamiltonian now reads as

$$\hat{Z}_I = \omega_0 \hat{I}_z \quad . \tag{2.12}$$

Entering the Zeeman term 2.12 into the Schrödinger equation 2.4 yields the explicit time evolution: The spin state is *rotated* around the z-axis (i.e. the direction of the magnetic field $\mathbf{B}_0$) with angular frequency ω_0:

$$|\Psi(t+\tau)\rangle = \hat{R}_z(\omega_0\tau)|\Psi(t)\rangle \quad , \tag{2.13}$$

$\hat{R}_z(\phi) = \exp\left(-i\phi\hat{I}_z\right)$ being the rotation operator around z.
In a typical NMR sample, one deals not with one spin, but with $\approx 10^{22}$ spins - an *ensemble* of spins. To describe a quantum mechanical system this large, the *density operator* is introduced

$$\hat{\rho} := \overline{|\psi\rangle\langle\psi|} \quad , \tag{2.14}$$

where the overbar indicates the average over all spins in the ensemble. It is commonly written as a *density matrix*, by expressing the states $|\psi\rangle$ as a vector $\begin{pmatrix} c_+ \\ c_- \end{pmatrix}$ in the vector space spanned by $|+\rangle$ and $|-\rangle$. It therefore reads as

$$\hat{\rho} = \begin{pmatrix} \rho_{++} & \rho_{+-} \\ \rho_{-+} & \rho_{--} \end{pmatrix} = \begin{pmatrix} \overline{c_+ c_+^*} & \overline{c_+ c_-^*} \\ \overline{c_- c_+^*} & \overline{c_- c_-^*} \end{pmatrix} \quad . \tag{2.15}$$

The diagonal elements ρ_{++} and ρ_{--} are the (normalized) *populations* of the states $|+\rangle$ and $|-\rangle$, while the off-diagonal elements ρ_{+-} and ρ_{-+} are called the *coherences* between $|+\rangle$ and $|-\rangle$.
In thermal equilibrium, the two states are populated according to the *Boltzmann distribution*:

$$\begin{aligned} \rho_{++} &= \frac{\exp\left(\frac{1}{2}\beta\hbar\omega_0\right)}{\exp\left(\frac{1}{2}\beta\hbar\omega_0\right) + \exp\left(-\frac{1}{2}\beta\hbar\omega_0\right)} \qquad \text{and} \\ \rho_{--} &= \frac{\exp\left(-\frac{1}{2}\beta\hbar\omega_0\right)}{\exp\left(\frac{1}{2}\beta\hbar\omega_0\right) + \exp\left(-\frac{1}{2}\beta\hbar\omega_0\right)} \end{aligned} \tag{2.16}$$

with $\beta = \frac{1}{k_B T}$, k_B being the Boltzmann constant and T the absolute temperature.
By expanding the exponential around 0 to the first order in $\beta\hbar\omega_0$ renders:

$$\begin{aligned} \rho_{++} &= \frac{1}{2} + \frac{1}{4}\beta\hbar\omega_0 \qquad \text{and} \\ \rho_{--} &= \frac{1}{2} - \frac{1}{4}\beta\hbar\omega_0 \quad , \end{aligned} \tag{2.17}$$

which is called the *high temperature approximation*. It is valid for $\beta\hbar\omega_0 \ll 1 \Leftrightarrow k_B T \gg \hbar\omega_0$, which for typical NMR field strengths gives a validity to very low temperatures in the range of a few Kelvin. This is reflected in tiny thermal polarization values: At room temperature and 9.2 T field strength, corresponding to a typical 400 MHz ^{1}H-NMR magnet, the thermal polarization of the protons is merely $5 \cdot 10^{-6}$! This is an inherent feature of NMR and one of its biggest problems and will be addressed later.
The population difference is schematically depicted in an energy level diagram in figure 2.1:

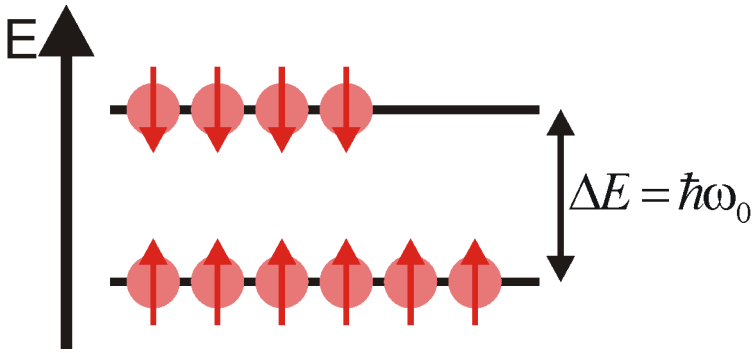

Figure 2.1: Energy level diagram of a (nuclear) spin $\frac{1}{2}$ system in an external magnetic field. The red balls and arrows depict the Boltzmann populations of the respective spin states. This figure is not drawn to scale.

2.1.2 Magnetization

The fact that there is a population difference between the two states means that in the presence of the static magnetic field, there is a net polarization of the ensemble of spins - and thus a net magnetization. Therefore, from a macroscopic point of view regarding the ensemble of (isolated) spins one can indicate the direction and magnitude of this net magnetization by defining the *magnetization vector*. This is most convenient in the *rotating frame*; the frame of reference rotating around the z-direction of the laboratory frame of reference at angular frequency ω, i.e. in the Heisenberg picture:

$$\tilde{\mathbf{M}} := \tilde{M}_x\tilde{\mathbf{e}}_x + \tilde{M}_y\tilde{\mathbf{e}}_y + \tilde{M}_z\tilde{\mathbf{e}}_z \quad , \tag{2.18}$$

with

$$\begin{aligned}
\tilde{M}_x &= 4 \cdot \frac{1}{\beta\hbar\omega_0} Re(\tilde{\rho}_{-+}) \\
\tilde{M}_y &= 4 \cdot \frac{1}{\beta\hbar\omega_0} Im(\tilde{\rho}_{-+}) \\
\tilde{M}_z &= 2 \cdot \frac{1}{\beta\hbar\omega_0} (\rho_{++} - \rho_{--}) \quad .
\end{aligned}$$

Note that in this definition the magnetization vector is normalized, so for the thermal equilibrium

$$\tilde{\mathbf{M}}^{eq} = \tilde{\mathbf{e}}_z = \mathbf{e}_z \quad . \tag{2.19}$$

2.1.3 The RF Term: Manipulation of Magnetizations

When a radiofrequency field is applied, i.e. $\hat{H}_{RF} \neq 0$, the spins experience and are influenced by the magnetic component of the RF field. Usually, this is done for a short period of time, yielding an RF *pulse*. The Hamiltonian during a pulse at the angular frequency ω applied along the x-axis of the laboratory frame with phase ϕ_{ph} can be written as

$$\hat{H} = \hat{Z}_I + \hat{H}_{RF}(t) = \omega_0 \hat{I}_z - \frac{1}{2}\gamma_I B_1 \left(\cos(\omega t + \phi_{ph}) \cdot \hat{I}_x + \sin(\omega t + \phi_{ph}) \cdot \hat{I}_y\right) \quad , \tag{2.20}$$

where B_1 is the peak intensity of the magnetic component of the RF field. This can be rewritten to

$$\hat{H}_{RF}(t) = -\frac{1}{2}\gamma_I B_1 \hat{R}_z/(\omega t + \phi_{ph}) \hat{I}_x \hat{R}_z/(-\omega t - \phi_{ph}) \quad ,$$

which yields for the Hamiltonian in the rotating frame, which now corresponds to the interaction picture,

$$\hat{\tilde{H}} = (\omega_0 - \omega)\hat{I}_z + \omega_1 \left(\hat{I}_x \cdot \cos(\phi_{ph}) + \hat{I}_y \cdot \sin(\phi_{ph})\right) \quad , \tag{2.21}$$

with the *nutation frequency* defined as

$$\omega_1 := |\frac{1}{2}\gamma_I B_1| \quad . \tag{2.22}$$

For an RF pulse at angular frequency $\omega = \omega_0$ for a pulselength τ_{pulse} and choosing a phase $\phi_{ph} \stackrel{!}{=} 0$ ("x-pulse") propagating a spin state renders

$$|\tilde{\Psi}(t + \tau_{pulse})\rangle = \hat{R}_z(\theta_{pulse})|\tilde{\Psi}(t)\rangle \quad , \tag{2.23}$$

containing the definition of the *flip angle*

$$\theta_{pulse} := \omega_1 \tau_{pulse} \quad . \tag{2.24}$$

The value of the flip angle can be set to a desired value, e.g. 90° (or $\frac{\pi}{2}$), by choosing an appropriate pulselength τ_{pulse} and ω_1, i.e. power. The pulse defined above with $\phi_{ph} \stackrel{!}{=} 0$ and flip angle $\theta_{pulse} \stackrel{!}{=} \frac{\pi}{2}$ is called a "$\frac{\pi}{2}$-pulse in x" and commonly written as $\left(\frac{\pi}{2}\right)_x$

In a similar fashion as in equation 2.23, if one now considers this pulse acting on the ensemble of spins, it comes down to propagating the density matrix instead of a single state. This gives us access to calculate the effect of the RF pulses on the magnetization 2.18:

A $\left(\frac{\pi}{2}\right)_x$-pulse acting on the thermal equilibrium magnetization 2.19 will *rotate* $\mathbf{M}^{eq} = \tilde{\mathbf{e}}_z$ by the flip angle $\theta_{pulse} = \frac{\pi}{2}$, into the x-y-plane: $\mathbf{M}^{eq} = \tilde{\mathbf{e}}_z \xrightarrow{\left(\frac{\pi}{2}\right)_x} -\tilde{\mathbf{e}}_y$. This is depicted in figure 2.2.
In a nutshell, the RF pulse can be used to *manipulate* the magnetization. This is a very important feature which can be exploited to perform NMR (and analogously EPR) experiments.

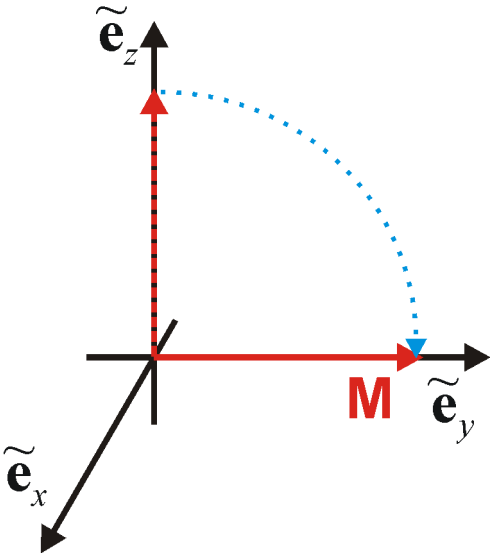

Figure 2.2: Effect of a $\left(\frac{\pi}{2}\right)_{-x}$-pulse acting on the thermal equilibrium magnetization $\mathbf{M}^{eq} = \mathbf{e}_z$, turning it into the direction of $\tilde{\mathbf{e}}_y$, i.e. into the x-y-plane.

In an analogous fashion to the $\left(\frac{\pi}{2}\right)_x$-pulse, a $(\pi)_x$-pulse will *invert* the magnetization vector $\mathbf{M}^{eq} = \tilde{\mathbf{e}}_z \xrightarrow{(\pi)_x} -\tilde{\mathbf{e}}_z$, along with the populations. Such a pulse is therefore also referred to as an *inversion pulse*.

2.1.4 The Bloch Equations

While the RF induces a nutation of the spins and thus can be used to manipulate the magnetization of the ensemble, the magnetization also propagates when the RF field is turned off. This is properly described by propagating the density matrix using the appropriate Hamiltonian $\hat{H} = \hat{Z}$.
However, it can also be described - in a semiclassical fashion - by starting from the (classical) interaction between the magnetization $\mathbf{M}$ and the static magnetic field $\mathbf{B}_0$:

$$\partial_t \mathbf{M} = \gamma_I \cdot \mathbf{M} \times \mathbf{B}_0 \quad . \tag{2.25}$$

this yields for the individual components

$$\begin{aligned} \partial_t M_x &= \gamma_I \left(M_y B_0 + M_z B_1 \sin \omega_0 t \right) \\ \partial_t M_y &= \gamma_I \left(M_z B_1 \cos \omega_0 t - M_x B_0 \right) \\ \partial_t M_z &= \gamma_I \left(-M_x B_1 \sin \omega_0 t + M_y B_1 \cos \omega_0 t \right) \quad , \end{aligned} \tag{2.26}$$

which is identical to the result from the propagation method.
In 2.26 relaxation processes can be added phenomenologically by introducing relaxation terms: Firstly the *spin-lattice relaxation* with a term containing the spin-lattice or *longitudinal* relaxation time T_1 and secondly the *spin-spin relaxation* with terms containing its characteristic *transversal* relaxation time T_2, rendering the *Bloch equations*

$$\begin{aligned} \partial_t M_x &= \gamma_I \left(M_y B_0 + M_z B_1 \sin \omega_0 t \right) - \frac{M_x}{T_2} \\ \partial_t M_y &= \gamma_I \left(M_z B_1 \cos \omega_0 t - M_x B_0 \right) - \frac{M_y}{T_2} \\ \partial_t M_z &= \gamma_I \left(-M_x B_1 \sin \omega_0 t + M_y B_1 \cos \omega_0 t \right) - \frac{M_z - M_0}{T_1} \quad , \end{aligned} \tag{2.27}$$

where M_0 denotes the thermal equilibrium value of the magnetization. T_1 is the characteristic time with which the magnetization relaxes back to its thermal equilibrium value and aligns back with $\mathbf{B}_0 || \tilde{\mathbf{e}}_z = \mathbf{e}_z$, while T_2 is the characteristic time with which coherence between the spins of the ensemble is lost.

2.1.5 NMR Experiments

The magnetization of the ensemble of spins is a macroscopic property, so its precession and relaxation following equations 2.27 can be externally detected. If a coil is placed around the sample (containing the ensemble), the precessing magnetization will induce a voltage, oscillating with the Larmor frequency of the precession. This signal is recorded and for technical reasons convert ed down with the spectrometer reference frequency ω. In NMR usually the same coil used for transmitting the RF field into the sample and picking up the induced signal.
The simplest (Fourier Transform-) NMR experiment is to first apply a $\left(\frac{\pi}{2}\right)_x$-pulse and then record the induced signal. The $\left(\frac{\pi}{2}\right)_x$-pulse will rotate the magnetization into the x-y-plane, where it will precess with the Larmor frequency and decay exponentially as described by equations 2.27. The decaying signal from the magnetization is called the *free induction decay*, short FID.

This experiment is depicted in figure 2.3.

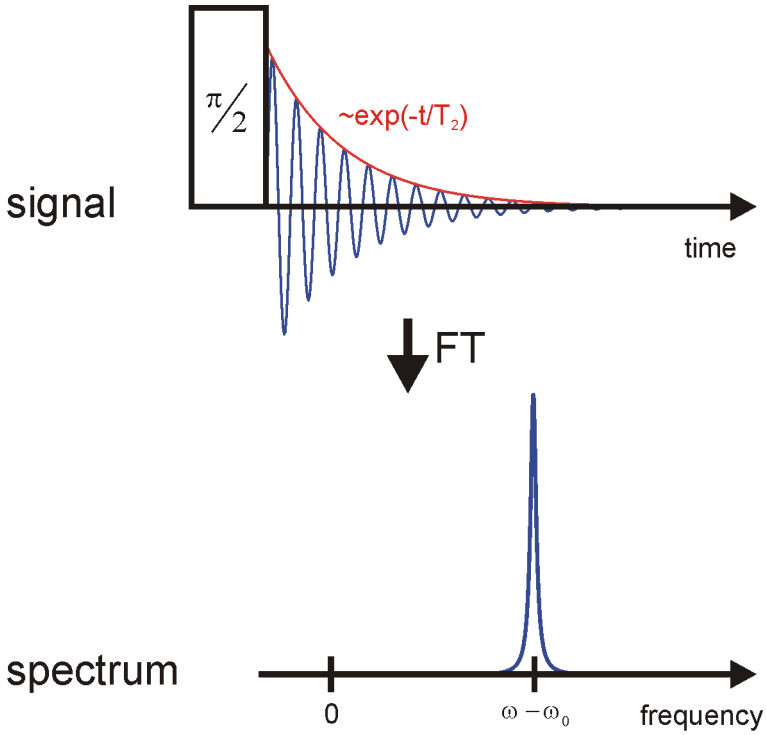

Figure 2.3: A $\left(\frac{\pi}{2}\right)_x$-pulse, followed by the *free induction decay*. The signal decays exponentially with the characteristic time T_2.
Below: Upon Fourier transformation ("FT"), a FT-NMR spectrum is obtained, showing a signal at the frequency offset between the Larmor frequency ω_0 and the spectrometer reference frequency ω.

The FID oscillates with the frequency offset between the Larmor frequency ω_0 and the spectrometer reference frequency ω and – in the ideal case – decays exponentially with T_2. In reality, this value has to be replaced with T_2^* to account for the effect of spin-spin interactions and field inhomogeneity.
The FID is Fourier transformed, resulting in a *spectrum* with a resonance line at the frequency offset. The linewidth of the resonance line correlates with T_2^*: For a Lorentzian line the full-width-half-maximum ("FWHM") is $\frac{1}{\pi T_2^*}$.
Practically, an NMR spectrum is not obtained by one pulse and recording one FID. An NMR signal is very weak and covered with noise. Hence, to improve the signal to noise ratio ("SNR") of the resonance signal, the experiment is

performed multiple times in succession and the result is averaged, resulting in a SNR improvement factor of $\sqrt{\mathrm{N}}$ for N averaging scans. Because the experiment has to start with the magnetization being at its thermal equilibrium value, it is crucial to wait between scans until the longitudinal relaxation with characteristic time T_1 has reestablished that state. As a rule of thumb the delay between experiments should be $\approx 5 \cdot T_1$.
In an NMR spectrum, some valuable information about the sample is contained in the frequency offset $\omega_0 - \omega$. The first is the *chemical shift* δ. It stems from local magnetic fields caused by the electrons on their molecular orbitals: The electron cloud possessed a magnetic susceptibility, which partially shields the nucleus from the static magnetic field – thus on a local level the field becomes inhomogeneous. This local magnetic field causes a frequency shift of the resonant line of the nucleus from a reference value, i.e. it slightly alters ω_0. The normalized expression $\delta = \frac{\nu - \nu_{ref}}{\nu_{ref}}$ is called the chemical shift. It is independent from the static magnetic field strength and commonly given in parts per million, short ppm. Since the electron distribution is strongly dependent on the local geometry of the molecule, such as bond lengths and –angles, the chemical shift varies between different nuclei of the same kind, e.g. ^{1}H on the same molecule. This makes it in principle possible to distinguish different nuclei of the same kind by their chemical shift. Because the bond lengths and –angles vary with temperature, the chemical shift is also temperature dependent. This feature can be used to determine the temperature of a sample by NMR.[47]
In a similar fashion, the resonance line can be shifted by what is referred to as the *paramagnetic shift*, if there are paramagnetic species present in the sample. Since DNP samples are doped with stable radicals, those samples experience this effect. The electron spins of the radicals are polarized in a similar fashion as the nuclei (see equation 2.17), but to a higher extent, since their respective gyromagnetic ratio γ is larger. The nuclei experience the magnetization stemming from the radicals like they experience the electrons from their own molecule, which results in said paramagnetic shift of their resonance line. This effect is negligible for radical concentrations in the mM regime, but - depending on the radical - plays a large role for high radical concentrations.

Aside from the simple $\left(\frac{\pi}{2}\right)_x$-pulse NMR experiment yielding an FID, the inversion $(\pi)_x$-pulse can be of great use in the *inversion recovery* experiment. It consists of two pulses, separated by a variable delay time τ: First a $(\pi)_x$-pulse inverting the magnetization and after waiting the delay τ a $\left(\frac{\pi}{2}\right)_x$-pulse is applied and the FID recorded. The pulse scheme is depicted in figure 2.4.

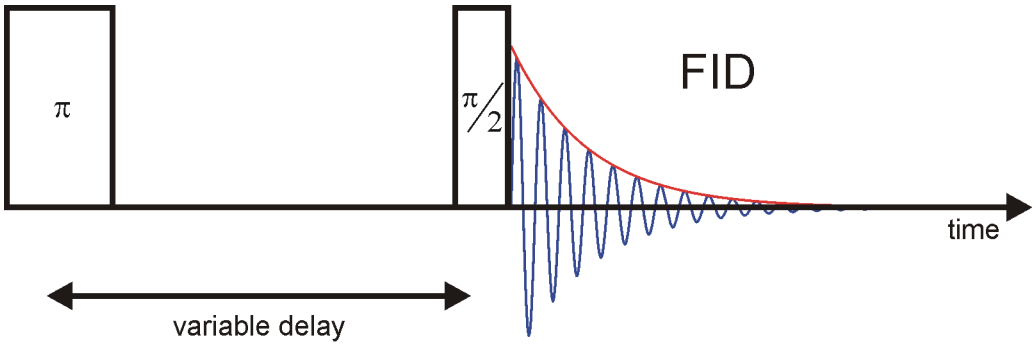

Figure 2.4: Pulse scheme for the inversion recovery NMR experiment. The magnetization in first inverted. After letting it relax back for a variable delay time τ a $\left(\frac{\pi}{2}\right)_x$-pulse is applied and the FID recorded. Plotting the signal intensity as a function of τ and fitting with an exponential yields the longitudinal relaxation time T_1.

According to the Bloch equations 2.27, the signal intensity A will behave as

$$A \propto 1 - 2e^{\frac{-\tau}{T_1}} \quad . \tag{2.28}$$

Therefore, by performing the experiment in an arrayed fashion, varying the delay time τ, yields data points, which can subsequently be fitted with equation 2.28, finally rendering the longitudinal relaxation time T_1.

2.2 EPR Basics

EPR is the analog to NMR for unpaired electrons. Because electrons are elementary particles bearing a spin $\frac{1}{2}$, their behavior can be treated in a similar fashion as protons in the previous NMR section. There are, however, very notable differences that will be briefly explained in this section. Because of its importance for liquid state DNP, the focus of this section is on nitroxide radicals in solution, which were used in this work.
As mentioned previously in equation 2.3, the magnetic moment of a *free* electron spin can be written as

$$\hat{\boldsymbol{\mu}}_S = \frac{g_e \mu_B}{\hbar} \cdot \hat{\mathbf{S}} \quad ,$$

using the Bohr magneton μ_B and the free electron g-factor $g_e \approx 2.0023193$. Analogous to the treatment of nuclear spin $\frac{1}{2}$, putting the free electron spin

in an external magnetic field $\mathbf{B}_0 = B_0\mathbf{e}_z$ splits the degenerate Zeeman levels. Their energies are given by

$$E_S = \gamma_S m_S \hbar B_0 = g_e \mu_B m_S B_0 \quad , \tag{2.29}$$

with the electronic spin quantum number $m_S = \pm\frac{1}{2}$. For the energy splitting this yields

$$\Delta E = \hbar\omega_S = g_e \mu_B B_0 \quad , \tag{2.30}$$

using the electron Larmor frequency ω_S. This behavior is illustrated in figure 2.5.

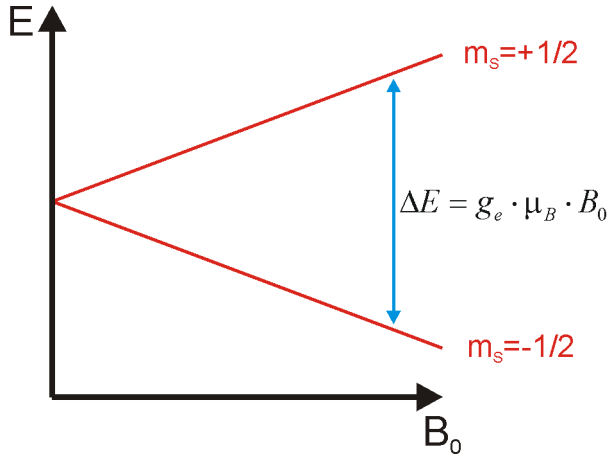

Figure 2.5: The Zeeman energy splitting for a free electron spin as a function of the external magnetic field B_0.

Because the Larmor frequency scales linearly with the magnetic field strength, designations by field and frequency values are equivalent. In EPR, however, it is common to label spectrometers with their operation frequency band, rather than the actual field value. E.g. an "X-band" spectrometer corresponds to a field value of approximately 0.35 T, "X-band" being the designation for microwave frequencies around 9.8 GHz for historical reasons.

If the unpaired electron is in an orbital of a molecule containing nuclei with nonzero spins, a coupling between its magnetic moment and the magnetic moment of those nuclei can be observed. For historic reasons, it is called the *hyperfine coupling*. The corresponding Hamiltonian is given by

$$\hat{H}_{IS} = \hat{\mathbf{S}} \cdot \underline{\mathbf{A}} \cdot \hat{\mathbf{I}} \quad , \tag{2.31}$$

with the hyperfine tensor $\underline{\mathbf{A}}$. It can be divided into two parts: An isotropic (scalar) part, and an anisotropic (dipolar) part.

The *isotropic hyperfine coupling* a_{iso} of a nucleus stems from the fact that the probability density of the electron is nonzero at the site of the nucleus. It is therefore also called the *Fermi contact interaction*, and is proportional to the the probability density at the site of the nucleus:

$$\hat{H}_{IS}^{iso} = a_{iso}\hbar\hat{\mathbf{S}} \cdot \hat{\mathbf{I}} \quad , \tag{2.32}$$

with

$$a_{iso} = \frac{8\pi}{3}\gamma_S\gamma_I\hbar^2|\Psi(0)|^2 \quad . \tag{2.33}$$

The anisotropic dipolar coupling adds an orientation dependent component. It is given by the Hamiltonian

$$\hat{H}_{IS}^{aniso} = \gamma_S\gamma_I\hbar^2\left(\frac{3(\hat{\mathbf{I}}\cdot\mathbf{r})(\hat{\mathbf{S}}\cdot\mathbf{r})}{r^5} - \frac{\hat{\mathbf{I}}\cdot\hat{\mathbf{S}}}{r^3}\right) \quad , \tag{2.34}$$

where $\mathbf{r}$ is the connecting vector between the point dipoles $\hat{\mathbf{I}}$ and $\hat{\mathbf{S}}$.
For a quickly tumbling molecule in solution, i.e. fast rotational diffusion, this dipolar interaction is averaged out and only the isotropic component remains. In contrast, in solid samples, the anisotropic part can be measured and in fact plays an important role in the spectra of solid samples.

2.2.1 EPR Spectrum of TEMPOL

In this work, experiments were performed exclusively with the TEMPOL radical. TEMPOL, or 4-hydroxy-2,2,6,6-tetramethyl-piperidine-1-oxyl, is a stable nitroxide radical, which solves well in water. Its chemical structure is shown in figure 2.6. With a molecular weight of 172.24 atomic units it is relatively light and small, thus in a water solution at room temperature and above, the isotropic limit is a valid approximation.

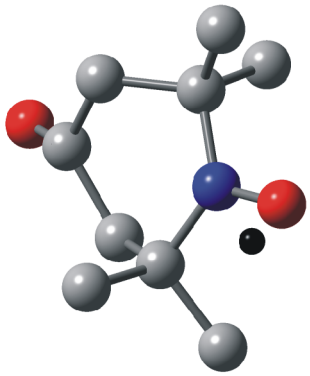

Figure 2.6: The chemical structure of TEMPOL, a stable nitroxide radical, which is used throughout this work. The ball and stick depiction shows carbon atoms in gray, oxygen in red and nitrogen in blue. The unpaired electron (black) is located between the nitrogen and the oxygen.

For a solution of TEMPOL in water at room temperature, the energy levels are given by

$$E(m_S; m_I) = \gamma_S m_S \hbar B_0 + \gamma_I m_I \hbar B_0 + a_{iso} m_S m_I \quad . \tag{2.35}$$

As a result, the EPR spectrum is governed by by the spin quantum numbers m_S and m_I, the isotropic hyperfine coupling constant a_{iso} and the external magnetic field strength B_0. m_S is limited to the values $\pm\frac{1}{2}$, while m_I depends on the nitrogen nucleus: If the nitrogen atom in the nitroxide is the naturally abundant ^{14}N, m_I can take three values $0, \pm 1$, while $m_I = \pm\frac{1}{2}$ for a ^{15}N-labeled radical.
In consequence, a_{iso} leads to the ^{14}N-TEMPOL spectrum featuring 3 hyperfine lines, equally separated by ≈ 16 G. This is depicted in figure 2.7.

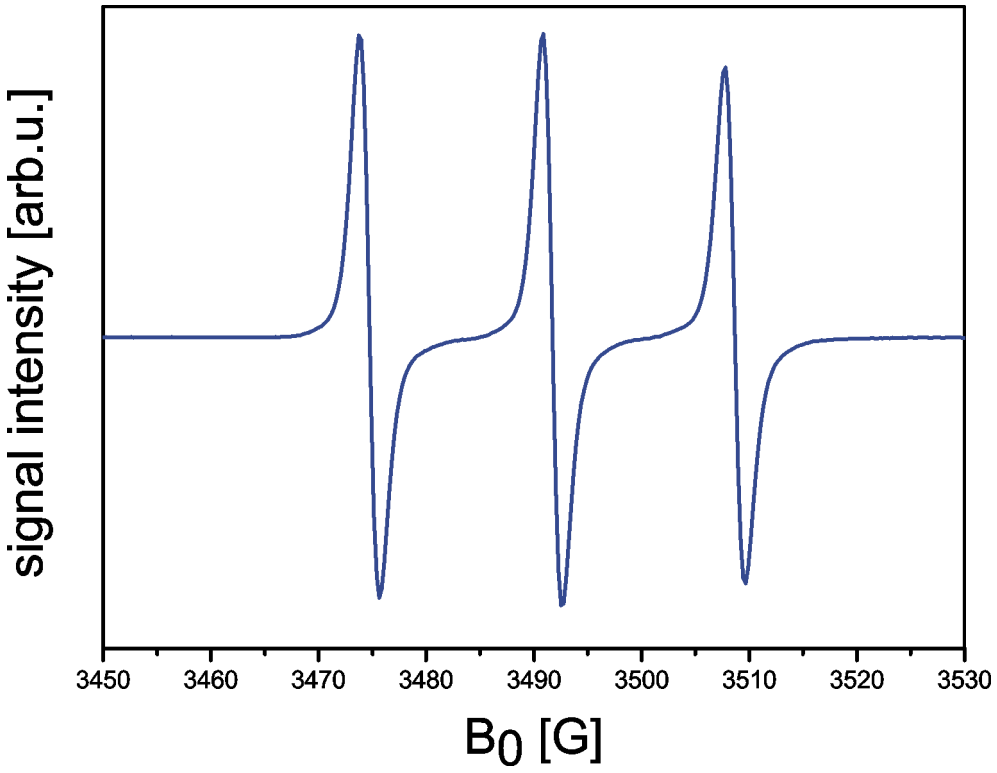

Figure 2.7: The CW-EPR spectrum of 10 mM ^{14}N-TEMPOL in water taken at X-band at room temperature. Three resonance lines can be observed, separated by the hyperfine coupling of $\approx$ 16 G.

2.3 Dynamic Nuclear Polarization

So far, NMR and EPR were only discussed separately. Both these fields in combination are essential for the treatment of DNP in the following section.

2.3.1 The Overhauser Effect

The spin Hamiltonian for an interacting pair of a particle with an electronic spin $\hat{\mathbf{S}}$ on a radical and a nuclear spin $\hat{\mathbf{I}}$, both of value $\frac{1}{2}$, in an external magnetic field $\mathbf{B}_0 \| \mathbf{e}_z$ is[20,48]

$$\begin{aligned} \hat{H}_{OE} &= \hat{Z}_S + \hat{Z}_I + \hat{H}_{SI} \\ &= \gamma_S \hbar (\hat{\mathbf{S}} \cdot \mathbf{B}_0) + \gamma_I \hbar (\hat{\mathbf{I}} \cdot \mathbf{B}_0) \\ &\quad + \gamma_S \gamma_I \hbar^2 \left[\frac{8\pi}{3} |\Psi(0)|^2 (\hat{\mathbf{I}} \cdot \hat{\mathbf{S}}) + \frac{3(\hat{\mathbf{I}} \cdot \mathbf{r})(\hat{\mathbf{S}} \cdot \mathbf{r})}{r^5} - \frac{\hat{\mathbf{I}} \cdot \hat{\mathbf{S}}}{r^3} \right] . \end{aligned} \quad (2.36)$$

The first two terms $\hat{Z}_S$ and $\hat{Z}_I$ are the Zeeman terms for the $\hat{\mathbf{S}}$ and the $\hat{\mathbf{I}}$ spin, respectively. The third term $\hat{H}_{SI}$ describes the scalar and dipolar interaction between the two, while nuclear spin-spin interactions are not considered. The Zeeman terms do not induce any relaxation and can therefore be neglected for the derivation of the *Overhauser Effect*. The scalar part is proportional to the square of the wave function $\Psi(0)$ of the electronic spin $\hat{\mathbf{S}}$ at the site of the nucleus and is referred to as the *"Fermi Contact Term"*. The last term describes the classic dipolar coupling of the spins. For the rapid motion between the $\hat{\mathbf{S}}$ and the $\hat{\mathbf{I}}$ spin in a typical low-viscosity liquid such as water, it is averaged to zero and hence does not contribute to time independent interactions of the system, such as the energy levels. However, it is the origin of relaxation and therefore the *Overhauser Effect*.

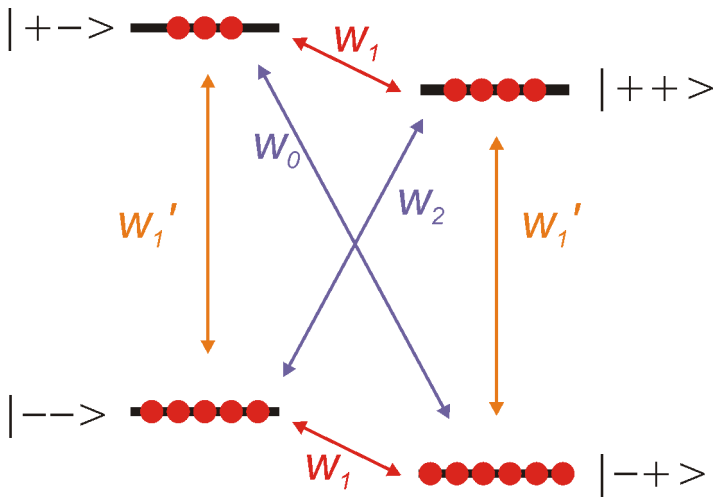

Figure 2.8: Energy level diagram of a two spin system of a nuclear spin coupled to an electronic spin. The red balls depict the Boltzmann populations of the respective states. Relaxation pathways (arrows) are marked with the respective rates w_0, w_1, w_1' and w_2. Notation is $|m_S m_I\rangle$. This figure is not drawn to scale.

By introducing the relaxation rates for the single quantum transitions w_1 and w_1', the zero quantum transition w_0 and the double quantum transition w_2 between the respective energy levels in figure 2.8 the total relaxation rate of the nuclear spin $\hat{\mathbf{I}}$ is obtained:

$$w^t = \frac{1}{T_1} = w_0 + 2w_1 + w_2 + w^0 \tag{2.37}$$

where w^0 contains all relaxation processes *not* involving the electronic spin $\hat{\mathbf{S}}$, i.e. they are not depicted in figure 2.8.

The nuclear polarization p is defined as

$$p := \frac{n_+ - n_-}{n_+ + n_-} = \frac{\langle \hat{I}_z \rangle}{I_0} \tanh \beta(E_- - E_+) \quad ,$$

i.e. the expectation value of the nuclear magnetization $\langle \hat{I}_z \rangle$, normalized by its thermal equilibrium value I_0 and weighted by the Boltzmann factor β. Since we are interested in deviations from magnetization from its thermal equilibrium value, we introduce the *enhancement factor* or short *enhancement* ϵ as

$$\epsilon := \frac{\langle \hat{I}_z \rangle - I_0}{I_0} \quad . \tag{2.38}$$

The experimental observables are the expectation values of the magnetizations in the z direction, $\langle \hat{I}_z \rangle$ and $\langle \hat{S}_z \rangle$.

From figure 2.8 one obtains the following coupled differential equations, referred to as the *Solomon equations*:[48]

$$\partial_t \langle \hat{I}_z \rangle = -(w_0 + 2w_1 + w_2)(\langle \hat{I}_z \rangle - I_0) - (w_2 - w_0)(\langle \hat{S}_z \rangle - S_0) \tag{2.39}$$

$$\partial_t \langle \hat{S}_z \rangle = -(w_2 - w_0)(\langle \hat{I}_z \rangle - I_0) - (w_0 + 2w_1' + w_2)(\langle \hat{S}_z \rangle - S_0) \tag{2.40}$$

While this properly describes the relaxation behavior of the nuclear spin, it is a negligible component for the relaxation of the electronic spin.

Including the relaxation rate w^0 for other pathways into equation 2.39 one obtains for the steady state $\partial_t \langle \hat{I}_z \rangle = 0$:

$$0 = \partial_t \langle \hat{I}_z \rangle = -(\underbrace{w_0 + 2w_1 + w_2 + w^0}_{w^t})(\langle \hat{I}_z \rangle - I_0) - (w_2 - w_0)(\langle \hat{S}_z \rangle - S_0) \quad , \tag{2.41}$$

which can be rearranged to give the *enhancement factor* introduced in equation 2.38:

$$\epsilon = \frac{\langle \hat{I}_z \rangle - I_0}{I_0} = \frac{S_0}{I_0} \cdot \underbrace{\frac{w_0 + 2w_1 + w_2}{w^t}}_{=:f} \cdot \underbrace{\frac{S_0 - \langle \hat{S}_z \rangle}{S_0}}_{=:s} \cdot \underbrace{\frac{w_2 - w_0}{w_0 + 2w_1 + w_2}}_{=:\xi} \quad . \tag{2.42}$$

By substituting

$$\frac{S_0}{I_0} = \frac{\gamma_S}{\gamma_I}$$

and defining the *"leakage factor"*

$$f := \frac{w_0 + 2w_1 + w_2}{w^t} \tag{2.43}$$

the *"saturation factor"*

$$s := \frac{S_0 - \langle \hat{S}_z \rangle}{S_0} \tag{2.44}$$

and the *"coupling factor"*

$$\xi := \frac{w_2 - w_0}{w_0 + 2w_1 + w_2} \tag{2.45}$$

one obtains the well known enhancement formula

$$\epsilon = \frac{\gamma_S}{\gamma_I} \cdot f \cdot s \cdot \xi \quad . \tag{2.46}$$

2.3.2 Leakage Factor

The leakage factor f in definition 2.43 is the ratio of the nuclear relaxation induced by the electronic spin and the *total* nuclear relaxation, including w^0. It can therefore be accessed via the nuclear spin-lattice relaxivity with the electronic spin present: $w^t = R_1^t = \frac{1}{T_1^t}$, and without the electronic spin present: $w^0 = R_1^0 = \frac{1}{T_1^0}$. This yields:

$$\begin{aligned} f &= \frac{w_0 + 2w_1 + w_2}{w^t} \\ &= 1 - \frac{w^0}{w^t} \\ &= 1 - \frac{T_1^t}{T_1^0} \quad , \end{aligned} \tag{2.47}$$

an expression containing only the longitudinal nuclear relaxation times T_1^t and T_1^0 of samples with and without electronic spins present, respectively. These values can be measured by performing inversion recovery NMR experiments on those samples, given that the nuclei in question are not on the radical itself.
Due to the additional relaxation pathways the value of T_1^t drastically decreases when electronic spins are added to a sample, so with increasing concentration

$$\lim_{[S]\to\infty} f = 1 \quad .$$

In a typical DNP sample, the leakage factor is therefore very close to 1.

2.3.3 Saturation Factor

The saturation factor s displays the degree to which the electronic transitions are saturated, i.e. by how much the populations of the $|--\rangle$ and $|+-\rangle$ states and the $|-+\rangle$ and the $|++\rangle$ states are equalized in figure 2.8. Full saturation means completely equalized populations ($\langle S_z\rangle = 0 \Rightarrow s = 1$), no saturation ($s = 0$) means the populations are at their thermal equilibrium value $\langle S_z\rangle = S_0$.
Practically the two transition frequencies are so similar, that one can safely assume them to be the same, therefore they can be saturated simultaneously with the same microwave excitation.
Assuming the validity of the Bloch equations 2.27 for the electronic spins, i.e. for a single EPR line without any couplings, one obtains:

$$\begin{aligned} s &= \frac{S_0 - \langle \hat{S}_z\rangle}{S_0} \underset{2.27}{\widehat{=}} 1 - M_z \\ &= \frac{\gamma_S^2 B_1^2 T_{1e} T_{2e}}{1 + (\omega - \omega_S)^2 T_{2e}^2 + \gamma_S^2 B_1^2 T_{1e} T_{2e}} \end{aligned}$$

with T_{1e} and T_{2e} being the longitudinal and transversal relaxation times of the electronic spin S, respectively, ω is the angular frequency of the field B_1 and ω_S is the Larmor frequency of the spin S.
A maximum is obtained for irradiation at the electronic Larmor frequency $\omega = \omega_S$:

$$s = \frac{\gamma_S^2 B_1^2 T_{1e} T_{2e}}{1 + \gamma_S^2 B_1^2 T_{1e} T_{2e}} \tag{2.48}$$

Infinite power, i.e. infinite B_1 leads to full saturation $\lim_{B_1\to\infty} s = 1$. Unfortunately, power and B_1 are always finite in reality, but by taking the reciprocal value

$$\frac{1}{s} = 1 + \frac{1}{1 + \gamma_S^2 B_1^2 T_{1e} T_{2e}} \propto \frac{1}{P_{MW}} \tag{2.49}$$

one obtains a formula showing linearity (i.e. affinity) between the reciprocal microwave power $\frac{1}{P_{MW}}$ and the reciprocal saturation $\frac{1}{s} \propto \frac{1}{\epsilon}$, the reciprocal enhancement, given that all other parameters remain constant. This can be used to extrapolate DNP results to infinite power and full saturation in a so-called *"power curve"*. However, in reality a variation of power will often cause a change in sample temperature, rendering this assumption moot. When plotting $\frac{1}{s}$ against $\frac{1}{P_{MW}}$ this power dependence of the sample temperature manifests itself in a deviation from linearity, especially at high microwave power due to the increased heating. Equation 2.48 also shows, that longer

electronic relaxation times T_{1e} and T_{2e} lead to better saturation.
In the case of hyperfine split EPR lines, e.g. 3 lines for a ^{14}N-nitroxide like TEMPOL, things become more complicated: Since equation 2.48 is derived for the idealized case of a single, homogeneously broadened, Lorentzian EPR line it has be modified to account for this. One may put

$$s = \frac{1}{n} \frac{\gamma_S^2 B_1^2 T_{1e} T_{2e}}{1 + \gamma_S^2 B_1^2 T_{1e} T_{2e}} \tag{2.50}$$

for n hyperfine lines, assuming the lines are well separated and do not interact. For instance, a ^{14}N-nitroxide with I=1 yields n=3, ^{15}N labeling renders n=2 hyperfine lines.
However, this description deteriorates in reality: If the lines are very broad, i.e. T_{2e} very short, the off resonance excitation of those lines will play a role. Additionally, in reality the coupling between hyperfine split lines cannot be ignored. Firstly, the hyperfine coupling between the electron and the nitrogen spin on a tumbling TEMPOL molecule provides a relaxation pathway, which mixes the electronic spin states.
Secondly, *Heisenberg Spin Exchange* ("HSE") is a major factor: HSE is a mechanism that flips two electronic spins S_1 and S_2 upon their collision in the solution. This mixes the lines while the total spin number is preserved:

$$|+\rangle_1 + |-\rangle_2 \leftrightarrow |-\rangle_1 + |+\rangle_2 \quad .$$

This can be accounted for by a HSE frequency ω_{ex}, which decreases inversely proportional with the rate of radical-radical encounters, i.e. with the radical concentration. HSE is very effective even at moderate radical concentrations of a few mM and therefore has to be considered. Effectively, it transfers the saturation from an irradiated hyperfine line to another.
In the limiting case of $w_1 \gg w_1'$ it can be analytically calculated[49] within the general theory of saturation transfer and double resonance effects in EPR.[50] For the case of a ^{14}N-TEMPOL radical in solution, which is irradiated at the central resonance line, the saturation effect on the other lines via HSE is given by

$$s = \frac{1}{1 + \frac{\omega_{ex}}{6 w_1'}} \quad .$$

If the relaxation rates and ω_{ex} were known, this would allow a calculation of s. However, they are not, but they and hence the saturation factor s can be experimentally accessed by performing pulsed **EL**ectron **DO**uble **R**esonance ("ELDOR") experiments.[51]
At very high radical concentrations (usually $\gg$ 100 mM) HSE will become so strong that the hyperfine lines collapse into a single line. In this case

equation 2.48 can again be an appropriate approximation.

2.3.4 Coupling Factor

The most critical (and maybe most important) quantity in DNP is the *coupling factor* ξ. It expresses how strongly the electronic spins $\hat{\mathbf{S}}$ and the nuclear spin $\hat{\mathbf{I}}$ couple and therefore how efficient the polarization transfer between them is.
The coupling factor is strongly dependent on the strength of the static magnetic field B_0 and is closely related to the total relaxation rate w^t. Consequently, it can in principle be accessed via relaxivity measurements.[35,52–54]
ξ is largely determined by the relaxation rates w_0 and w_2. For these two transitions to be effective, a modulation of the dipolar interactions $\hat{\mathbf{S}} \cdot \hat{\mathbf{I}}(t)$ between $\hat{\mathbf{S}}$ and $\hat{\mathbf{I}}$ on the timescale of the transition frequency $\omega_S(B_0)$ is necessary.
A fundamental difference between the transitions of w_0 and w_2 compared to w_1 is that they require the exchange of an energy quantum $\hbar(\omega_S \pm \omega_I) \approx \hbar\omega_S$ with the spin lattice, whereas the w_1-transition merely requires a much smaller energy quantum of $\hbar\omega_I$. If the angular frequency $\omega_S(B_0)$ is in a range, where the correlation spectrum of the molecular motion is "white", the necessary degrees of freedom for the exchange of energy quanta $\hbar\omega_S$ are available. This is the case if the product of the Larmor frequency and the correlation time of the liquid $\omega_S\tau \ll 1$. With increasing field strength B_0 and thus increasing ω_S, this condition will not be fulfilled anymore and eventually $\omega_S\tau \gg 1$. Consequently, w_0 and w_2 will drop and a dispersion of the relaxation can be observed in the $\omega_S\tau \approx 1$ region. Further increasing ω_S will fully diminish w_0 and w_2 and therefore ξ.[18] This behavior is depicted in figure 2.9.

In the case of pure dipolar coupling and isotropic motion of the spins, the behavior of the coupling factor as a function of field and correlation time is described by

$$\xi = \frac{12 \cdot J(\omega_S + \omega_I) - 2 \cdot J(\omega_S - \omega_I)}{2 \cdot J(\omega_S - \omega_I) + 2 \cdot 3 \cdot J(\omega_I) + 12 \cdot J(\omega_S + \omega_I)} \quad , \tag{2.51}$$

where $J(\omega)$ is the spectral density function of the molecular motion.[18,20,48,55,56]
Taking $\omega_S \gg \omega_I$ into account, this yields the approximation for the coupling factor

$$\xi \approx \frac{5 \cdot J(\omega_S)}{3 \cdot J(\omega_I) + 7 \cdot J(\omega_S)} \quad . \tag{2.52}$$

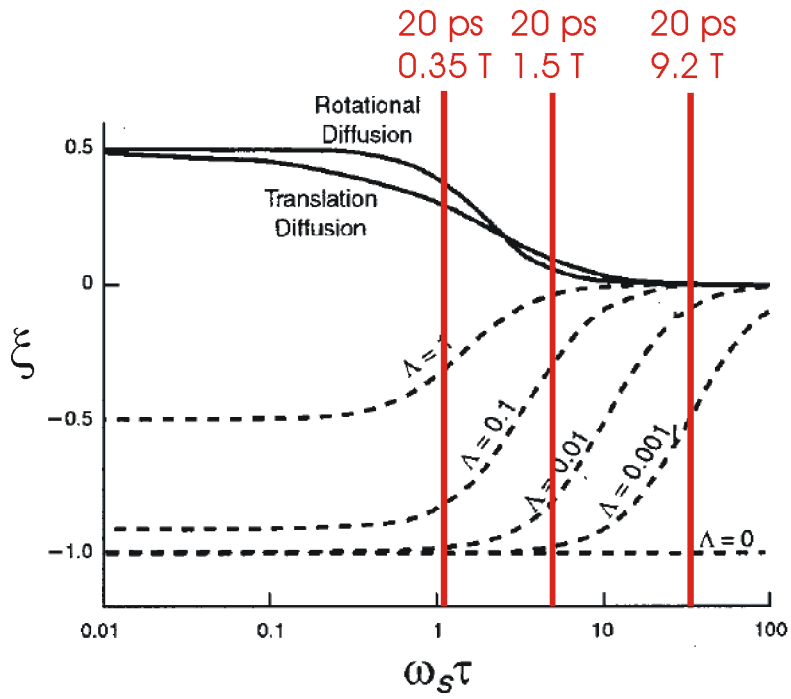

Figure 2.9: Coupling factor ξ versus the product $\omega_S\tau$ for dipolar interaction (solid lines) and scalar interaction (dashed lines).[20] In the case of scalar interaction, the parameter Λ accounts for relaxation contributions by spin exchange. The red vertical lines mark the values of $\omega_S\tau$ for a correlation time $\tau = 20$ ps (typical for water at room temperature) for 0.35 T, 1.5 T and 9.2 T magnetic field strength, respectively.

At low magnetic fields, one can safely assume the validity of the conditions of the *extreme narrowing limit*. This is the case for fast molecular motion and therefore short correlation times τ compared to the Larmor frequency, so $\omega_S\tau \ll 1$. It can be shown that under these conditions T_{1e} becomes similar to T_{2e} and with $J(\omega_S) \approx J(\omega_I) \approx J(0)$ equation 2.52 renders the theoretical maximum for ξ:

$$\xi = \frac{5 \cdot J(0)}{3 \cdot J(0) + 7 \cdot J(0)} = \frac{1}{2} \quad .$$

For a solution of nitroxide radicals in water, this condition is no longer satisfied for fields higher than 0.35 T ("X-band"), for which the Larmor time scales $\frac{1}{\omega_S}$ drop to a few picoseconds.
The spectral density functions in equations 2.51 and 2.52 are calculated by a Fourier transform from the time correlation functions of the molecular mo-

tion:[55–57]

$$J(\omega) = Re \int_0^\infty C(\tau) \cdot e^{-i\omega\tau} d\tau$$

the correlation function being the average over time and the ensemble of the dipolar interaction F with the time dependent connecting vector $\mathbf{r}(t)$

$$C(\tau) = \overline{F(\mathbf{r}(t)) \cdot F^*(\mathbf{r}(t+\tau))} \quad . \tag{2.53}$$

Since these equations contain the spectral density function evaluated at the low nuclear Larmor frequency ω_I in the denominator, ξ is sensitive on the long term decay of the correlation function and therefore on the model used to obtain that correlation function.
For translational diffusion, the dipolar spectral density can be modeled by

$$J(\omega) \propto \int_0^\infty J_{3/2}^2(u) \cdot \frac{u \cdot du}{u^4 + \omega^2 \tau_t^2} \quad , \tag{2.54}$$

where $J_{3/2}(u)$ is the $\frac{3}{2}$-order Bessel function and τ_t is the translational correlation time, which can be obtained from the diffusional hard-sphere model using

$$\tau_t = \frac{d^2}{D_S + D_I} \quad , \tag{2.55}$$

from the distance of closest approach d between $\hat{\mathbf{S}}$ and $\hat{\mathbf{I}}$, and the respective diffusion constants D_S and D_I.[20,55]
For this modeling approach, the spectral density $J(\omega)$ will decay as $\omega^{-\frac{3}{2}}$ for high fields and thus $\omega\tau_t \gg 1$, whereas more refined calculations render a decay of $J(\omega) \propto \omega^{-2}$.[56,57]
In the case of complex formation of the molecules carrying $\hat{\mathbf{S}}$ and $\hat{\mathbf{I}}$, for an average timescale $\tau_a \gg \tau_t$, the dipolar interaction becomes time dependent by the rotational motion of the complex and by its lifetime τ_a. In this case an exponentially decaying correlation function is a good approximation, yielding a spectral density of the form

$$J(\omega) \propto \frac{1}{1 + \omega^2 \tau_c^2} \quad , \tag{2.56}$$

with the correlation time $\tau_c^{-1} = \tau_r^{-1} + \tau_a^{-1}$ containing τ_a and the rotational correlation time τ_r, which can in principle be obtained from an Einstein-Stokes model.[55]

A computational approach to determining the coupling factor ξ is a molecular dynamics ("MD") simulation.[56] These simulations model the physical

movement of the molecules of the respective system, e.g. a radical in a bounding box with a multitude of solvent molecules, e.g. water. Because the simulation can describe the system with atomic resolution on a sub-picosecond timescale, the correlation function in equation 2.53 can in principle be extracted and the coupling factor can be calculated.

2.3.5 DNP in Solids

DNP in liquids, which is described by the Overhauser effect, relies on the time dependence of the relative positions of the spins $\hat{\mathbf{S}}$ and $\hat{\mathbf{I}}$. However, in the solid state, this is not the case. Consequently, the DNP is described by other DNP mechanisms.

The *Solid Effect* ("SE") is a two spin process involving flip flop transitions between an electron and a nearby nuclear spin induced by the microwave field.[27,58,59] It relies on the mixing of the spin states due to the hyperfine coupling between them. By supplying energy quanta of $\hbar(\omega_S \pm \omega_I)$ trough irradiation, zero or double quantum transitions, i.e. "forbidden" transitions to the first order, are induced, and the electron spin polarization is transferred to the nearby nuclei. The corresponding transition probability and therefore the enhancement scales with B_0^{-2}, limiting the effectiveness of the SE at high fields. Subsequently, the polarization is transported further away from the electron spin by flip flop processes between nuclei, polarizing the entire sample. This process is referred to as "(nuclear) spin diffusion".

The other two DNP mechanisms, the *Cross Effect* ("CE") and *Thermal Mixing* ("TM"), are somewhat similar. Both rely on allowed transitions, rather than forbidden transitions like the SE, and involve the interaction of electron spin packets in a homogeneously broadened (TM) or inhomogeneously broadened (CE) EPR line.[24,26,27,60,61] The intermediate case with both homogeneous and inhomogeneous interactions has also been treated.[25] At high magnetic fields, the CE is a three spin process involving two dipolarly coupled electrons and a nucleus. If the width of the EPR spectrum is larger than the Larmor frequency of the nucleus ω_I, the condition $\omega_{S1} - \omega_{S2} = \omega_I$ can be fulfilled, i.e. there are effectively two EPR resonance frequencies, separated by ω_I. Simultaneously, the homogeneous linewidth δ must satisfy $\delta < \omega_I$. This is achieved by using biradicals as polarizing agents with dipolar coupling between between the two spins.
If a well-fitted polarizing agent is used, $\omega_{S1} - \omega_{S2} = \omega_I$ can be fulfilled. This means the $|+-+\rangle$ and the $|-+-\rangle$ state and the $|+--\rangle$ and the $|-++\rangle$

state become degenerate and the states mix. If this is the case, a three spin flip process, flipping both involved electrons and the nucleus can transfer the polarization.
Because the linewidth of a powder EPR spectrum scales linearly with the static magnetic field strength, meeting the degeneracy condition will become harder with increasing field. In consequence, CE enhancements scale as B_0^{-1}. In contrast, for TM a homogeneously broadened line is needed, stemming from many dipolarly coupled electrons, i.e. TM is a multispin process. Here, the homogeneously broadened line is broader than the nuclear Larmor frequency $\delta > \omega_I$. It is explained thermodynamically, treating the multispin system with a spin bath model.[26,62] The electron-nuclear spin system can be described as a set of three interacting baths, each characterized by a spin temperature: the electron Zeeman system ("EZS"), the electron dipolar system ("EDS"), and the nuclear Zeeman system ("NZS"). Off resonance irradiation of the allowed EPR transition results in a large polarization gradient across the EPR line, which is equivalent to cooling the EDS. This bath is in thermal contact with the NZS, which is also cooled in an energy conserving three-spin electron-electron-nuclear exchange process, leading to DNP enhancement. The TM process can be direct, i.e., the enhancement is caused by the direct coupling between the NZS and the EDS, or indirect, when both allowed and forbidden transitions are induced.[27] However, compared to the CE, the TM effect is less efficient and results in smaller enhancements.[61]

Chapter 3

Liquid State DNP at High Fields

Early after its discovery, liquid state DNP via the Overhauser Effect has been shown to work well at relatively low magnetic fields below 1 T. Following the field dependence of the coupling factor ξ depicted in figure 2.9, considerable enhancements have been reached. However, the predicted decline of the coupling factor and thus the enhancement towards higher magnetic fields has led to the belief, that liquid state DNP will be too inefficient to use at high magnetic fields. Unfortunately, high magnetic fields are mandatory for magnetic resonance methods that rely on spectral resolution, including spectroscopic liquid state NMR and MRI. In consequence, the application of liquid state DNP to those methods has not been considered until recently.
This chapter is dedicated to the challenge of performing liquid state DNP at high magnetic fields. In the first section, the hardware is introduced, while in the second section the experimental results are presented and interpreted.

3.1 Hardware

Performing DNP experiments at high magnetic fields is by no means an easy task. Especially the technical challenges are tremendous: A magnetic field strength of 9.2 T corresponds to roughly 260 GHz EPR frequency, i.e. the EPR wavelength is as short as 1.1 mm. Consequently, microwave structures are tiny. Additionally, generating adequate levels of microwave power at 260 GHz poses another challenge.
In this section, the hardware that was used for DNP experiments at 9.2 T is introduced. The first subsection describes the 9.2 T DNP spectrometer, while the second subsection is dedicated to the description of the microwave

sources.

3.1.1 The DNP Spectrometer

The DNP spectrometer consists of a commercially available superconducting 9.2 T wide bore magnet (Bruker) and a corresponding 400 MHz NMR console (Bruker Avance). Additionally, it is equipped with a home built microwave bridge operating at 260 GHz for the excitation and detection of the EPR signal and a home built double resonance DNP probe (260 GHz / 400 MHz).[63]

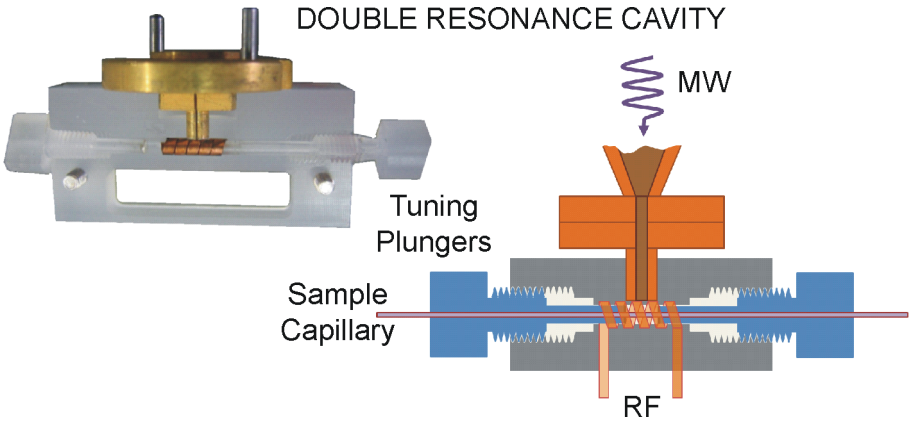

Figure 3.1: Photograph (left) and schematic drawing (right) of the double resonance structure used for NMR at 400 MHz and EPR at 260 GHz simultaneously.

The DNP probe contains the double resonance structure, an RF tuning setup, and the metal-dielectric microwave waveguide (Institute of Radiophysics and Electronics, Kharkiv, Ukraine). It consists of a helix coil for NMR detection, which serves as the body of a TE_{011} cylindrical resonator for the EPR excitation and detection at the same time. The leads of the coil are connected to the RF circuit tuned to 400 MHz NMR frequency. The microwave resonance mode is maintained inside of the helix between two plungers made of MACOR® (Corning Inc.) with silver coated caps. The structure is coupled to the waveguide in the middle of the helix through an elliptical iris in the copper tape of the helix, approximately 0.4 mm long and 0.25 mm wide. The structure is depicted in figure 3.1. For microwave cavity tuning, one of the plungers can be moved from outside of the probe via gears and a driving rod. The radio frequency of the NMR circuit can be tuned in the range from 390 to 400 MHz; its conversion factor is $\approx 0.17\ \frac{\mathrm{mT}}{\sqrt{\mathrm{W}}}$ and its

quality factor Q about 70. The microwave resonance of the cavity can be tuned between 256 and 260 GHz, typically reaching a conversion factor of $\approx 0.45\ \frac{\mathrm{mT}}{\sqrt{\mathrm{W}}}$ and a quality factor of approximately 400.[41]

For DNP measurements the liquid sample is put into a quartz capillary (Polymicro Technologies), which is placed along the axis of the cylindrical cavity. That way, the sample is exposed to the maximum of the magnetic component of the microwave field in the resonator, while it is in a minimum of the electric component, which is responsible for dielectric losses and thus sample heating. Three capillary sizes are used: 20, 30 and 50 μm inner diameter ("ID") and 150 μm outer diameter ("OD") each. With a cavity length of 1.6 mm this yields 0.6, 1.4 or 4 nl of sample volume, respectively.

The microwave bridge is depicted schematically in figure 3.2. It consists of oversized waveguides (Institute of Radiophysics and Electronics, Kharkiv, Ukraine), calibrated attenuators, a beam splitter and two zero-bias Schottky diodes (VDI-WR3ZBD-S027C, Virginia Diodes). One diode is used to measure the reflected power for the microwave coupling of the probe, the other to monitor and calibrate the incident power during DNP experiments. Each diode is protected by its respective calibrated attenuator.

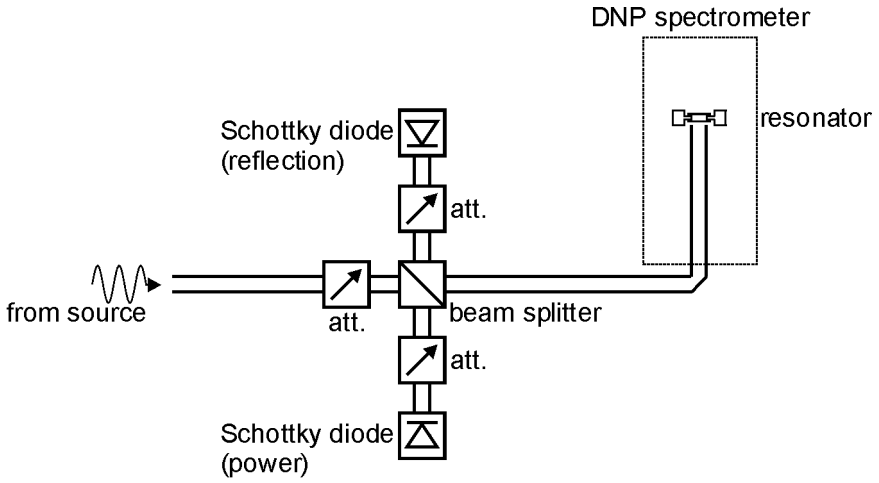

Figure 3.2: Block diagram of the microwave bridge. The incident microwave power from the source is first attenuated before reaching the beam splitter, which can be set to 24 dB for DNP operation or 3 dB for coupling. The incident and reflected microwave power is monitored by two Schottky diodes, protected by their respective calibrated attenuators.

The beam splitter can either be set to 3 dB or to 24 dB. The coupling of the probe is achieved by setting the beam splitter to 3 dB, i.e. approximately half of the reflected microwave power from the probe goes to the respective diode. The coupling of the probe can now be monitored by observing the reflected power. During DNP experiments, the 24 dB setting is chosen. That way -24 dB of the incident power goes first through the calibrated attenuator and then to the other diode, making it a calibrated power monitor. This power monitor allows real time tracking of the incident microwave power, which is critical for power sensitive DNP experiments.

For typical NMR experiments not requiring a double resonance structure, such as T_{1n} measurements or presaturation experiments, a commercial 400 MHz liquid state probe head is used (Bruker BBI).

3.1.2 Microwave Sources

Two microwave sources for the excitation of the EPR transitions in continuous wave ("CW") mode are used.
The first is a solid state source (VDI-S019b, Virginia Diodes), which delivers approximately 45 mW of microwave power.[63] It consists of a temperature stabilized yttrium iron garnet ("YIG") oscillator, driving a cascade of multiplication-amplification stages. The final output frequency can be tuned from 245 to 265 GHz by varying the bias voltage of the YIG oscillator. Because this bias voltage is well stabilized, the source exhibits a frequency instability below $10^{-5}\ \frac{1}{\mathrm{h}}$, making it suitable for prolonged DNP experiments without drifting off resonance.

The second microwave source that is used is a gyrotron (Gycom, Russia), which can generate up to 20 W of microwave power at 260 GHz.[41] Compared to the solid state source this means three orders of magnitude more power, but it is significantly more complex to operate, requiring many auxiliary systems and is in consequence harder to handle. The gyrotron is a free electron maser that uses the cyclotron resonance of an electron beam in a magnetic field at relativistic energies inside a resonator cavity to generate microwave power. It operates in a magnetic field of 4.7 T, which is provided by a cryomagnet. The operation frequency of the gyrotron is close to the second harmonic of the electron's cyclotron resonance and is determined by the cavity of the gyrotron. It can be tuned in a very limited range by changing the temperature of the cooling water for the copper gyrotron resonator, slightly varying its dimensions through thermal expansion. A temperature

change from 15 °C to 35 °C changes the gyrotron resonance frequency by about 60 MHz. The frequency stabilization is achieved by a cooler (P-307, ThermoTek), which achieves a temperature stability of ±0.1 °C.

3.1.3 Power Transmission

Due to their respective stray fields, the gyrotron in its magnet and the DNP spectrometer cannot be placed close to each other. Therefore, an effective power transmission system from the gyrotron to the DNP spectrometer is needed. This is achieved by a quasi-optical MW transmission line (Gycom, Russia). The transmission line consists of 18 mm ID corrugated waveguide pieces with a total length of 14 m, and some passive components such as a calorimeter, an attenuator, 90° bends, and a mechanical MW switch. The total MW losses are measured to be approximately 4 dB to the DNP probe.

3.1.4 Experimental Procedures

Unless otherwise specified, the DNP enhancements were determined by taking the ^{1}H FT-NMR spectrum of the samples with and without CW microwave irradiation of the central hyperfine line of the ^{14}N-TEMPOL radicals, respectively, and integrating the proton NMR lines to determine the signal strength. Using equation 2.38, the enhancement can then be calculated. The optimal irradiation frequency for maximum DNP enhancement was determined both by a frequency-swept CW EPR experiment and empirically.
Because this method takes the integral value of the NMR signal, it is insensitive to possible spacial inhomogeneities of the magnetization. In other words, this method yields an average or net enhancement for the entire sample volume, regardless of the actual magnetization distribution. Consequently, when trying to determine a *maximum* value for the enhancement, this method will underestimate this value. This is not the case if the *peak* values of the NMR spectra are used instead of the integrals. However, this method of using peak values is prone to error. This is due to the distortion of the spectra because of temperature gradients, B_1 gradients within the sample, B_1 instabilities during averaging and the impact of noise peaks. It should therefore be applied cautiously.

Putting the samples into the quartz sample capillaries was achieved by dipping the capillaries into the liquid sample. For low-viscosity liquids like

water, the capillary forces suffice to pull the liquid into the capillary and fill it. The capillaries were subsequently sealed with wax in a similar way: The wax was heated to approximately 90 °C, making it very low-viscous as well. Both ends of the capillary with the sample were then briefly dipped into the liquid wax. In this way, the wax does not only coat the cooler capillary on the outside, but it is also drawn into the capillary for a short distance before it cools and hardens, forming a wax plug *in* the capillary. On one tip, the excess wax coating the outside was subsequently removed, so it would not come off when the sample is placed in the resonator.

Unfortunately, the sample temperature in a DNP experiment cannot be accessed directly. A 4 nl sample is much to small for this, e.g. via a thermocouple. Luckily, the sample temperature can be accessed via NMR and the temperature dependent chemical shift δ. For each incident power, solvent and capillary size used in any DNP experiment, a temperature reference is taken: The reference sample is a sample containing the same, pure solvent without radicals and the same capillary size and hence has the same dielectric losses and the same microwave heating for a given incident microwave power. For every incident power, the NMR spectrum is taken. Since the reference contains no radicals, no paramagnetic shift occurs and only the temperature shift of the pure solvent through the microwave heating is observed.
The temperature shift is then calibrated by monitoring the chemical shift of the reference sample while heating the entire probe head and hence the reference sample with a hot gas stream. The system is given 10 minutes at the set temperature to come to thermal equilibrium, then the temperature of the probe head is measured with a thermistor in different positions, yielding a range for the sample temperature. While the temperature dependence of the chemical shift of e.g. water is in principle known,[47] the sample shape, size and orientation plays a large role as well.[64,65] In consequence, the calibration must be performed as described above.
The temperature calibrated chemical shift can now be used to extract the temperature of the reference sample under microwave irradiation at a given microwave power. The microwave heating goes linearly with applied microwave power and they respective temperature shift is reproducible for each capillary size. It can therefore be considered an approximation for the temperature of the DNP sample irradiated with the same power.

3.2 Experimental Results

In this section, the experiments that were performed at 9.2 T are presented and discussed. While the target nuclei are protons in all presented cases, the range of target molecules is broad: The first subsection deals with water as a target, the second subsection with organic solvents, namely toluene, acetone and dimethylsulfoxide ("DMSO"). In the third subsection, three small metabolites (pyruvate, lactate and alanine) in aqueous solution serve as polarization targets.

3.2.1 DNP on Water

Without a doubt, when it comes to biological or medical applications, water is the most important and most interesting solvent. Because it is the only "natural" choice one may even say it is *the* only interesting solvent for such applications.
Aside from its importance in nature, water has some properties that make it interesting for liquid state DNP. It has a high proton density of approximately 110 mol/l and a single NMR line, making it relatively easy to detect by NMR, even with very small samples. Also, it is low-viscous and rapidly diffusing (see table 3.2), so one can expect relatively short correlation times compared to other solvents and the validity of the isotropic limit for typical nitroxides in water solution. However, compared to other solvents water has a relatively high dielectric constant and it heats fast when exposed to microwave power. As a result, water samples need to be relatively small in order to avoid excessive sample heating during microwave irradiation.
The issue of dielectric losses in a water sample can make the analysis of DNP experiments a tedious task. The irradiation of the sample with microwave power will then always result in a change of sample temperature. Along with sample temperature everything that is temperature dependent will be changed as well, such as relaxation rates, EPR lineshapes, the molecular motion and its correlation time. In consequence, for a quantitative analysis, keeping track of the sample temperature is critical. But aside from the problems that dielectric heating causes, it can also be of use. Varying the sample size results in varying dielectric losses and thus in a variation of sample temperature for a given incident microwave power. Consequently, experiments were performed on water samples in capillaries with ID 20, 30 and 50 μm. This way, one can use the microwave heating to explore the Overhauser effect at various temperatures.
The DNP experiments were carried out on water samples containing ^{14}N-

TEMPOL radicals as a polarizing agent in concentrations ranging from 5 mM to 1 M. The concentration dependence of the DNP enhancement is depicted in figure 3.3 for various incident microwave powers and thus sample temperatures.

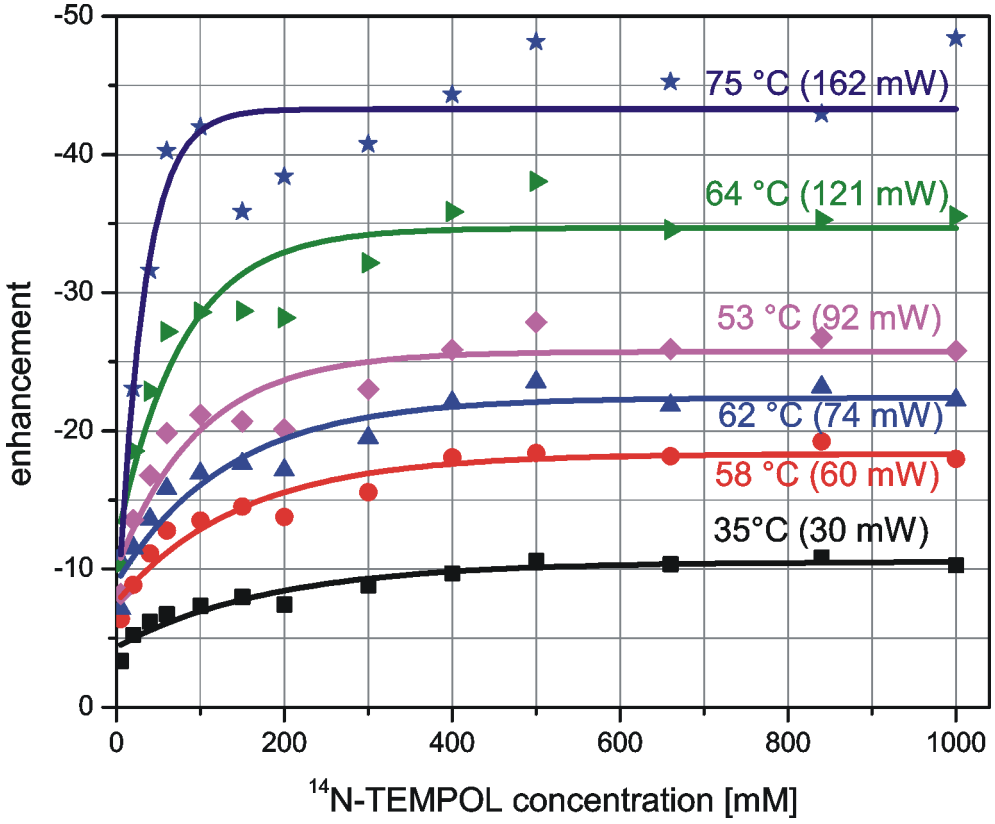

Figure 3.3: Dependence of the integral DNP enhancement on the radical concentration for various irradiation powers/sample temperatures.

For a given microwave power, the enhancement shows a monotonic increase with radical concentration. Above a concentration of roughly 100 mM, the curves flatten and approach an asymptotic maximum value, i.e. the enhancement does not significantly improve anymore with rising concentration. Increased microwave power concordantly leads to an increased sample temperature yields a higher enhancement. For a sample temperature of ≈ 64 °C, enhancement factors up to $\epsilon \approx -35$ are achieved. Putting in more power and heating the sample even more results in even higher enhancement factors up to ≈ -45 for ≈ 75 °C and even beyond that number. This is depicted in figure 3.4 for a 1 M ^{14}N-TEMPOL in water sample in three different capillary sizes, giving a different heating behavior.

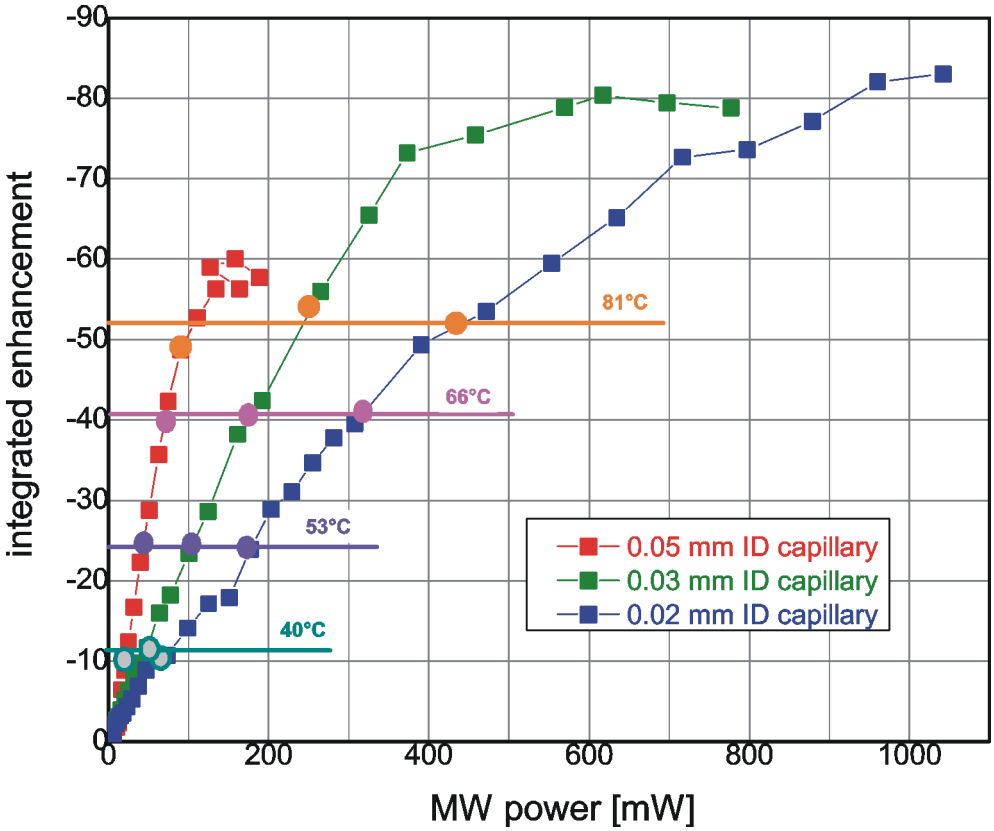

Figure 3.4: DNP enhancement for a 1 M ^{14}N-TEMPOL in water sample in a 20, 30 and 50 μm ID capillary, respectively, plotted against the incident MW power. The larger the sample capillary, the stronger the respective sample heats in the microwave field and the stronger the increase in sample temperature. The colored dots on the respective graphs and the corresponding colored horizontal lines indicate sample temperatures derived from NMR line shifts. For very high MW powers and sample temperatures, enhancements beyond -80 are observed.

So apparently, high enhancements up to $\epsilon \approx -80$ can be achieved by Overhauser DNP at 9.2 T with sufficiently large power for very high temperatures. To be able to quantitatively understand these Overhauser enhancements, the parameters in equation 2.46 have to be considered.

The leakage factor was determined for a broad range of radical concentrations ranging from 5 mM to 1 M and in a broad temperature range from room temperature, i.e. 298 K, to 365 K, i.e. just below the boiling point. This was achieved by measuring T_{1n} in the presence and the absence of radicals at the respective temperature and calculating the leakage factor f from

equation 2.47.
Being in the extreme narrowing limit, T_{1n} gets longer with increasing temperature. However, the effects in the presence and in the absence of radicals almost cancel out completely in the ratio, so the leakage factor f turns out to be almost independent of temperature. Its dependence on radical concentration is given for room temperature (25 °C) and for 92 °C in table 3.1.

T_{H_2O}	^{14}N-TEMPOL concentration			
	200 mM	100 mM	40 mM	5 mM
25 °C	0.99	0.98	0.95	0.66
92 °C	0.99	0.98	0.94	0.62

Table 3.1: Leakage factors for various concentrations of TEMPOL in water at 25 °C and 92 °C.

Because adding radicals to the solution adds a strong relaxation pathway and thus shortens T_{1n}, f shows a monotonic increase with radical concentration. At 40 mM TEMPOL concentration, the leakage factor has reached 0.95; at 200 mM it is 0.99 and therefore practically at its theoretical maximum of 1. This behavior results in the drop of DNP efficiency for low concentrations in the concentration dependence shown in figure 3.3.

The saturation factor in a DNP experiment is in general hard to access in this experimental setup. On the one hand it cannot be calculated well. As explained in subsection 2.3.3 this would require some assumptions on the EPR spectrum that may not be valid. Also, hard numbers for T_{1e} and T_{2e} are unavailable, because they were not measured at this field. On the other hand, the saturation factor cannot be easily accessed experimentally. The experimental setup has no ELDOR capability, which could directly determine s. Also, extrapolating to full saturation by equation 2.49 in a power curve will not work well, because the irradiation of the sample with varying microwave power always results in a change of sample temperature. Since the extrapolation is unstable in the first place, the temperature deviation prevents the power curve method from giving a result with a reasonable error.
Fortunately, s can be accessed via the paramagnetic shift. In a DNP sample in the static magnetic field, the nuclei experience a certain paramagnetic shift, depending on the radical concentration. If the electron spin transition is now saturated, the electron spin polarization is diminished. In consequence, the paramagnetic shift is diminished as well. At full saturation, i.e.

equalized electron spin populations and no polarization left, the paramagnetic shift has disappeared altogether. So if the temperature effect on the chemical shift ("temperature shift") and the variation of the paramagnetic shift can be distinguished well, monitoring the NMR peak position gives access to s. Because the paramagnetic shift scales linearly with the radical concentration, high concentrations are required to make it significant to be able to apply this method. For a sample with 1 M concentration of TEMPOL in water in a 30 μm ID capillary, the paramagnetic shift is large enough to do so, as can be seen in figure 3.5.

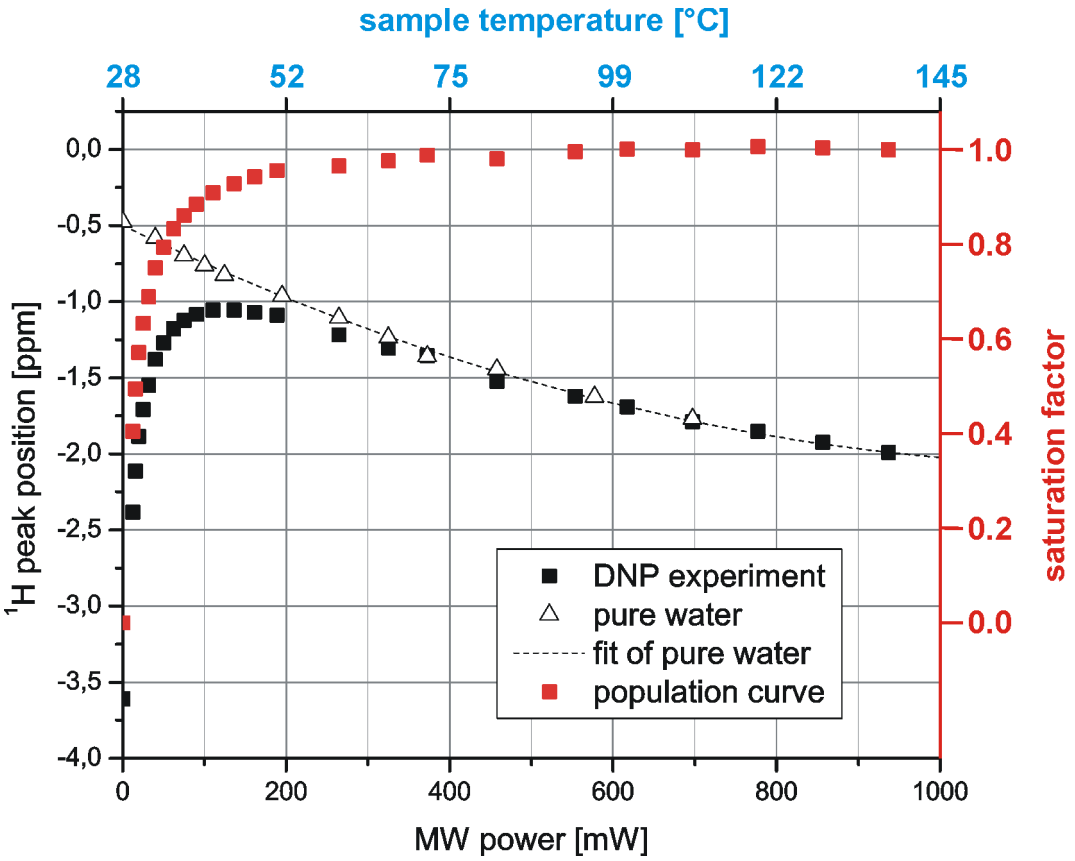

Figure 3.5: NMR line shift of the water peak of a pure water sample (white triangles) and a 1 M TEMPOL in water sample (black circles), plotted against the incident microwave power. Through the microwave heating calibration with the pure water sample, each irradiation power can be assigned a sample temperature (blue scale, top). By subtracting the temperature shift from the total NMR shift the pure paramagnetic shift is obtained, which can be scaled to give the saturation factor (red line, red scale on the right).

Figure 3.5 shows, that in this case, a microwave power of roughly 100 mW is sufficient for ≥ 0.9 saturation. For power above 100 mW the saturation factor does not improve much anymore, but the sample is heated further. In consequence the NMR line shift follows the temperature shift of the pure water sample.
The example also demonstrates, why this method is only feasible for a large radical concentration. Without MW irradiation, i.e. at $s = 0$, the paramagnetic shift for a 1 M concentration is approximately 3.1 ppm. For 100 mM, this yields only 0.31 ppm paramagnetic shift to begin with, making it hard to distinguish from the temperature shift and the method prone to error.

The behavior of the saturation factor can be better understood from the CW-EPR spectra of the DNP samples. The narrower the EPR linewidth of the respective spectrum, the easier it is to saturate the corresponding EPR transition. While the EPR spectrum is determined by the radical concentration, it it also determined by the incident MW power through sample heating. Both an elevated temperature and a higher concentration increase Heisenberg exchange, which collapses the three hyperfine lines into one. For the 1 M sample at 100 °C the line is as narrow as 6.2 G. This behavior can be observed in figure 3.6.

In conclusion, both a high radical concentration and an elevated sample temperature caused by microwave heating help to narrow down the linewidth and hence help to increase the saturation factor. Consequently, full saturation can be achieved here with adequate microwave power input as shown in figure 3.5.

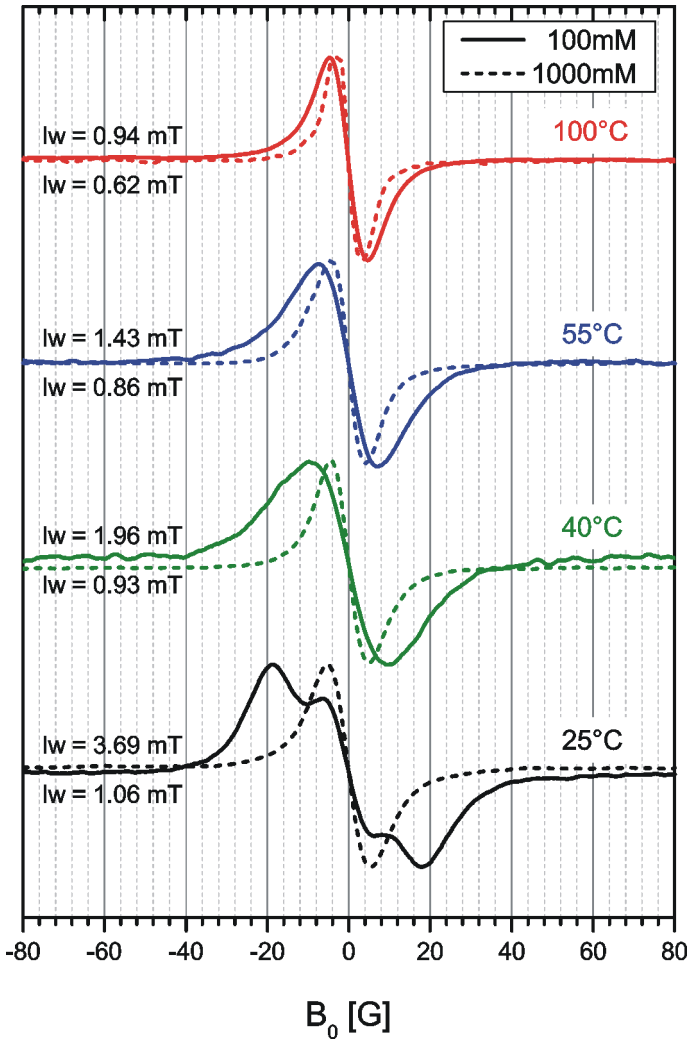

Figure 3.6: CW-EPR spectra of ^{14}N-TEMPOL in water samples with 100 mM (solid lines) and 1 M (dotted lines) radical concentration, respectively, at various temperatures ranging from room temperature (black spectra) to the boiling point (red spectra). In this regime both elevated temperature and radical concentration narrows the EPR line, making saturation easier. The corresponding linewidth is given on the left, next to the respective spectrum. The spectra were taken by Petr Neugebauer at the G-band (180 GHz) EPR spectrometer in our group.

Having determined the leakage factor (table 3.1), the saturation factor (figure 3.5) and the enhancement (figure 3.4) equation 2.46 can now be used to calculate the coupling factor for the respective sample temperature. These experimentally determined coupling factors can then be compared to coupling

factors extracted from NMRD measurements (see appendix A.1) and molecular dynamics simulations.[56] The result is depicted in figure 3.7.

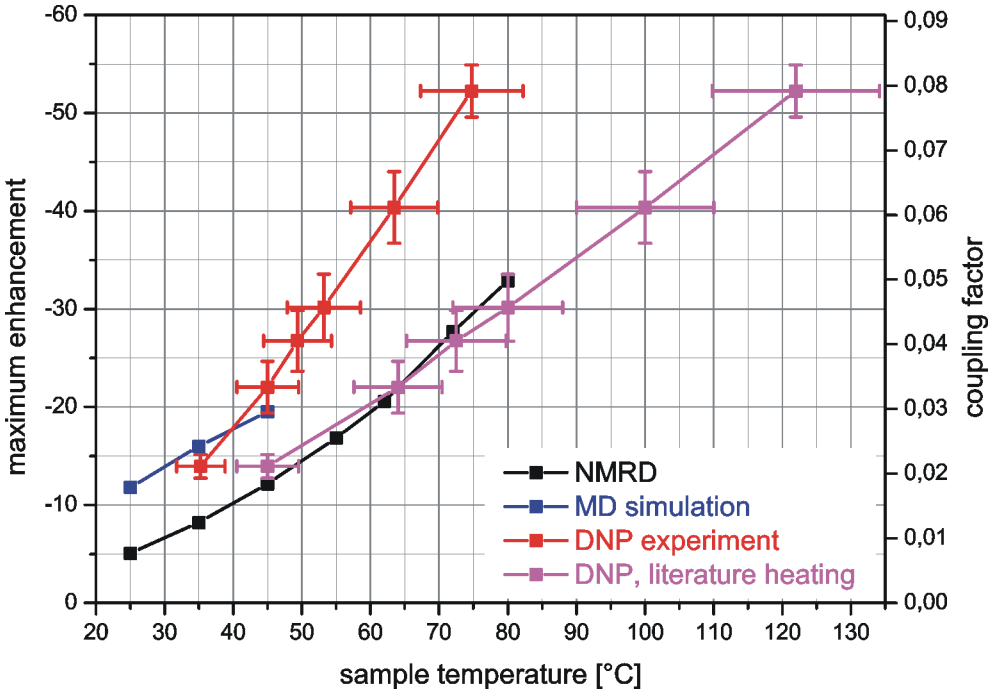

Figure 3.7: Maximum enhancement ($s = f = 1$) and coupling factor between the TEMPOL radicals and the water protons versus the calculated sample temperature. The red curve gives the experimentally determined coupling factors. The black curve shows the coupling factors extracted from NMRD measurements, while the blue data points are simulated by MD.[56] The errorbars indicate the statistical errors in enhancement and heating reproducibility. Note that there are systematic errors in the temperature as well. To demonstrate the range this might render, the purple curve shows the experimental data with the temperature assigned using the literature value for the temperature shift[47] instead of our own calibration.

The experimental (red) curve is closer to the MD simulations (blue) than to the NMRD data (black) which predict a lower coupling factor. However, the slope of the curve does not seem to correspond well to either. The errorbars on the experimental curve reflect the propagation of error from the determination of ϵ, f and s. For a quantitative interpretation, however, the error in the assigned temperature must be considered.
As described in chapter 2, the sample temperature is determined by the

temperature shift of the NMR line of a (water) reference sample, i.e. a pure solvent sample without paramagnets. In consequence, no paramagnetic shift is present and the dielectric heating behavior can be considered identical to the DNP samples. Because the temperature dependence of the chemical shift of water is known from the calibration, the shift of the ^{1}H-NMR peak can be used to calculate the temperature.

While this method gives an experimental access to the temperature of the DNP sample, it also introduces errors in several instances: Firstly, the microwave heating of any sample depends strongly on variations in sample placement, size and especially the microwave coupling of the resonator. Coupling the resonator must therefore be performed very exactly to make it truly reproducible. Fortunately, large deviations can be identified in the experiment: If the heating reference sample and the DNP sample are coupled significantly different, their respective NMR line shifts as a function of MW power will not show the same slope after the paramagnetic shift is diminished by EPR line saturation as demonstrated in figure 3.5. Instead, they will show different slopes, representing their different heating behavior. As a result, these experiments can then be discarded and redone. Overall, the approximation that the temperature of the heating reference for a given microwave power equals the temperature of the DNP sample for that power adds an additional statistical error of $\approx \pm 10\%$.

Additional to these statistical errors, the method of calibration described above introduces several systematic errors in the determination of temperature, making a quantitative analysis of the data very difficult:

For the calibration, the temperature of the probe head is measured and then taken as the temperature of the sample. A systematic error ensues, because the value depends on the position of the thermistor. The heating gas inlet gives the highest temperature, while the thermistor on the waveguide taper gives the lowest value, since it is in thermal contact with the outside. The temperature measured next to the Kel-F® holder lies between those two extremes and likely reflects the sample temperature more closely. Consequently, this systematic error is in the range of $\approx \pm 10\%$.

For water the calibration differs roughly a factor of 2 from the literature value.[47] While some of this difference can be accounted for by shape factors,[64,65] the probe head itself makes a difference as well. A shift calibration for the same sample shape, size and orientation for a probe consisting of only and NMR circuit renders a different value. In conclusion, the sample shape alone does not dominate the temperature behavior. Taking the literature values to calculate the sample temperature yields roughly twice the heating and hence the purple curve in figure 3.7.

Additionally, in the calibration, the *entire* sample is heated and the chemical

shift is observed. However, when the sample is heated by microwaves, only a very small region inside the resonator is heated, which is in good thermal contact with the surrounding, cooler sample. So in this case, a "heatsink" exists, which is not existent in the calibration.
Moreover, under DNP conditions, i.e. microwave irradiation, there is a temperature gradient over the sample, that is not captured with this method. This temperature gradient exists, because there is an inhomogeneous distribution of the electric component of the microwave field over the resonator. As a result the dielectric losses in the sample are inhomogeneously distributed as well and a temperature gradient ensues.
This temperature gradient across the sample increases with increasing the microwave power. While this can be observed on the large signals enhanced by DNP, this is not possible for the heating reference samples: Here, due to the low SNR, the maximum value is used to determine the peak position, as opposed to e.g. its barycenter. The peak maximum represents the central part of the sample[65] with the least contact to the cooler outside sample, neglecting any temperature gradients. The enhancement on the other hand is determined by integration over the entire sample volume.

In conclusion, in addition to the statistical error, the temperature values given here bear systematic errors, that are hard to evaluate. This is particularly important for the heating calibration, since the temperature plays a major role in understanding liquid state DNP. Consequently, another method to accurately determine the sample temperature under microwave irradiation has to be found. Currently, a temperature calibration via the temperature dependent value of T_{1n} is being evaluated.

The DNP buildup time was determined to be 133 ± 6 ms for 100 mM TEMPOL concentration for an incident microwave power of 45 mW and ≈ 40 °C sample temperature, as explained in appendix A.2. This is comparable to $T_{1n} = 130$ ms for this sample at a similar temperature. This militates in favor of the DNP effect being relaxation driven in this case.

3.2.2 DNP on Organic Solvents

Concordantly to the DNP experiments performed on samples with water as solvent, experiments were performed on TEMPOL solutions in acetone, DMSO and toluene. Their chemical structures are shown in figure 3.8.

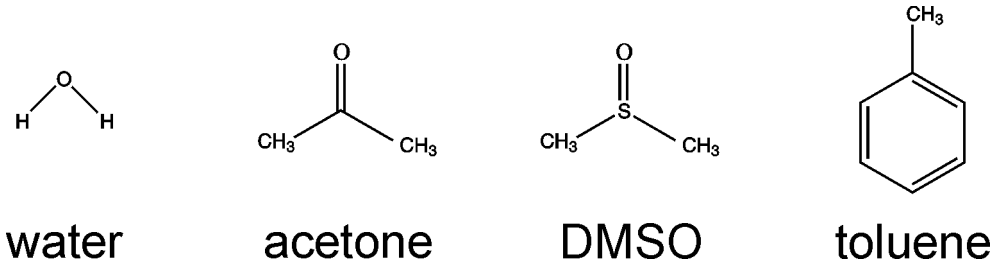

Figure 3.8: Chemical structures of the solvents used in this work: Water, acetone, DMSO and toluene.

For water, acetone and DMSO, all protons are equivalent, so those three substances feature a single ^{1}H-NMR line, while toluene has two proton lines: One from the methyl protons and one from the ring protons. While they are all relatively small, low-viscosity solvents, they differ significantly in their properties. Particularly acetone and DMSO are very similar in structure, but their diffusion constant differs by an order of magnitude. Some relevant properties of the solvents are displayed in table 3.2.

substance	molecular weight $[\frac{g}{mol}]$	viscosity $[mPa \cdot s]$	diffusion coefficient $[10^{-9}\ \frac{m^2}{s}]$	dielectric constant
water	18.0	1.0019	2.023	78.5
acetone	58.1	0.324	4.57 (25 °C)	20.7
DMSO	78.1	1.99[66] (25 °C)	0.73 (25 °C)	46.7
toluene	92.1	0.585	2.27 (25 °C)	2.38

Table 3.2: Physical properties of water, acetone, DMSO and toluene. Values are given for 20 °C and taken from,[67] unless specified otherwise.

In consequence, in equation 2.55 acetone and DMSO should feature the same distance of closest approach d, due to their similar structure. In both cases the methyl protons stick out to the side and access to the electron spin

should be similar. At the same time the diffusion constants D_I differ by an order of magnitude. Neglecting D_S, which is usually an order of magnitude smaller than D_I, the respective correlation times derived from equation 2.55 differ by an order of magnitude as well. The coupling factors obtained from this are given in table 3.3, for a $\xi \propto \tau^{-\frac{3}{2}}$ decay of the coupling factor[56] and a $\xi \propto \tau^{-2}$ decay,[57] using $d \stackrel{!}{=} 2\ \mathring{A}$ as the distance of closest approach for all solvents.

substance	diffusion coefficient $[10^{-9}\ \frac{\mathrm{m}^2}{\mathrm{s}}]$	correlation time τ_t [ps]	$\xi \propto \tau_t^{-\frac{3}{2}}$, normalized	$\xi \propto \tau_t^{-2}$, nomalized
water	2.023	19.8	1	1
acetone	4.57 (25 °C)	8.7	3.4	5.2
DMSO	0.73 (25 °C)	54.8	0.22	0.13
toluene	2.27 (25 °C)	17.6	1.2	1.3

Table 3.3: Diffusion coefficients, calculated translational correlation times (equation 2.55, $D_S \stackrel{!}{=} 0$, $d \stackrel{!}{=} 2\ \mathring{A}$) and calculated coupling factors (normalized to water) for a $\xi \propto \tau_t^{-\frac{3}{2}}$ and a $\xi \propto \tau_t^{-2}$ decay of water, acetone, DMSO and toluene. Values are given for 20 °C and taken from,[67] unless specified otherwise.

However, these large differences in coupling factors are not reflected in the DNP enhancements that are achieved with these solvents.

The DNP enhancement for the methyl protons of acetone and DMSO are depicted in figure 3.9, as well as the enhancements for both the methyl and the ring protons of toluene. With acetone, enhancements of ≈ -30 are reached, while DMSO shows enhancements up to ≈ -20. In toluene, enhancements of up to ≈ -15 can be observed on both the methyl and the ring protons, that do not differ significantly in this respect. However, the enhancements cannot be compared easily: While the leakage factor is $f \approx 1$ for all samples, the saturation factors and especially the sample temperatures differ significantly.

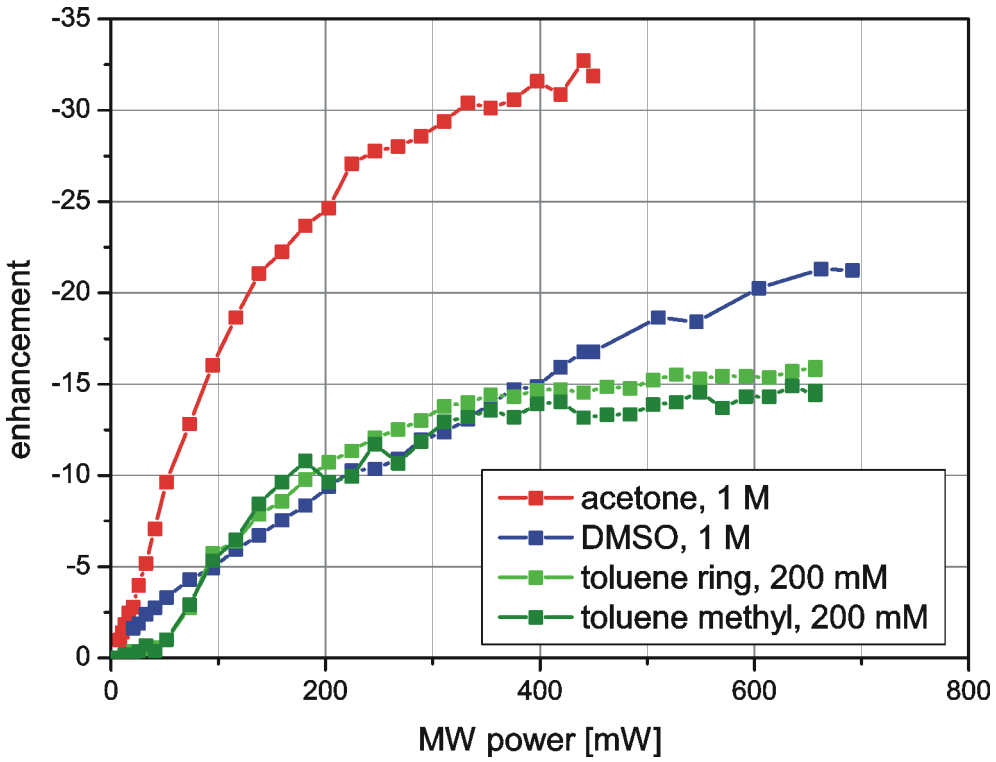

Figure 3.9: DNP enhancement for the methyl protons of acetone, the methyl protons of DMSO and both the ring and the methyl protons of toluene plotted against incident microwave power. The enormous differences in coupling factor predicted by the force free model are not reflected in the enhancements. The acetone and the DMSO sample were both doped with 1 M TEMPOL and put in a 20 μm ID capillary, while the toluene sample was doped with 200 mM (due to the lower solubility) and placed in a 30 μm ID capillary.

3.2.3 Beyond Solvents: DNP on Metabolites

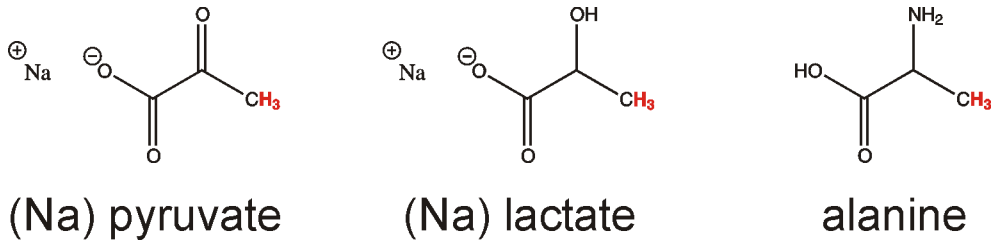

Figure 3.10: Chemical structures of the metabolites Na-pyruvate, Na-lactate and alanine. The target nuclei in the DNP experiments are highlighted in red.

The use of high magnetic field strength renders a larger NMR sensitivity and spectral resolution. This opens the possibility for new applications, like biomolecular research, since different nuclei on different molecules can be distinguished by their chemical shift. However, so far, only DNP experiments with solvent molecules as hyperpolarization targets have been presented here. In fact, until recently, *all* liquid state DNP experiments at high fields have been limited to detecting the solvent itself, not molecules in solution. This is due to the small sample volumes and low filling factors leading to a poor SNR compared to commercial liquid state NMR probes at this field. This relatively poor SNR is sufficient to observe the signal from the highly concentrated solvent nuclei of a sample, but it makes it hard to observe a signal from any compound at low concentration, such as a molecule in solution. However, the more interesting target molecules for DNP, especially with regard to imaging, are molecules in solution. This is particularly true for metabolites, such as pyruvate, lactate and alanine, because they have already been shown to be a promising hyperpolarization target in metabolic imaging.[34,68] Their chemical structures are depicted in figure 3.10. Pyruvate in particular is ideal for metabolic imaging using hyperpolarization because of the long T_{1n} value of its $^{13}C_1$ nucleus and because it is at the entry point to several important energy and biosynthetic pathways.[69]

To investigate how efficiently these molecules can be polarized in solution by liquid state DNP, experiments were performed on Na-pyruvate, Na-lactate and alanine in water solutions, doped with 12 mM ^{14}N-TEMPOL radical.[70] These metabolites range from 89 to 112 Da in weight and exhibit good water solubility, which makes it possible to reach 1 M concentration without any aggregation. Furthermore these compounds are temperature stable and can

withstand the sample heating caused by microwave irradiation during a DNP experiment. Because of this and their importance in metabolic imaging, they are ideal for the investigation of liquid DNP polarization transfer to small target molecules in solution.

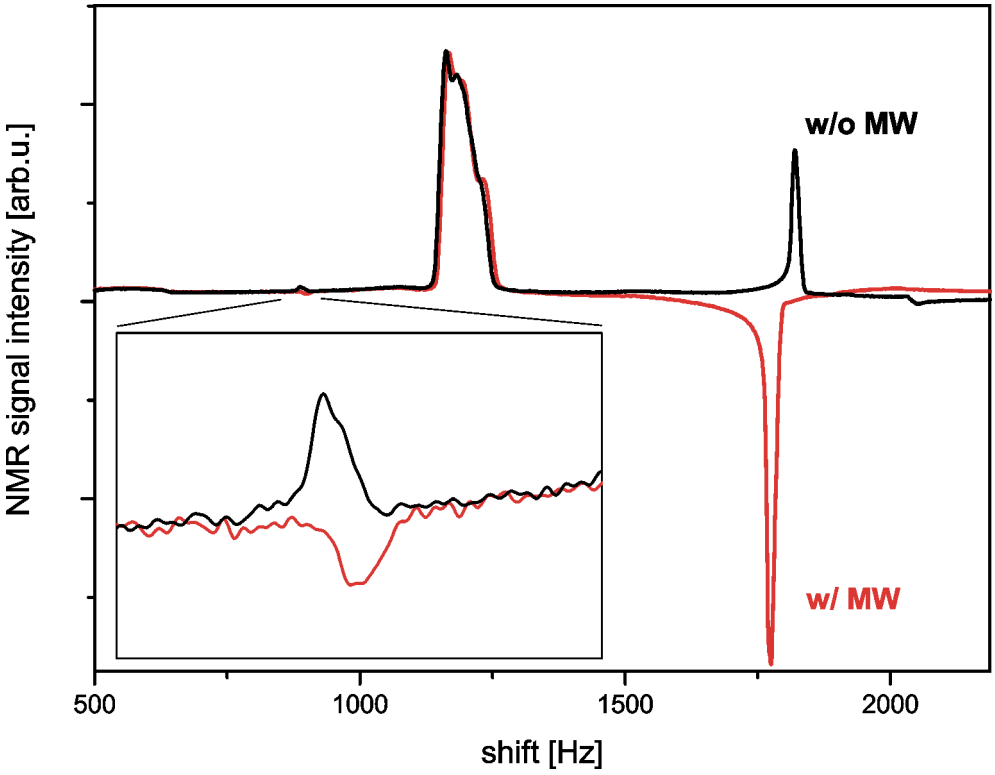

Figure 3.11: ^{1}H-NMR spectra of 1 M Na-pyruvate and 12 mM TEMPOL in water, with (red) and without microwave irradiation (black), respectively. The inlay shows the (direct) polarization of the CH_3 protons of the pyruvate (line at 900 Hz shift), the enhancement being -1.6. The enhancement of the water protons (peak at 1600 Hz shift) is -3.9, corresponding to results with water-TEMPOL solutions. The spectra were obtained using 8192 scans. The temperature of the sample inside the resonator is approximately 15 °C above room temperature during microwave irradiation. The large unchanged peak at 1200 Hz shift is due to water outside the DNP resonator.

Water protons feature a concentration of 110 mol/l, while the three methyl protons of these metabolites in 1 M solution add up to 3 mol/l. So in this case, the corresponding ^{1}H-NMR signal is less than 3 % of the water proton signal from the solvent. In consequence, the spectra were taken using

8192 scans for averaging, to be able to observe the signal from methyl group of the metabolites with a good SNR. Because such an experiment requires stable DNP conditions over a long period of time, the 45 mW solid state source was used.
When the central TEMPOL hyperfine line is irradiated with microwaves, the enhancement that can be observed on the water protons is comparable to the enhancements achieved for TEMPOL in water solution with the same radical concentration. The absolute enhancements are rather small because of the low microwave power used, which does not allow full saturation of the electron spin transition. Additionally, an enhancement can be observed on the signals from the methyl group on the metabolite, as shown for pyruvate in figure 3.11.

Hence, liquid state DNP can indeed polarize such a metabolite in solution. To explain this, several polarization transfer pathways are imaginable: The polarization could be transferred via the solvent protons, or directly. This is depicted in figure 3.12.

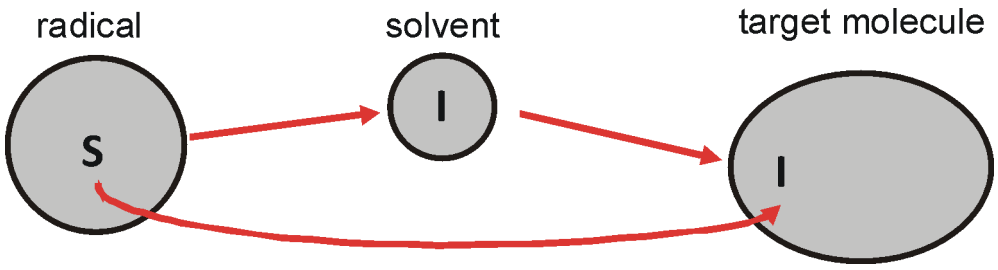

Figure 3.12: Possible polarization transfer pathways between radical and target molecule.

To explore, which pathway is active and which is not, the proton content of the solvent water was varied, i.e. the metabolites were each dissolved in 3 different solvents: Either pure water, 99.9 % deuterated water (i.e. D_2O) or partially deuterated water with roughly 3 M water proton concentration, i.e. comparable to the methyl proton concentration of the metabolites. As a result, the water proton peak in the ^{1}H-NMR spectra is drastically reduced. The effect in the pyruvate methyl proton peak of the can be observed in figure 3.13.

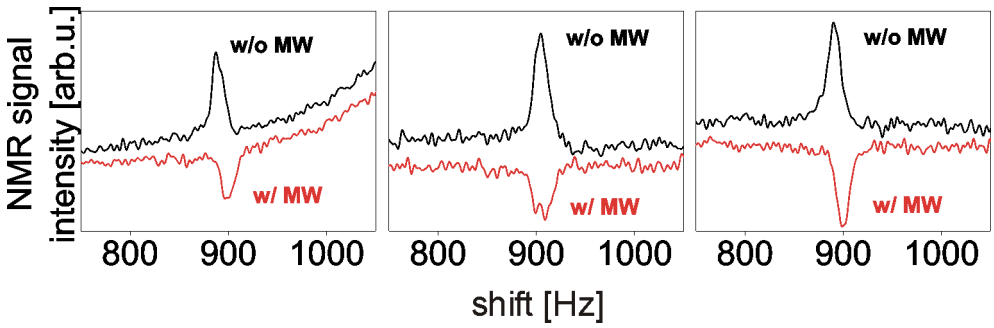

Figure 3.13: ^{1}H-NMR spectra of the CH_3 protons of 1 M (sodium) pyruvate solution in protonated water (left), partially deuterated water (middle) and 99.9 % deuterated water (right), containing 12 mM ^{14}N-TEMPOL radical with (red) and without microwave irradiation (black), respectively. The spectra were obtained using 8192 scans. The achieved enhancement is practically unchanged: -1.6 for water (left), -1.5 for partially deuterated water (middle) and -1.7 for 99.9 % deuterated water (right).

As can be seen, the enhancement on the methyl protons of pyruvate is effectively unchanged. This proves experimentally that the enhancement on the methyl protons of pyruvate is not mediated by hyperpolarized water protons. The pathway via the water protons in figure 3.12 is apparently inactive. This finding is concordant with results at lower magnetic field, where direct ^{13}C polarization on small organic molecules, benzene and chloroform, without mediation via abundant proton spins was observed.[71]
The argument is reinforced by performing an NMR experiment, where the water proton peak is diminished by a 20 s presaturation pulse before recording the ^{1}H-NMR spectrum and comparing it to the spectrum without the presaturation pulse: While the water proton peak is significantly diminished by the presaturation pulse, the methyl proton peak of pyruvate remains effectively unchanged, as can be seen in figure 3.14.

In consequence, the direct polarization transfer from the electron spins to the methyl protons and the water protons can both be treated with equation 2.46, respectively. The gyromagnetic ratios are the same for both systems, because only protons are involved. The same holds for the saturation factor s, which is equal for both target nuclei, since it is one and the same experiment. The leakage factor f can be determined individually for both kinds of protons by determining their respective T_1 values with and without radicals, respectively, in an inversion recovery experiment, as explained in subsection 2.1.5. The leakage factor is practically unaffected by the deuteration of the solvent, e.g. for the pyruvate methyl protons $f = 0.925 \pm 0.028$ for all three

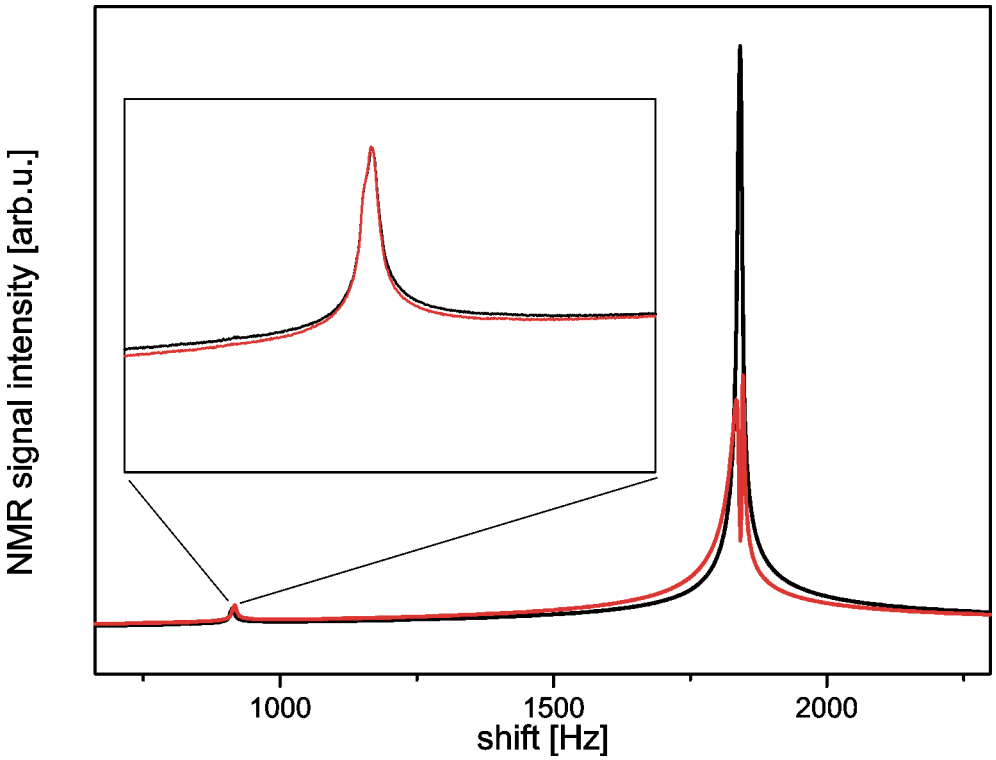

Figure 3.14: ^{1}H-NMR spectra of the CH_3 protons of 1 M pyruvate solution in H_2O containing 12 mM TEMPOL radical with and without a 20 s pre-saturation pulse at the water proton resonance frequency, respectively. The inlay shows the pyruvate CH_3 peak. While the water peak is significantly suppressed, the magnitude of the CH_3 peak is effectively unchanged. The spectra were obtained using 16 scans.

solvents. So finally, by setting up equation 2.46 for both kinds of protons and dividing the two, the unknown and hard to access saturation factor s cancels out and the ratio of the coupling factors of the individual protons ξ_{H_2O} and ξ_{CH_3} can be obtained.

$$\begin{aligned} \frac{\epsilon_{H_2O}}{\epsilon_{CH_3}} &= \frac{\frac{\gamma_S}{\gamma_I} \cdot f_{H_2O} \cdot s \cdot \xi_{H_2O}}{\frac{\gamma_S}{\gamma_I} \cdot f_{CH_3} \cdot s \cdot \xi_{CH_3}} \\ \Leftrightarrow \frac{\epsilon_{H_2O} \cdot f_{CH_3}}{\epsilon_{CH_3} \cdot f_{H_2O}} &= \frac{\xi_{H_2O}}{\xi_{CH_3}} \end{aligned} \tag{3.1}$$

The enhancement factors that were obtained for the methyl protons of the three metabolites are depicted in table 3.4.

substance	ϵ_{CH_3}	$\frac{\xi_{H_2O}}{\xi_{CH_3}}$
(Na-) pyruvate	-1.6 ± 0.1	2.4 ± 0.2
(Na-) lactate	-1.0 ± 0.1	3.5 ± 0.4
alanine	-0.7 ± 0.1	5.3 ± 0.8

Table 3.4: Enhancement factors and coupling factor ratios for (sodium) pyruvate, (sodium) lactate and alanine in water samples.

Although the three metabolites are roughly the same weight and size, their respective methyl proton coupling factor ratio to water protons differs significantly. More striking, however, is the fact that considering pyruvate the coupling factor to its methyl protons ξ_{CH_3} is only a factor 2.4 smaller than ξ_{H_2O} to water protons .
For a simple hard sphere model equation 2.55 can be used to calculate a correlation time between the respective molecules. Assuming the distance of closest approach d to be the same for both polarization targets and a $\tau^{-\frac{3}{2}}$ decay of the coupling factor,[56] this yields

$$\frac{\xi_{H_2O}}{\xi_{CH_3}} = \left(\frac{\tau_{H_2O}}{\tau_{CH_3}}\right)^{-\frac{3}{2}} = \left(\frac{D_S + D_{H_2O}}{D_S + D_{CH_3}}\right)^{\frac{3}{2}} \quad . \tag{3.2}$$

With the room temperature diffusion coefficient for water $D_{H_2O} = 2.3 \cdot 10^{-9} \frac{m^2}{s}$,[72] for the pyruvate ion $D_{CH_3} = 0.44 \cdot 10^{-9} \frac{m^2}{s}$,[73] and using the diffusion coefficient of 4-oxo-TEMPO for the TEMPOL $D_S = 0.41 \cdot 10^{-9} \frac{m^2}{s}$,[74] a coupling factor ratio of 5.7 is calculated, compared to an experimental value of 2.4. Performing this calculation with a decay of τ^{-2} [57] renders a coupling factor ratio of 10.2. Due to the sample heating under microwave irradiation, our sample temperature is approximately 40 °C, 15 °C above room temperature. While the diffusion constants increase with higher temperature, they are assumed to scale with the solvent diffusion constant. In consequence, the obtained ratio of coupling factors can again be compared.
In other words, the measured coupling between the pyruvate methyl protons and the electron spin of TEMPOL is stronger than expected theoretically from the diffusion coefficients, using this approach. This might show, that local dynamics of the DNP agents/target system play an important role for the DNP enhancement at high magnetic fields.[56]

3.3 Conclusion and Outlook

The results presented in this chapter prove that significant Overhauser enhancements up to ≈ -80 can be achieved at a high magnetic field of 9.2 T for TEMPOL in water solutions. This shows that despite the predicted decline of the coupling factor ξ with increasing magnetic field, liquid state DNP at these fields is not only feasible but actually lucrative. However, the technical challenges for DNP at these fields and thus frequencies are considerable. Additionally, strong limitations, particularly small sample sizes and high sample temperatures, apply.

These results are very promising for an eventual application of liquid state DNP at high fields. In particular, this holds for samples, where the small sample size is less of an issue, because the amount of available sample is restricted in the first place.

With regard to the main aim of this work, the application of liquid state DNP in an MRI tomograph operating at 1.5 T, these results are promising as well. Firstly, they prove the feasibility and effectiveness of Overhauser DNP at elevated field strength, an important prerequisite for a successful attempt at 1.5 T.

Moreover, it was shown that considerable enhancements can not only be expected on water protons, but on metabolites as target molecules. Considering the impact of hyperpolarized metabolites in the field of metabolic imaging, this again manifests the high potential of this method.

Chapter 4

DNP for MRI

This chapter deals with the application of hyperpolarization, in particular liquid state DNP, with the aim of enhancing sensitivity and contrast in MRI. In the first section two alternative approaches to hyperpolarization for MRI applications are introduced, PHIP and hyperpolarized noble gases. The second section deals with the application of DNP for MRI applications, both in the solid and in the liquid state, and introduces our approach. The next section describes the hardware that was developed for this task and its features. In the fourth section, the experimental results are presented and discussed before a conclusion and an outlook is given in the final section.

4.1 Other Hyperpolarization Methods

Liquid state DNP via the Overhauser effect is not the only means of hyperpolarizing nuclei. For comparison purposes, a very brief overview over other approaches will be given here. The other three DNP mechanisms, which are of importance for hyperpolarization in the solid state, PHIP and hyperpolarized noble gases are all powerful approaches with applications in MRI.

4.1.1 PHIP

Para-**H**ydrogen **I**nduced **P**olarization ("PHIP") is a chemical approach to hyperpolarization.[7,9] While hydrogen gas in thermal equilibrium at room temperature consists of only 25% para-hydrogen, it is thermodynamically favored over ortho-hydrogen and can therefore be enriched by cooling. Para-hydrogen in its singlet state exhibits a non-Boltzmann spin population with very high spin alignment which can be embedded in unsaturated molecules

through fast chemical reactions.[75] This high proton polarization can subsequently be transferred via the J-couplings to hetero nuclei such as ^{13}C or ^{15}N by adequate pulse sequences, e.g. INEPT.
Compared to the DNP methods of hyperpolarization, PHIP has the advantage of being technically much less demanding, because it requires no microwave irradiation and thus none of the advanced microwave technology. It does however require the possibility to chemically bond the para-hydrogen, therefore, it is limited to substances with unsaturated bonds.

4.1.2 Hyperpolarized Noble Gases

Imaging of organs with air spaces, notably the lungs, is notoriously difficult with protons, so filling this space with a gas giving an MRI signal provides an alternative. However, performing MRI on gases is technically a challenge, because the spin density is very low compared to e.g. the typical case of tissue water. This amounts to a typical factor of 10^3 in signal loss from the lower density.[76,77]
Fortunately, the signal loss from the spin density can be more than compensated by hyperpolarization. These experiments are almost exclusively performed on ^{129}Xe and ^{3}He, the only two non-radioactive noble gases with nuclear spins of $\frac{1}{2}$. The hyperpolarization can be achieved through collisional spin exchange with optically pumped alkali metal vapor ("SEOP"):[78]
The sample contains both the noble gas and a rubidium vapor, which is irradiated with circularly polarized 795 nm laser, resulting in a polarization of the rubidium spins. Spin exchange upon collision transfers this polarization to the noble gas, resulting in a polarization 10^5 times above the thermal equilibrium value.
Another option for the hyperpolarization of ^{3}He is Metastability Exchange Optical Pumping ("MEOP").[79–81] In this method, an electric discharge excites ^{3}He atoms from the ground state into a metastable excited state. Then, the ^{3}He gas can be optically pumped by a circularly polarized laser light at 1083 nm.
Additional to their nonreactivity, noble gases such as ^{129}Xe and ^{3}He are particularly amenable for hyperpolarization, due to their very long relaxation times of tens of minutes to tens of hours.[82,83]
An example of a medical application of hyperpolarized ^{3}He gas is shown in figure 4.1.

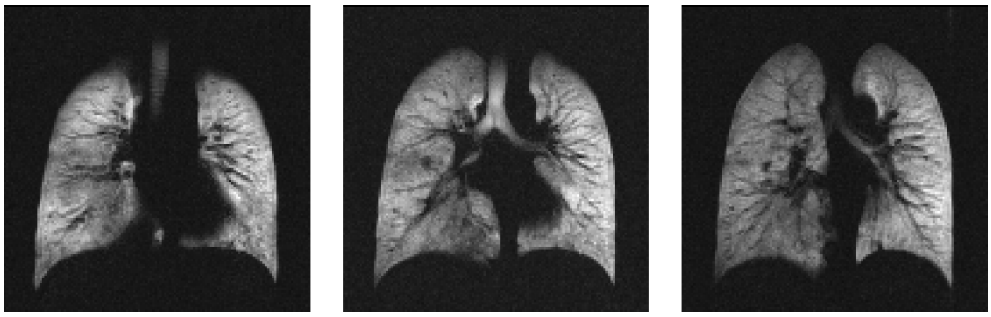

Figure 4.1: Three ^{3}He image slices of the author's lungs. Because the lungs are filled with the hyperpolarized ^{3}He gas, the signal is obtained from the lung cavity itself. Hence, the shape of the lungs, the trachea and the heart shadow can be clearly seen. Data by courtesy of Section of Medical Physics, University Medical Center Mainz.

4.2 Concept

MRI provides spatially and temporally resolved information about spin density, e.g. proton (^{1}H) or carbon (^{13}C) spins, and their chemical environment. Because of the low energy of the excitation (in the radio frequency range) the method is noninvasive and does not require chemical alteration of the sample or application of ionizing radiation. On the other hand this leads to low sensitivity and contrast, limiting the spatial and temporal resolution of the method.

Typically, contrast is enhanced by administering specific contrast agents, which significantly shortens the longitudinal and transversal relaxation times T_{1n} and T_{2n} of the nuclei close to it. Sensitivity can be improved by different techniques, such as optimization of hardware and acquisition parameters, or the use of higher magnetic field, which increases the energy splitting of the involved nuclear spins and therefore the Boltzmann polarization (see equation 2.9). For larger objects this is technically very challenging and thus increasingly expensive, but also practically limited by the effects of the large magnetic fields and high-frequency excitations, for example on the human body or on neuronal transmission.[84,85]

A different approach tackling both issues simultaneously is hyperpolarization, i.e. creating a non-Boltzmann nuclear polarization. As explained in section 2.3 and 4.1, hyperpolarization can be achieved by several methods and mechanisms, such as PHIP,[7,9] laser polarization of e.g. ^{129}Xe gas[86] or DNP.[87–89]

However, the hyperpolarization in these approaches is not performed on the

imaging object itself, but on a sample, which is then transported to the imaging site and injected or applied in a bolus-like fashion. Therefore, for the injection it has to be either a liquid or, in the case of ^{129}Xe and ^{3}He, gaseous. Depending on how and where the hyperpolarization is created, these approaches differ significantly.

4.2.1 Dissolution DNP

Dissolution DNP is an approach, where hyperpolarization is achieved in an external magnet (typically 3.4 T, 95 GHz for EPR excitation), i.e. spatially separated from the imaging magnet, in the solid state at low temperatures by the mechanisms described in subsection 2.3.5.[90–93] After a typical polarization buildup time of more than 30 minutes, the sample is quickly heated to room temperature and dissolved in about a second. As a liquid sample it is then shuttled into the imaging magnet for the MRI application, e.g. metabolic imaging.[93] Performing the hyperpolarization under these conditions is optimal for high signal enhancements, e.g. of ^{13}C, because additionally to the DNP effect a Boltzmann enhancement from the temperature jump is obtained. Therefore, enormous signal enhancements (> 10000 [87]) can be achieved on relatively large sample volumes (up to 100 ml[92]) on a broad range of target molecules, creating entirely new possibilities and fields of application.
However, the requirement to shuttle between two magnetic fields practically prohibits the use of nuclei with short relaxation times, like ^{1}H. Also, the long polarization buildup time makes this approach a single shot procedure, i.e. the experiment cannot be repeated quickly due to the slow buildup time causing a slow repetition rate.

4.2.2 Liquid State DNP

In contrary, performing the hyperpolarization in the liquid state, allows for an operation in continuous mode, delivering a constant flow of hyperpolarized sample. The polarization transfer mechanism effective in liquids relies on cross-relaxation between the electron and the nuclear spin, which works most efficiently at low magnetic fields.[20] Liquid DNP experiments for MRI application have been realized at a polarizing magnetic field of approximately 0.35 T, corresponding to an EPR frequency of approximately 9.8 GHz ("X-band"). They used either a separate polarizing magnet[94] or incorporated the polarizer setup in the fringe field of the imaging magnet.[95] Liquid state DNP

enhancements at X-band have been reported as high as -170, for sample sizes of about 6 μl.[38]
However, in the case of an external X-band polarizer, the polarization achieved at the imaging site is scaled down by the factor between the polarizing and the imaging field. In the particular case of an X-band polarizer and 1.5 T imaging field this scaling factor is roughly 1/5.
Additionally, in both cases of external polarizers, the shuttling through a field gradient might induce coherent and incoherent magnetic field effects on the polarization[96] and lead to relaxation losses during shuttling, resulting in distorted spectra.
Here we choose a different strategy: We use the very same 1.5 T field of the imaging magnet as our polarizing field, putting an EPR resonator, used for the polarization transfer, very close to the imaging object.[97,98] This not only fully eliminates the Boltzmann penalty, but does not require sample shuttling through static field gradients and over long distances, either. It does however require the use of a higher microwave excitation frequency of 42 GHz, compared to the 9.8 GHz used for the previously described approach. Considering the field dependence of the DNP efficiency, we compare our results obtained at 42 GHz with former published results obtained at X-band.

4.3 Hardware

This section describes the hardware that was developed in this project. The first subsection discusses the two hardware setups with an electromagnet and an MRI scanner, respectively. Then, the layout of the microwave source and the issue of power transmission is discussed. The next subsection deals with the heart of the DNP polarizer, the microwave resonator, followed by the NMR detection. Finally, the flow though system and the topic of RF compatibility are explained.

4.3.1 General Setup

In this work, two different setups were used for DNP experiments at 1.5 T:
In the first development stages of the project, the experiments were performed in a commercially available electromagnet (BE-33, Bruker). This magnet can reach a maximal field strength of approximately 1.3 T in its normal configuration, but can be equipped with specialized pole tips which raise the maximum above 1.5 T, while sacrificing space and some field homogeneity. In this setup, a probe head is used to host the DNP polarizer and NMR

detection (discussed later in subsection 4.3.5) and fix it in the magnetic field. All experiments not involving MRI were performed in this setup. Its general layout is depicted in figure 4.2.

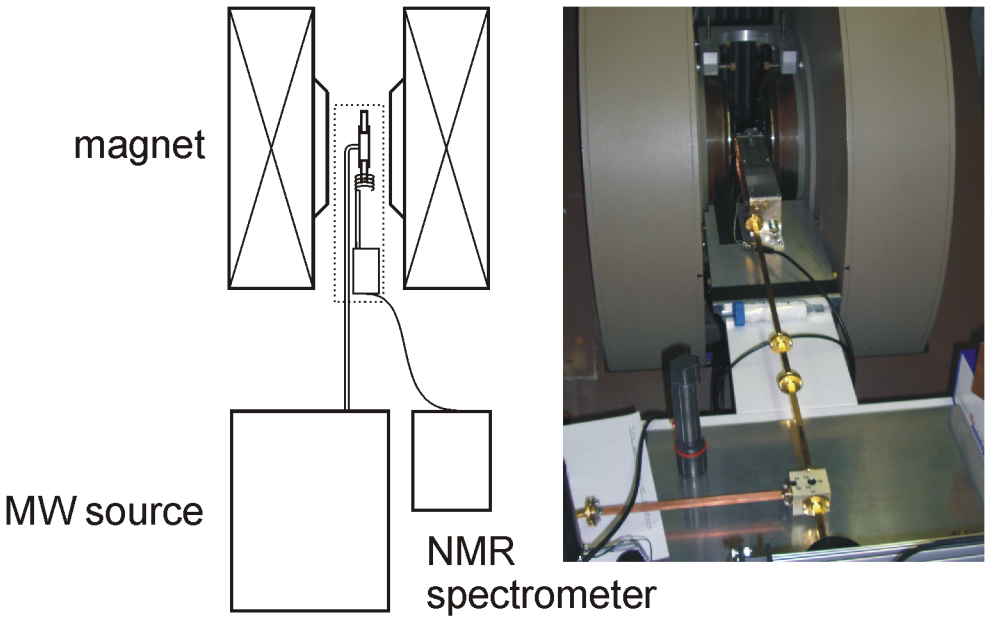

Figure 4.2: The experimental setup using the electromagnet. The extra pole tips allow a field strength of 1.5 T. The probe head, which contains the EPR resonator, the NMR detection coil and the NMR tuning circuit, is held in place by a supporting structure, which is fixed to the magnet. Since no large stray field exists, the microwave source can be placed close to the magnet, ≈ 50 cm from the resonator.

To be able to perform MRI after hyperpolarization through DNP, the DNP system has to be incorporated to an MRI scanner. The principle setup of this system is shown in figure 4.3 both schematically and as a photo.

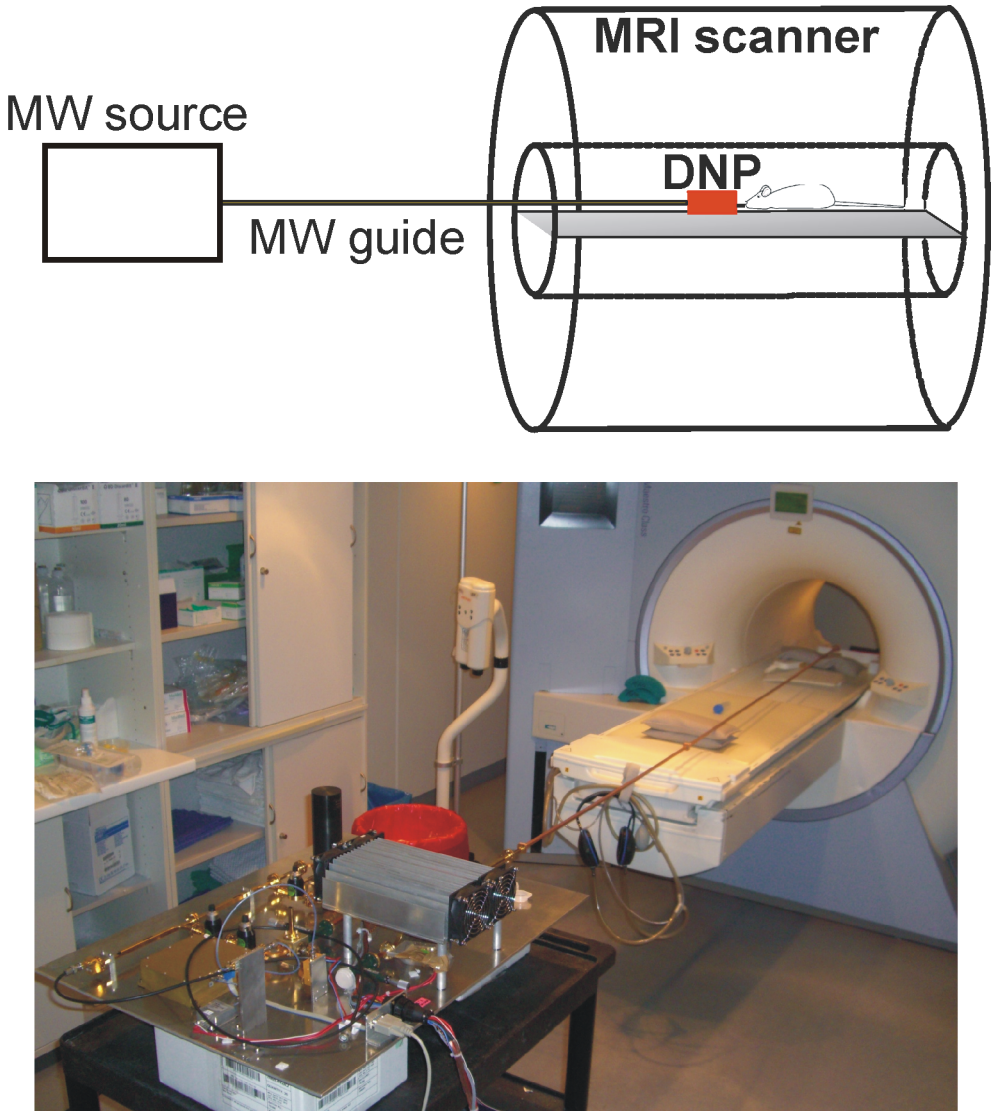

Figure 4.3: The principle setup of the DNP system in the MRI scanner: The DNP polarizer is placed inside the bore of the imaging magnet, right next to the imaging object, represented by a mouse. The microwave source is placed well outside the bore, keeping it out of the large stray field. Power transmission is accomplished via a 3 m piece of waveguide.

The DNP polarizer is placed inside the bore of the imaging magnet, right next to the imaging object.[97–99] The microwave source is placed well outside the bore, keeping it out of the large stray field. The transmission of the microwave power is accomplished via a 3 m piece of waveguide leading from the source to the polarizer. Because the MRI excitation and detec-

tion is performed by integral parts of the MRI scanner setup, no additional NMR equipment is necessary. Therefore, no probe head as such exists, but a wooden structure to support the soft waveguide. The equipment is additionally fixed in place with sandbags.

4.3.2 The Microwave Source

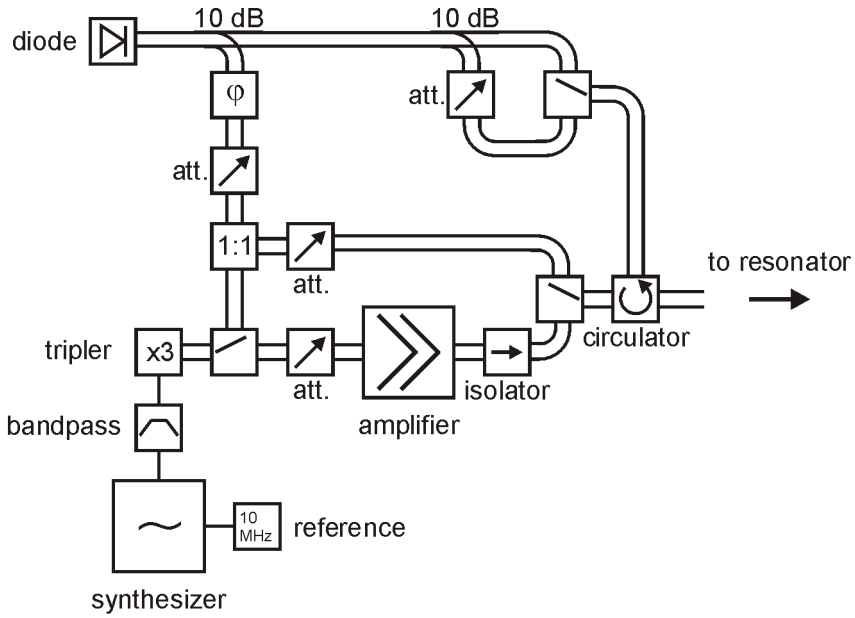

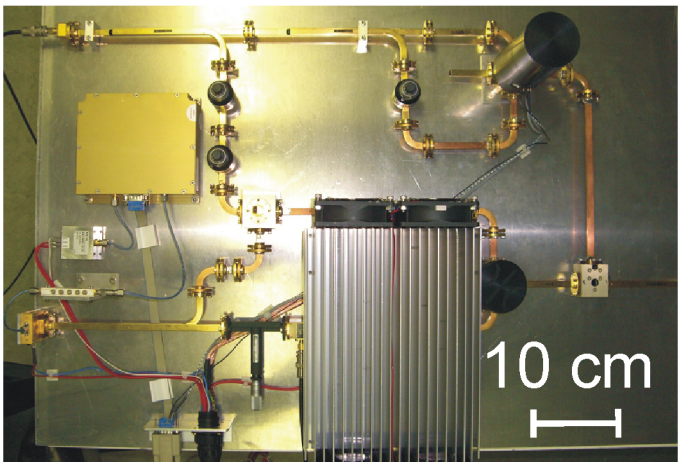

Figure 4.4: Block diagram and photo of the microwave source. The waveguide switches are shown in position for the low power tuning mode.

A boxplot of the source setup is depicted in figure 4.4. The primary microwave source is a synthesizer (SNP 1216-520-02, Gigatronics) with a frequency stability of 10^{-7} $\frac{1}{\mathrm{h}}$. This is achieved by an external 10 MHz reference (AXIOM90-12-25, Axtal). The synthesizer can be accurately tuned from 12 to 16 GHz with a maximum power output of 17 dBm. This output power is attenuated down with a fixed 9 dB attenuator (WA4H/18-9-12, Mi-Wave) and a bandpass filter (BP-14000-4000-10CS, BL Microwave) is employed to discard any unwanted spurious modes. Subsequently, an active frequency tripler (QMM-4305103ZBPF, Quinstar) is fed, bringing the frequency output to a tuning range of 40 to 45 GHz at a power of approximately 13 dBm. Additional to CW operation, this combination can be used to perform fast frequency sweeps. This is achieved by dialing an output frequency and triggering on the start of the synthesizer retuning. Typically, the synthesizer tunes to the new frequency in 10 to 20 ms, depending on the size of the frequency step. While the retuning does not render a frequency sweep that is linear in time, it is sufficient for a quasi real time monitoring of the frequency response. This option comes very handy when it comes to observing the cavity resonance "dip", unwanted modes, etc. (see subsection 4.3.4).
Optionally, a power amplifier (QPW-40453334-K0, Quinstar), can be used to boost the power output to a maximum of approximately +34 dBm. The input power is controlled by a variable attenuator (model 23020, FLANN), while its output is protected with a ferrite isolator (QIF-Q00000, Quinstar). When the amplifier is not in use, it is simply bypassed using two mechanical waveguide switches (530B/383, Mi-Wave). Because the amplifier will dissipate most of its power consumption of 120 W in heat, it is mounted to a large aluminum heat sink, which is additionally equipped with 4 cooling fans.
The detection of the reflected microwave power is realized with a detection diode (DQ-2P S/N 7M18, Spacek Labs), via a ferrite circulator (179B-34/383, Mi-Wave). To protect the diode from excessive power, the reflection is first attenuated down to an adequate power level, by transmitting it through an extra attenuator (520B/383, Mi-Wave) via an automatic waveguide switch (535B/383, Mi-Wave), which selects this path when the amplifier is running.

4.3.3 Power Transmission

Some components of the microwave source cannot operate in an external magnetic field. Most notably the ferrite isolator and circulator employ an internal permanent magnet and will not function properly if its magnetic field is overpowered by a strong external magnetic field. They must therefore be kept out of the stray field until it has dropped to their maximal tolerance

value of 50 G. While this is a minor issue for the electromagnet setup with its small stray field, it is a severe issue for the imaging magnet. Figure 4.5 depicts the stray field of a typical 1.5 T imaging magnet.

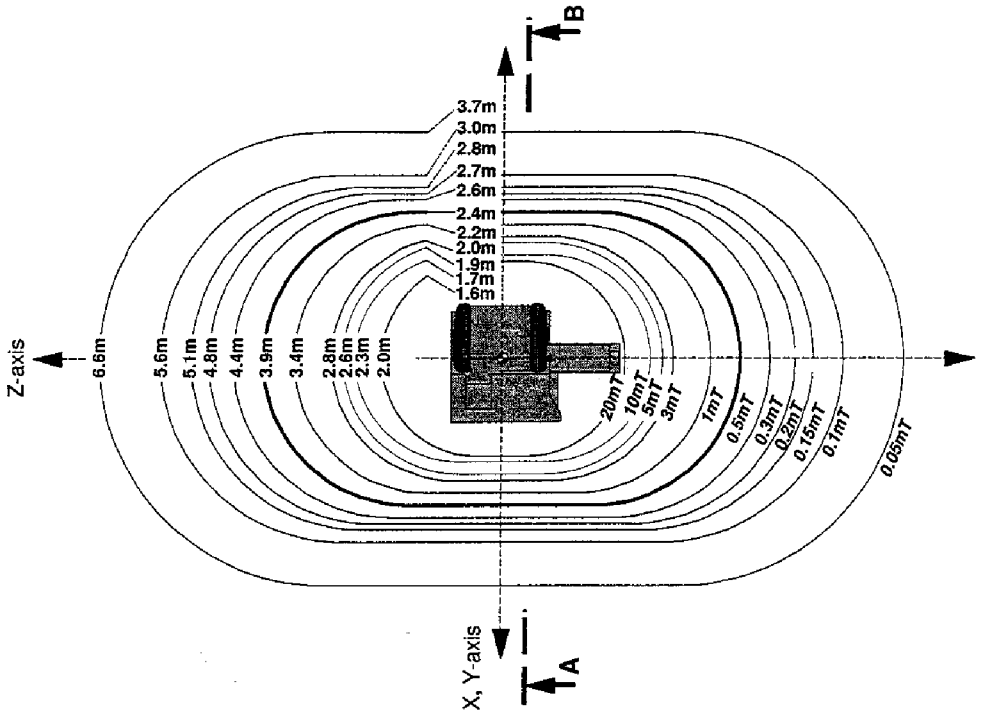

Figure 4.5: Stray field plot of a typical 1.5 T imaging magnet.[100] The 50 G line extends 2.6 m in axial direction, the 5 G line as far as 3.9 m. The source has to be kept in a region below the maximum tolerance value of its most sensitive components at 50 G.

The source setup was built using WR-22 waveguides, but a larger size with less losses per unit of length was chosen for the transmission into the imaging magnet. This is achieved with a 3 m long WR-28 waveguide, made out of nonmagnetic copper. For the connection a WR-22 to WR-28 taper was used. After the WR-28 transition, the waveguide is again narrowed down to a size WR-19 for an efficient coupling through the small iris. The total power losses from the board output to the resonator are below 1 dB. To prevent any disturbance of the magnetic field and attractive forces, the waveguide is made of pure copper, while only brass and aluminum screws were used inside the field.
In the test setup employing the electromagnet, power transmission is less of an issue. Since the stray field of the magnet is significantly smaller, the

source can be placed much closer to the resonator, so the microwave power only has to be transferred over approximately 500 mm, compared to over 3 m for the imaging setup. For this purpose, likewise to the board WR-22 waveguide was used.

4.3.4 The Resonator

We designed and constructed a cylindrical TE_{011} microwave cavity ("resonator"), tunable from 41 to 43 GHz. It consists of a hollow bore cylinder, OD 11 mm and ID 9 mm, and two movable plungers on both ends, that can be screwed in and out for frequency tuning. It is depicted schematically in figure 4.6.

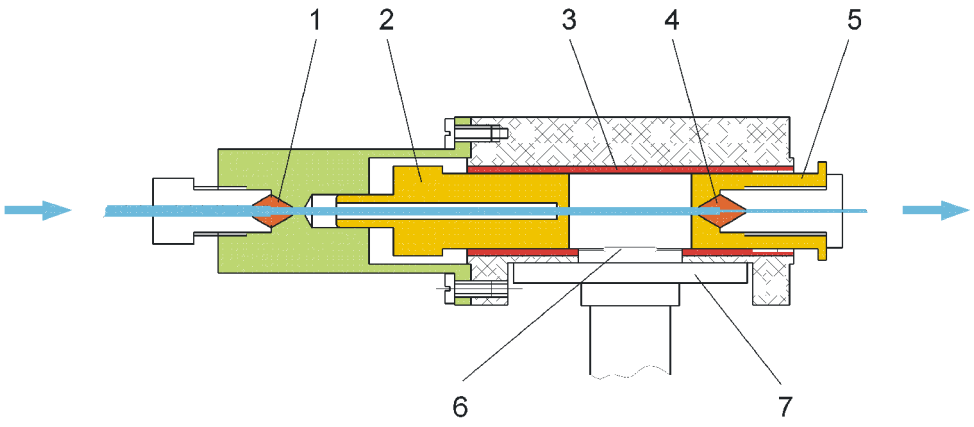

Figure 4.6: Schematic drawing of the resonator design: (1) conical squeeze joint, Polytetrafluoroethylene ("PTFE")/Teflon®; (2) plunger, nonmagnetic brass, 2 μm silver coating; (3) hollow bore cylinder, ID 11 mm, nonmagnetic brass, 2 μm silver coating; (4) capillary necking; (5) plunger, nonmagnetic brass, 2 μm silver coating; (6) slit iris, 5.6 mm long, 0.20 to 0.30 mm wide; (7) WR-19 waveguide flange, copper.

The distance between the plungers, i.e the cavity length of a cylindrical

cavity for a TE mode is given by[101]

$$d = \frac{\pi}{\sqrt{\frac{2\pi\nu_{ijk}}{c}^2 - \frac{p'_{ij}}{a}^2}} \quad , \tag{4.1}$$

where $\nu_{ijk} = \nu_{011} = 42$ GHz is the frequency of operation, $c = 3 \cdot 10^8 \frac{\mathrm{m}}{\mathrm{s}}$ is the speed of light, $p'_{ij} = p'_{01} \approx 3.832$ is the root of the appropriate Bessel function for the respective indices and $a = 4.5$ mm is the radius of the cavity. For a TM mode, p'_{ij} in equation 4.1 is replaced with p_{ij}. This renders a plunger distance $d \approx 14.2$ mm for the TE_{011}-mode.
With these dimensions for the hollow bore cylinder, only few other modes can occur. Solving equation 4.1 for a and $d \to \infty$ yields the critical radius $a_{crit} = \frac{c \cdot p'_{ij}}{2\pi\nu_{ijk}}$ for the respective indices, i.e. the minimal radius necessary for the mode to exist.
The modes with a critical radius $a_{crit} \leq 4.5$ mm are listed in table 4.1 for TE modes and table 4.2 for TM modes.

i	p'_{i1}	a_{crit} /mm
0	3.832	4.355
1	1.841	2.092
2	3.054	3.470

Table 4.1: a_{crit} for TE_{i11} modes, with $a_{crit} \leq 4.5$ mm.

i	p_{i1}	a_{crit} /mm
0	2.405	2.733
1	3.832	4.355

Table 4.2: a_{crit} for TM_{i11} modes, with $a_{crit} \leq 4.5$ mm.

This demonstrates that while 4 other modes than TE_{011} *can* exist, except for TM_{111} they are well separated from TE_{011}. Therefore, for a cavity length of $d \approx 14.2$ mm, there is only one unwanted mode with a similar frequency. In reality, TE_{011} and TM_{111} prove to be easy to distinguish and TM_{111} is quickly annihilated by the introduction of a lossy water sample.
Because the resonator performance depends greatly on its shape, the accuracy of manufacture is a very important factor. Both the cylinder tube and the plungers are manufactured from brass. The material is first annealed by heating it to ≈ 700 °C for approximately 5 hours, then slowly cooled down. This procedure removes any stress in the material and prevents deforming during and after the machining process. The cylindrical cavity is then drilled

to almost its final diameter and then reamed to its final cylindrical shape. Electrical discharge machining, or "electroeroding" the last tenths of millimeters renders an even more precise cylindrical shape, i.e. a more optimal resonator geometry, which can be seen in the resulting quality factor.
The coupling of the microwaves into the resonator is achieved by a slit shaped iris placed axially in the cavity wall. It is also electroeroded into the material to prevent any deformation of the cylinder shape of the cavity during machining, This easily happens when the iris is drilled through the thin cavity wall. The iris length is equal to the width of the transmission waveguide of 5.6 mm, its width has to be carefully chosen to achieve critical coupling depending on sample permittivity and size. For an iris thickness between 0.20 and 0.30 mm the quality factor ranges from 600 to 1600 for a water sample with a capillary ID between 0.4 to 0.3 mm. A exemplary frequency response for resonator R3 can be seen in figure 4.7.

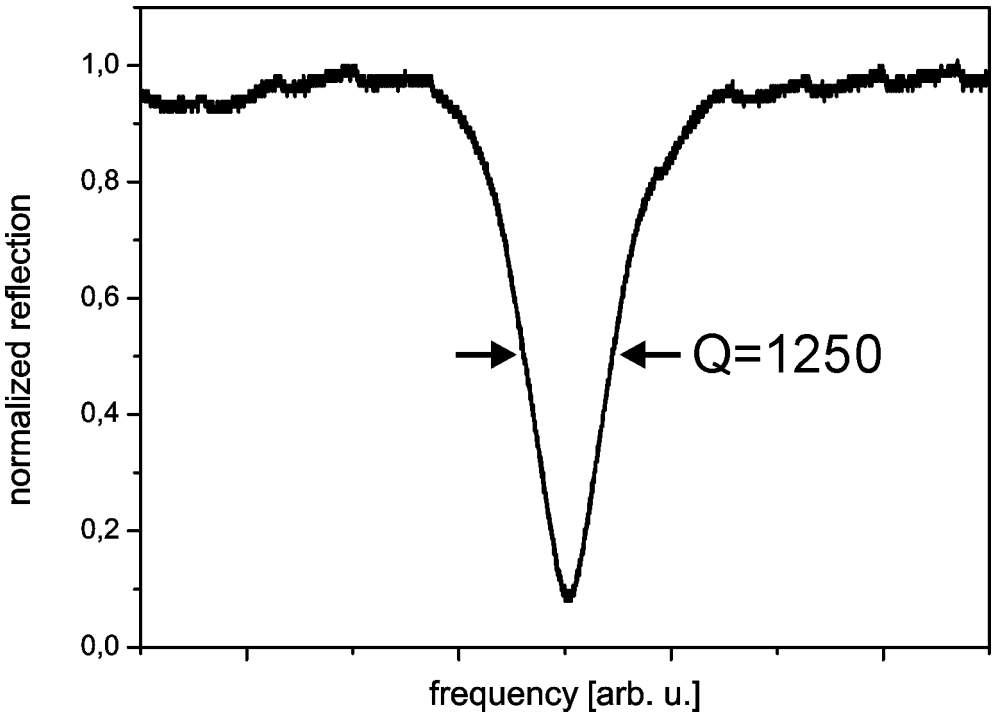

Figure 4.7: plot of the reflected microwave signal versus frequency of resonator R3 loaded with a 0.3 mm ID water sample. The resulting quality factor is ≈ 1250.

To avoid any disturbance of the static magnetic field the cylinder and the plungers of the resonator are made of nonmagnetic brass. While this brass

does not cause much field disturbance and is hard enough to be developed easily, its electric conductivity is roughly a factor of 4 lower than the conductivity of silver, which has the highest conductivity of any metal.[67] To make up for this, we coat the parts of the resonator that host the electric currents, i.e. its walls, with a layer of silver. Since these currents fall off exponentially in the wall with the characteristic distance of the skin depth $\approx$ 100 nm, a silver layer about 2 μm thick is sufficient.
The silver layer is deposited electrochemically on the inside resonator wall and on both plunger faces. The coating solution consists of 5.4 g of AgCN, 9.0 g of KCN and 6.75 g of K_2CO_3 dissolved in 150 ml of water. Because the goal is to plate the *inside* of the cylinder tube, a coaxial Pt-electrode is introduced into it. The cylinder with the electrode is then submerged in the plating solution and the silver deposition is run for 90 s at a voltage of 1.5 V. Subsequently, the parts are quickly rinsed with water and isopropanol to prevent staining.

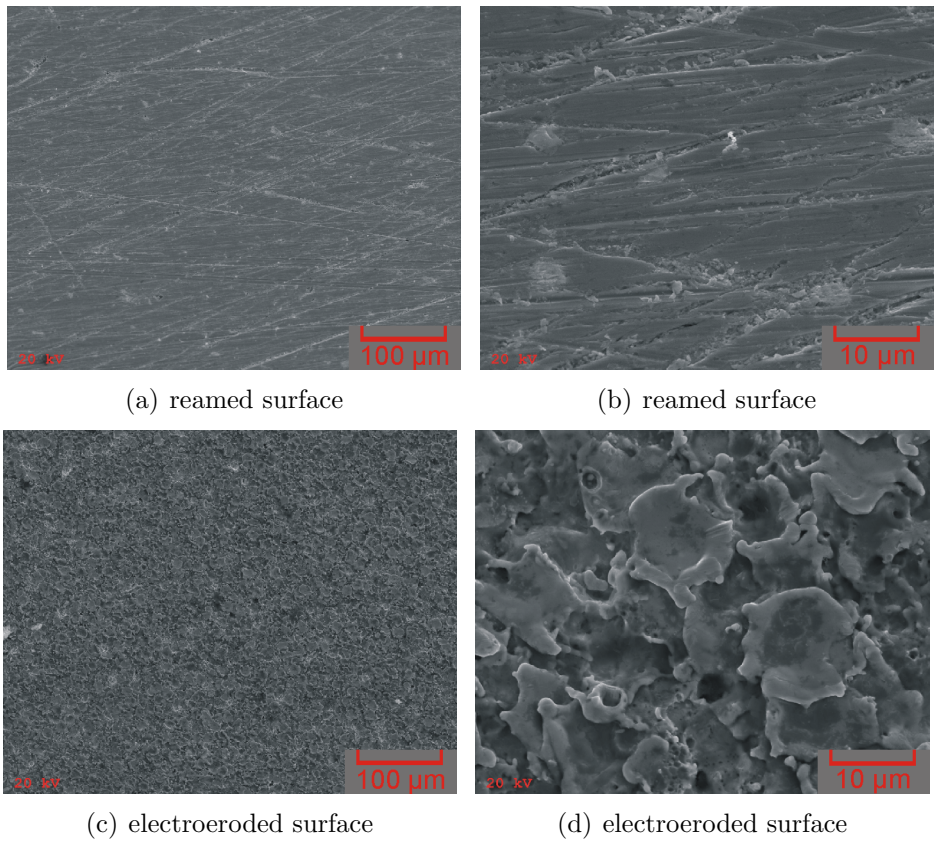

(a) reamed surface (b) reamed surface

(c) electroeroded surface (d) electroeroded surface

Figure 4.8: SEM images of reamed and electroeroded brass surfaces, respectively.

The result of the electroplating process varies, depending on how the surface was developed: A brass surface, that is cut, milled or reamed shows some scratches from the mechanical machining process, but aside from that the surface material is rather smooth. On the other hand, a surface that was electroeroded, does not feature any mechanical scratches, because no mechanical contact is made during the electroerosion. This can be observed on scanning electron microscopy ("SEM") secondary electron images in figure 4.8 (taken on an Atomica Amray 1920 ECO at 20 kV). While the mechanically developed surfaces show scratches and grooves (top), the electroeroded surfaces rather appear molten and pockmarked on a small scale of ≈ 10 μm (bottom).

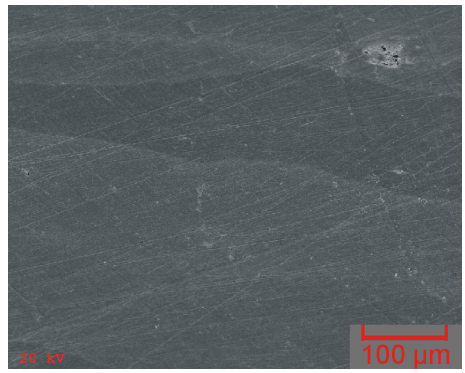

(a) reamed surface

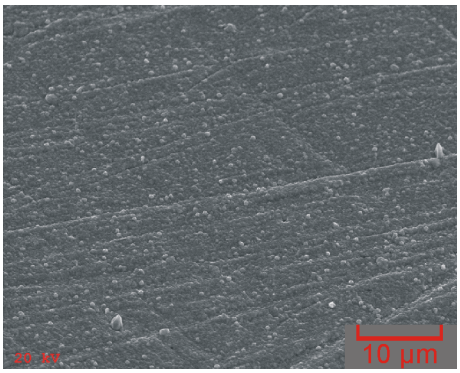

(b) reamed surface

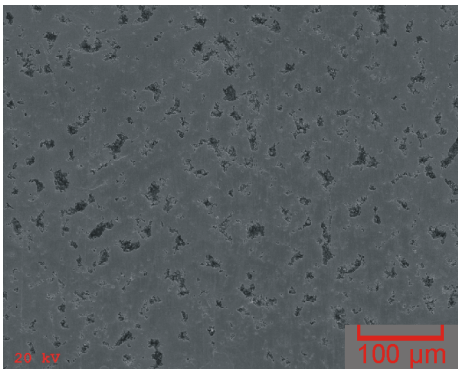

(c) electroeroded surface

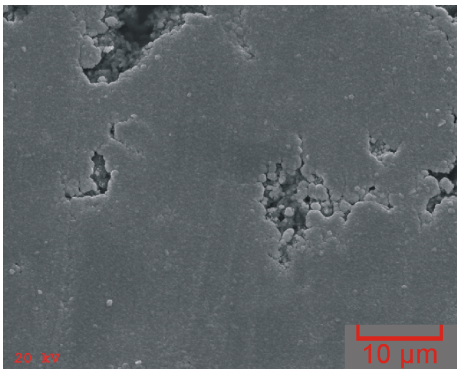

(d) electroeroded surface

Figure 4.9: SEM images of silver coatings on reamed and electroeroded brass surfaces, respectively.

The different surface conditions for the two manufacturing processes strongly affect the electroplating process, which is shown in figure 4.9. While the mechanically developed surface can easily be coated with a smooth silver

layer with hardly any visible graining (top), the silver deposition on an electroeroded piece of brass gives a worse result. The deposition takes place in small batches of silver instead of a smooth layer, i.e. it is grainier (bottom). The resulting silver layer shows small defects.

The coating performance for the two kinds of surfaces can be additionally checked by performing electron micro probe analysis ("EMPA") on the silver layers. In all cases, the results from the analysis of the emitted x-ray spectrum yielded a silver content $> 82\%$ for any part of the coating, including the defects, the remaining percentage being brass. In other words, the deposited layers are in fact pure silver.
As a result of the varying coating performance, the resonators that were made by electroerosion improve their performance not as pronounced as the resonators that were reamed. This can be seen in table 4.3 and 4.4.

type	Q	coupling	reflection
R 3: slit iris 0.20 mm, window slits, drilled	1150	critical	$< 1\%$
R 3 + Ag plating	1340	critical	$< 1\%$
R 4': slit iris 0.20 mm, drilled	1450	overcoupled	$\approx 9\%$
R 4' + Ag plating	1860	overcoupled	$\approx 15\%$
R 5: slit iris 0.20 mm, electroeroded	1600	overcoupled	$\approx 5\%$
R 5 + Ag plating	1740	overcoupled	$\approx 20\%$

Table 4.3: Q-factors for different resonators for 0.3 mm ID capillary samples.

type	Q	coupling	reflection
R 4: slit iris 0.30 mm, drilled, Ag plated	500	undercoupled	$\approx 10\%$
R 6: slit iris 0.28 mm, eroded, Ag plated	450	critical	$< 1\%$

Table 4.4: Q-factors for different resonators for 0.4 mm ID capillary samples.

In conclusion, a brass resonator, that is given its final cylindrical shape by electroerosion performs better compared to a resonator that was merely drilled and reamed, due to its more precise geometry. However, this is more than compensated by applying a silver coating, which works best on the latter kind. So with silver coating, the drilled and reamed resonators perform best.

To be able to detect the DNP polarization inside of the resonator cavity, a resonator version with electro-eroded narrow radial slits in its walls was made. It is depicted in figure 4.10. This design makes it possible to detect the NMR signal inside of the microwave resonator with a pair of saddle coils placed left and right on the outside of the resonator (see 4.3.5). Since there are no axial currents in the resonator walls in this microwave mode, only a relatively small reduction of the Q value to 1300 was observed for a resonator loaded with a 0.3 mm ID water sample (see table 4.3).

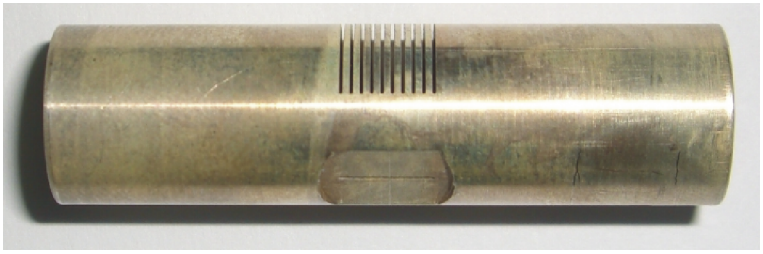

Figure 4.10: Photo of resonator R3 with radial window slits. This design permits the detection of NMR signals inside of the resonator via two saddle coils placed left and right of it.

4.3.5 NMR Detection

^{1}H NMR detection was performed at 1.5 T, i.e. 63.6 MHz, using a commercially available Bruker minispec spectrometer adapted to the homemade NMR coils by a tuning circuit. The principle setup is depicted in figure 4.11.

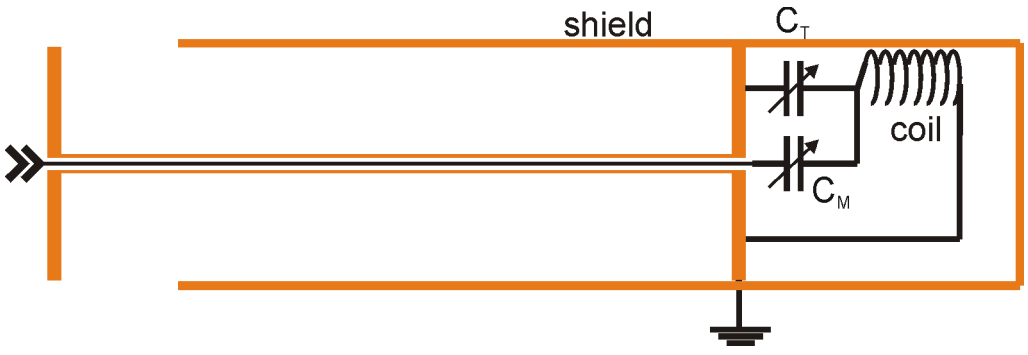

Figure 4.11: Schematic setup of the tuning circuit in the probe head.

The variable capacitors C_T for tuning and C_M for matching are kept as

close as possible to the NMR coil, so the inductance of the circuit is dominated by the coil, i.e. it can have as much inductance as possible. The resonant circuit of the tuning capacitor C_T and the coil is coupled to the spectrometer via the matching capacitor C_M, approximately 250 mm of type 36 semi rigid cable and a type N connector. C_T and C_M can be varied from the back of the probe head via two driving rods. The frame structure of the probe head serves as electric ground as well.
To shield the entire system from RF noise from the outside, the probe head is placed in a copper shield, which contacts the electric ground of the probe head vertical frame via bronze leaf springs. This very effectively shields off most RF noise in the 63 MHz frequency region from the resonant circuit.
To avoid any unwanted ^{1}H NMR signals from parts of the probe head all parts have to be free of protons. For metal or glass parts this is given while the other parts, such as holders, are made of Kel-F® (3M). Kel-F® is a proton free polymer and therefore does not give any NMR signal itself. Additionally it features a very low vapor transmission rate, i.e. it does not absorb any water or oil during machining, which also leads to unwanted NMR signals. This is particularly important for parts close to the detection coil. Small amounts of protonated polymers in capillary or wire coatings can be neglected.

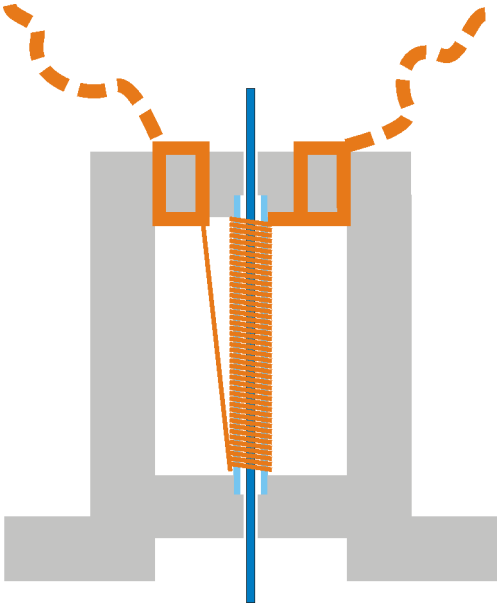

Figure 4.12: The solenoid coil for NMR detection of the sample outside of the resonator. The copper coil (orange) is wound on a quartz capillary (light blue), mounted in a Kel-F® housing (gray) where the leads are anchored with copper wire rings. The sample capillary (dark blue) runs through the holder capillary with the coil on it.

NMR detection of the capillary *outside* of the resonator is achieved with a single solenoid coil. It is wound on a quartz glass tube, with an ID of 1 mm and an OD of 1.6 mm and placed in a housing made of Kel-F®. The leads of the coil are anchored by soldering them to two copper rings in the bottom of

the housing, serving as electrical contacts and a strain relief at the same time. The housing surrounds the entire coil and protects the fragile system from breakage or deformation, which would result in a change in inductance and therefore detuning of the resonant circuit. The housing with the coil is now attached to the resonator housing and the sample capillary is run through the central tube (see figure 4.12).

The detection of the DNP polarization *inside* of the microwave resonator is a more demanding task: Because the walls of the resonator surround this part of the sample it is very effectively shielded from any radio frequency from the outside, such as the NMR frequency of 63 MHz. By using the resonator R3 with radial window slits described above (figure 4.10), NMR detection inside the resonator can be accomplished. It requires a set of saddle coils, placed left and right of the slit microwave resonator. The setup is shown in figure 4.13.

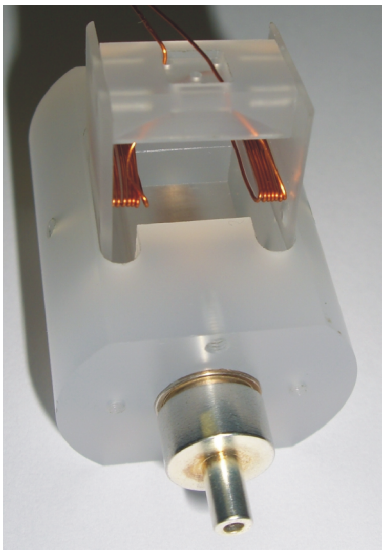

Figure 4.13: Photo of the saddle coil setup for NMR detection of the sample inside of the resonator R3. For better visibility the saddle coils are shown pulled up on their holder.

In both these setups, the quality factor Q of the resonant circuit is approximately 100. However, due to the low filling factor and the obstacle of the remaining resonator walls NMR performance in this setup is poor, yet sufficient to observe the ^{1}H peak of the 800 nl liquid water sample in a 0.3 mm ID capillary. Widening the slits will lead to better NMR sensitivity, but will gradually decrease the resonator quality factor and thus the DNP performance. Since not NMR sensitivity but DNP performance is the focus of this setup, the lack of NMR sensitivity is a minor issue.

4.3.6 MRI Detection

In the imaging setup, MRI detection was performed by a commercially available 1.5 T MRI tomograph (Magnetom Siemens Sonata), using the standard Siemens pickup loop coil with a radius of approximately 20 mm ("finger coil"). The imaging coil is placed in the transversal plane adjacent to the DNP resonator, approximately 80 mm downstream, in the isocenter of the magnet. That way, minimal transport times are achieved. At the same time the coil is not perturbed by any of the DNP equipment, because of its sensitivity profile, limiting the coil to approximately its radius in both directions. Spoiled Gradient Recalled Echo ("SGRE") and Spin-Echo ("SE") pulse sequences were used to acquire images.
The resonator is also subject to the field gradients used during imaging sequences and is therefore momentarily off resonance when gradients are applied. However, this is only the case for very short periods below the echo time TE = 9 ms, yielding a maximum "off-resonance" time $< 10\%$. Additionally, and the field fluctuations amount to less than 4 G over the resonator length, which corresponds to the EPR linewidth. In conclusion this does not play a significant role in the hyperpolarization process.

4.3.7 EPR Modulation

For CW EPR experiments, a modulation coil is needed. Due to the very confined space in the electromagnet setup, it is very flatly wound on a holder made of Kel-F®. The coil consists of 100 turns on a 15 mm diameter cylinder and is only 4 mm wide including the housing. It can therefore be clipped to the resonator housing and still be fit into the magnet.
An equivalent modulation coil is also used in the imaging setup, with a longer connection cable allowing the equipment to be kept out of the stray field.

4.3.8 Flow-through Setup

Sample flow is achieved using a standard medical injection pump (Graseby 3400, Smiths Medical) placed well outside the fringe field of the magnet. The sample is pumped through a 1.5 mm ID PTFE tube into the magnet to the polarizer, where it connects to the sample capillary (0.3 or 0.4 mm ID) via a Luer-Lok® connector in a plunger pressing on a conical Teflon® squeeze joint. The plunger presses the soft Teflon® squeeze joint against the Kel-F® housing. Due to the conical geometry of the housing, the tip of the

joint is squeezed against the capillary, which effectively tightens the connection. After the sample has passed through the polarizer cavity in the sample capillary, the capillary diameter can be necked down to accelerate the sample for faster transport to the detection site. Typically, the outlet capillary has an inner diameter of 0.15 mm (TSP150375, Polymicro Technologies). The necking is achieved by inserting the 0.15 mm ID/0.33 mm OD outlet capillary into the 0.4 mm ID sample capillary and gluing it in place with low-viscosity super-glue. Due to its low viscosity, this glue is quickly drawn into the space between the inner and outer capillary and therefore effectively seals the necking upon hardening. The flow-rates used in the experiments range up to 30 $\frac{\mathrm{ml}}{\mathrm{h}}$. While higher flow rates are in principle possible with this pump, the maximum flow is limited in this setup by the pressure necessary to achieve a high flow through relatively small capillaries. Being designed for infusions, the medical pump reports an occlusion above a certain pressure threshold, and stops. However, the flow rate is not a limiting factor in this setup. Due to the syringe design the accuracy of the pump is good, independent of the pressure it has to supply to reach the set flow rate. The flow rate error was determined to be ≤ 3 %.
After passing the detection site, the "spent" sample solution is collected in a basin for reuse. In order not to disturb the DNP experiment, particularly the NMR or MRI detection, this basin is kept out of the probe head (in the electromagnet setup) or in a safe distance from the pickup coil (in the imaging setup).

4.3.9 RF Compatibility

In any NMR or MRI experiment, one is very sensitive to unwanted noise in the respective RF region. Therefore, RF noise from the outside has to be shielded off. In spectroscopic NMR applications using a solenoid coil, the an RF shield completely surrounds the probe head. Clinical MRI scanners on the other hand are constructed in an open fashion to provide good access for the patient. Consequently, they are placed into large Faraday cages incorporated into the building structure, keeping out the RF noise.
In the electromagnet setup, the NMR resonant circuit is shielded off from its surroundings (see figure 4.11). However, in the setup with the MRI scanner, the Faraday cage RF shield will contain both the scanner *and* the DNP equipment. Therefore the RF compatibility of this equipment, especially the microwave source and its power supplies, is a major issue.
Supplying power for the microwave source via a switching-mode power supply ("SMPS") proved to be disastrous to the noise level. SMPSs rely on

pulsing, thereby creating RF noise at and above their operating frequency, which is then picked up by the detection coil of the MRI scanner. This is particularly so if the long waveguide is connected to the source, since it serves as an antenna for the RF noise as well, transporting it as a sheath current right to the detection coil. This problem was resolved by two measures:
Firstly, the SMPS was replaced by linear power supplies using a transformer. This eliminates the major source of RF noise in the setup. Secondly, the supply cables and the long waveguide were equipped with ferrite sheath current filters (7427114, Würth Elektronik) to prevent the transmission of noise to the detection coil. Additionally, the entire microwave source was equipped with a copper hood to further prevent the transmission of RF noise into the tomograph, as well as protect the microwave source from the strong RF pulses *from* the tomograph.

4.3.10 MRI Phantoms

For the first MRI experiments, two different phantoms were used:
Firstly, the 0.15 mm ID outlet capillary, which is comparable in size to a small blood vessel, was deployed. Essentially, this is a one dimensional phantom. Flowing an aqueous sample through it at moderate flow speeds, thus small Reynolds numbers, will result in a laminar "Hagen-Poiseuille" flow pattern over the capillary.
Secondly, a 0.4 mm thick flat cell was used, providing a two dimensional microfluidic system. The thickness of 0.4 mm was chosen as thin as possible while still allowing the outlet capillary to enter the flat cell. The flat cell is manufactured from two hard acrylic glass ("Plexiglas") blocks, the cell profile being milled in one block, the other block serving as a lid. Together with the outlet capillary, the two blocks are glued together with viscous polymer glue (ACRIFIX®, Evonik), which hardens upon ultraviolet ("UV") irradiation. This glue spreads very well along the interface between the two blocks without entering the flat cell cavity and thereby disturbing its shape. Upon hardening under a UV lamp the two blocks are basically fused into one, preventing any sample leakage to the sides. The flat cell is depicted in figure 4.14. The sample enters the flat cell through the outlet capillary, streams through the flat cell and then leaks out at the end where it can be collected in a basin. Both hard acrylic glass and the hardened glue contain protons and thus give an ^{1}H-NMR signal, but with a very fast decay, so it does not play a role in MRI acquisition.

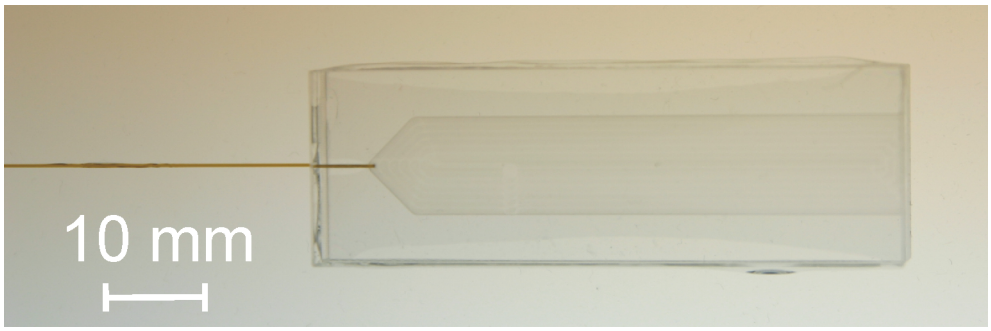

Figure 4.14: The 0.4 mm thick flat cell that was being used for the MRI experiments. Its outlet side on the right is open to allow the removal of bubbles etc.. The spread of the glue between the two acrylic glass blocks can be seen around the edges.

4.4 Experimental Procedures

Concordantly to the experiments performed at 9.2 T, the DNP enhancements were determined by taking the ^{1}H FT-NMR spectrum of the samples with and without CW microwave irradiation of the central hyperfine line of the ^{14}N-TEMPOL radicals, respectively, and integrating the proton NMR lines to determine the signal strength. Using equation 2.38, the enhancement ϵ can then be calculated. The optimal MW irradiation frequency was determined both by a CW EPR experiment (field swept in the electromagnet setup, frequency-swept in the imaging setup) and empirically.
Because this method takes the integral value of the NMR signal, it is insensitive to possible spacial inhomogeneities of the magnetization. In other words, this method yields an average or net enhancement for the entire sample volume, regardless of the actual magnetization distribution. For a DNP application this is a fair number, because what counts is the net enhancement of a certain sample volume. In other investigations, where the *maximum* enhancement in a spatial distribution is under investigation, other means of determining this number may be used, such as taking peak values.

In the imaging experiments, the repetition time ("TR") was varied in a range of 50 to 500 ms and excitation RF-pulse flip angle ("FA") from 45° to 90°, to find the optimal conditions for signal contrast and sensitivity and to observe the time-evolution of the flow pattern. The typical image resolution was 0.1 mm/pixel, with a pixel bandwidth of 80 Hz and a matrix size of 1024×512. The total measurement time ranged from 10 to 240 s per image, depending on the number of averages and the TR value used in the experi-

ment.
Because the sample is heated strongly in DNP experiments, small bubbles of air are found in the sample when it streams out of the resonator. They do not accumulate in capillaries, so they do not pose a problem in this case. They do however accumulate in the flat cell phantom, which makes is necessary to remove them from time to time. For this purpose, the flat cell is designed open on the outlet end, hence a capillary with a syringe attached can be inserted needle-like to remove the bubbles.

4.5 Results and Discussion

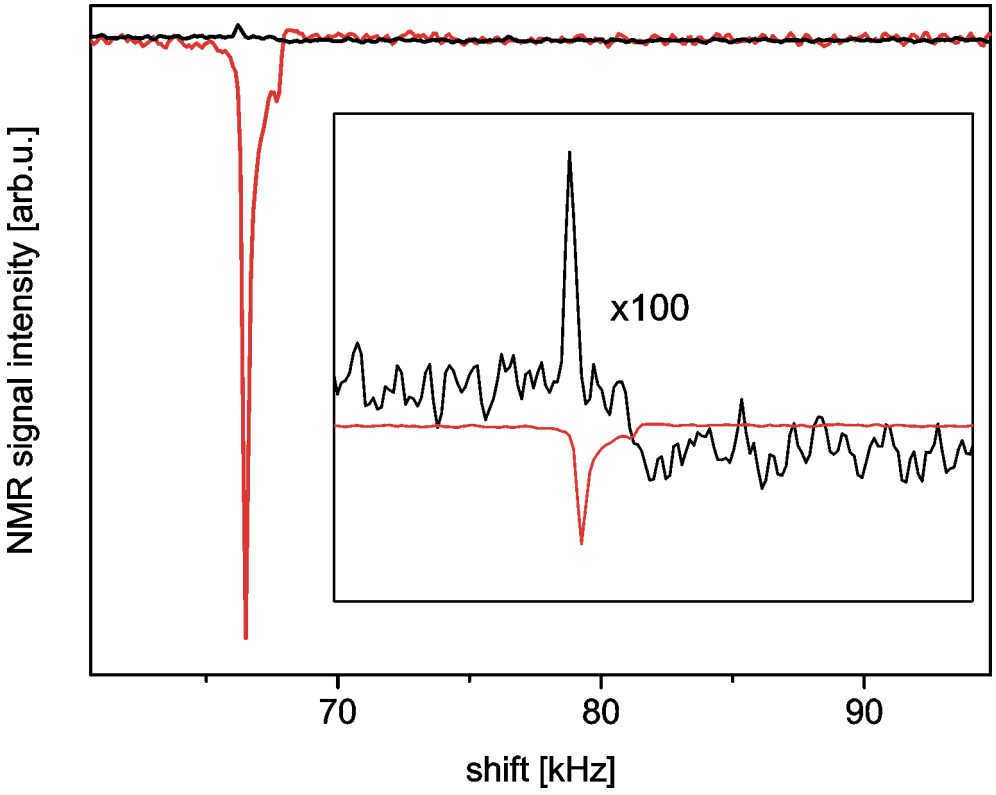

Figure 4.15: ^{1}H water proton NMR spectra of 24 mM TEMPOL in water with (red) and without (black) microwave irradiation of the sample, respectively. The spectra were taken inside the EPR cavity, with the sample resting, at a magnetic field strength of 1.5 T. An enhancement of -98 can be observed on the water proton signal (integrated over the whole signal). The inset shows the NMR signal without microwave $\times$100 for comparison.

Without flow of the sample, a DNP enhancement factor of -98 was achieved on water protons in an aqueous solution of 24 mM TEMPOL radical. The full available power of 2 W was applied to resonator R3 with a 0.3 mm ID sample capillary. The resulting Overhauser enhancement ϵ is depicted in figure 4.15. Due to the low NMR sensitivity the signal at thermal polarization (black line) is very weak, while the signal from the hyperpolarized sample (red line) is greatly enhanced and easily visible. The temperature shift between the hyper- and thermally polarized peaks can also be observed, resulting from heating of the sample close to the boiling point by the residual electrical field components of the microwave at the sample position.

This proves experimentally, that Overhauser enhancements by two orders of magnitude are feasible at 1.5 T magnetic field strength.
However, for the aspired application in a flow through setup and a detection behind the polarizer, the polarization must be performed under flow conditions. This means that in contrast to a resting sample a flowing sample has a finite time to polarize, because it only remains in the polarizer cavity for a certain amount of time. In consequence, under flow conditions, the achievable DNP enhancement is a function of flow, polarization build up and decay rates. Moreover, if a sample travels through a sample capillary at moderate flow speeds, thus small Reynolds numbers, a laminar Hagen-Poiseuille flow pattern over the sample capillary results, leading to an *inhomogeneous* residence time of microwave exposure. The central, fast part of the flow remains in the cavity for a much shorter timespan than slower flow layers, while the parts of the sample right next to the capillary wall are quasi-static. Therefore, for an efficient flow rate, some parts of the sample remain inside the EPR cavity for a time shorter than the polarization buildup time, which is in the order of the nuclear relaxation time T_{1n}. Thus, the enhancement inside the cavity under flow conditions is reduced. This enhancement drop could be modeled for various flow rates, which is described in appendix A.3.
Additionally, after flowing out of the cavity, the hyperpolarized nuclear spins will relax back to their thermal equilibrium value while being further dispersed according to the flow pattern along their travel pathway. Hence, one can only transport a part of the full hyperpolarization achieved inside the cavity to the detection site behind the polarizer. In fact, one has to balance fast flow and short transport times to maximize output and minimize relaxation losses on one hand and good polarization buildup on the other hand for an optimal transport of polarization. Because both the flow speeds and the polarization buildup and relaxation times play a role, the specific result depends on the flow geometry and the radical concentration. A higher radical concentration leads to a shortened T_{1n}. This yields a faster buildup time,

but simultaneously a faster relaxation. To compensate for a faster relaxation, the capillary can be necked to a smaller diameter, e.g. from 0.4 to 0.2 mm ID, right after the cavity. That way, the sample is polarized at slower flow speeds than it is transported to the detection site.
An example of polarization transport is shown in figure 4.16. While at zero flow no hyperpolarization can be transported out of the cavity, inducing a flow carries hyperpolarized sample to the detection site. Transport efficiency peaks at a certain flow value and then deteriorates slowly, due to the impeded polarization buildup at high flow speeds.

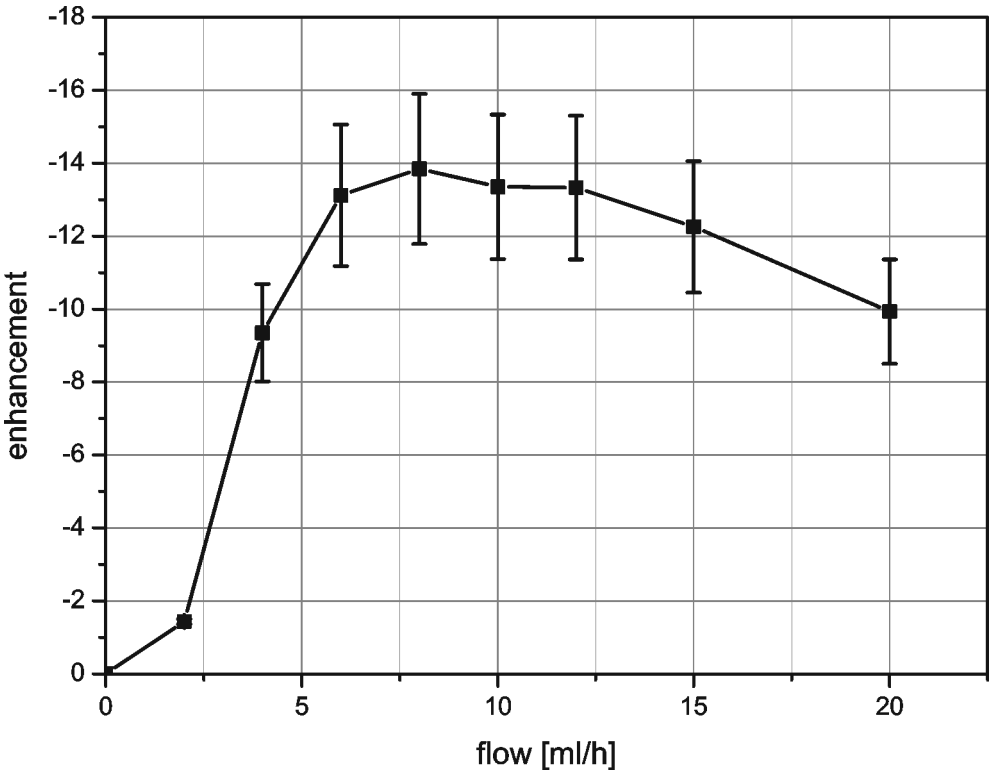

Figure 4.16: DNP enhancement vs. flow for a 24 mM TEMPOL in water sample, measured 30 mm behind the EPR cavity. At zero flow, the hyperpolarized sample remains in the EPR cavity and no transport of polarization takes place, while at very high flow speeds polarization buildup is impeded. Above a certain threshold, transport efficiency is relatively indifferent.

This shows that this setup is capable of hyperpolarizing the sample in flow through mode and to transport the hyperpolarized sample out of the polarizer to the detection site. While some of the hyperpolarization is lost

to relaxation and impeded buildup in flow through mode, the enhancements that can be achieved at the detection site are still significant.

This remains valid when performing the DNP experiment in the MRI scanner instead of the electromagnet setup. The ability to produce a constant flow of hyperpolarized sample is then demonstrated when performing imaging on the outlet capillary, out first, one-dimensional MRI phantom. Figure 4.17 shows the image of the outlet capillary, which is only 0.15 mm ID wide.

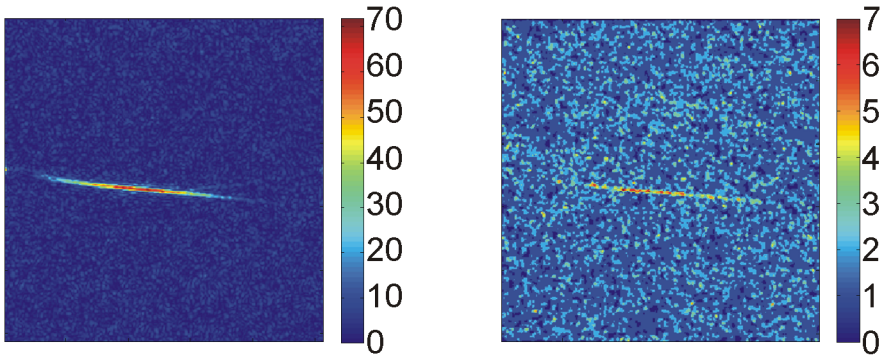

Figure 4.17: left: Single shot spin echo image of the outlet capillary, 0.15 mm ID, approximately 80 mm behind the resonator with DNP, i.e. while applying MW power to the polarizer. right: 8 scan average spin echo image of the same region as on the left, without DNP. Note the different intensity scales in the two figures. The sample used is a 24 mM ^{14}N-TEMPOL in water solution. The field of view ("FOV") is 45 mm; echo time ("TE") 16 ms, the repetition time ("TR") 200 ms and the flip angle 70°. The intensity profiles are due to the sensitivity profile of the imaging coil being limited to approximately its radius of about 20 mm in each direction.

As a result of this small sample volume, the capillary is hard to detect and a high spatial resolution of 0.1 mm/pixel is required. On the right side, the image without performing DNP is displayed. 8 averaging scans are necessary to acquire a sufficient SNR, yet it is very weak. This drastically changes with DNP: Running the resonator by irradiating the central EPR transition of the TEMPOL radical boost the signal from the capillary and it is easily visible with a single scan (left side). The gain in signal with the DNP polarized sample is above 10. Due to the small sample region, the signal strength and hence the enhancement is difficult to determine. The stated 10 is a rather

conservative estimate. In both images, the spatial sensitivity distribution of the imaging coil is apparent, as the signal disappears on a length scale of the coil radius of about 20 mm.

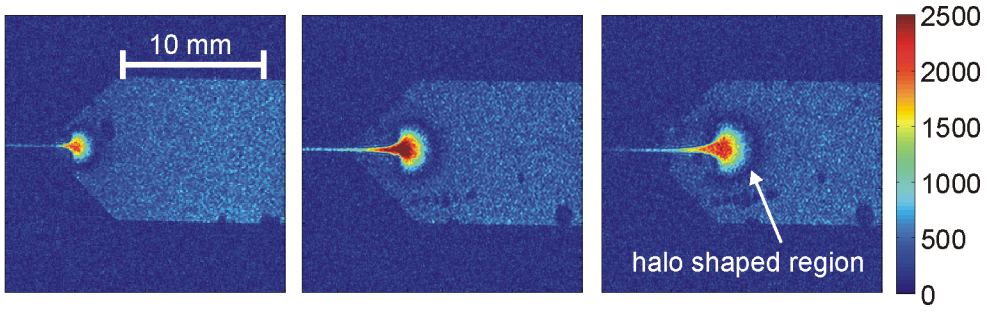

Figure 4.18: Single shot gradient echo images at various sample flow speeds: 12ml/h (left), 20ml/h (middle) and 30ml/h (right). The images show the outlet capillary leading into a 0.4 mm thick flat cell, approximately 60 mm behind the resonator while applying microwave power to the polarizer. The sample is 24 mM TEMPOL in water solution. Since the flat cell feature the same thickness everywhere, no physical volume effects can occur. One can clearly observe the jet of hyperpolarized, thus hyperintense sample into the sample which is at thermal polarization. During travel through the flat cell, the hyperpolarized sample relaxes back to thermal equilibrium, creating a halo shaped region without signal between the region with the enhanced, inverted signal, and the region at thermal polarization. While increased flow leads to a bigger jet, the image taken at 20 $\frac{\text{ml}}{\text{h}}$ shows the highest peak intensity, i.e. the highest enhancement. The small dark spots in the flat cell are small bubbles of air. The flat cell is 10 mm wide, the inlet is in the 90° corner on the left. The repetition time ("TR") is 100 ms, the echo time ("TE") is 10 ms, the flip angle is $90 \pm 5°$.

The constant stream of hyperpolarized sample is now used in the second phantom, the flat cell (shown in figure 4.14). The hyperpolarized sample is flown into the two dimensional flat cell filled with non-polarized sample, to demonstrate its dispersion and relaxation profile. Because the flat cell provides an equal thickness over its entire cell area, there are no partial volume effect, i.e. any pixel in the cell contains the same amount of sample and therefore its intensity truly reflects the net magnetization inside the voxel. Consequently, the intensity profile of an image is a polarization profile of the sample within; hyperpolarized sample appears hyperintense compared to non-polarized sample at thermal equilibrium. This can be seen in figure 4.18

for three different flow rates: 12 $\frac{\text{ml}}{\text{h}}$ (left), 20 $\frac{\text{ml}}{\text{h}}$ (middle) and 30 $\frac{\text{ml}}{\text{h}}$ (right).

The jet of hyperpolarized, thus hyperintense sample enters the cell in the 90° corner on the left side. The hyperpolarized sample relaxes while traveling through the flat cell, creating a steady state intensity distribution over the flat cell under constant flow conditions. It streams in with a highly enhanced, inverted signal, relaxes more and more towards thermal polarization while traveling on. Because of the negative enhancement the NMR signal passes through zero in the relaxation process, creating a region without *any* NMR signal. In the flat cell images it can be seen as a dark, halo-like region around the hyperintense jet before the sample reaches thermal polarization in the region covering the rest of the flat cell.
Comparing the three images taken at different flow rates shows that an increased flow leads to a bigger jet, i.e. the hyperpolarized sample travels farther before relaxing back to thermal polarization. The middle picture taken at 20 ml/h flow rate shows the highest signal intensity, thus the maximal enhancement, reflecting the geometry-dependent optimal flow rate for polarization transport, as depicted in figure 4.16 and described above. At lower flow rates relaxation kills the signal during transport, at higher flow rates the high flow speeds inhibit the DNP polarization process in the resonator cavity.
A closer look shows that the intensity of the jet of hyperpolarized sample right after entering the flat cell is not as high as it is a bit farther in the central part of the jet, when is has diffused more and slowed down. Despite the sample being "fresher" and hence higher polarized, it appears less intense. This is due to the relatively high velocity of the hyperpolarized sample with which it travels through the gradient fields. For instance, in the 0.15 mm ID outlet capillary the average flow speed for a flow rate of 30 $\frac{\text{ml}}{\text{h}}$ is 470 $\frac{\text{mm}}{\text{s}}$. Sample traveling fast through the field gradients leads to dephasing and therefore a weaker signal.[102] This effect is even stronger, when using imaging sequences that are more sensitive to this type of dephasing, like the Spin Echo sequence: One can actively suppress the signal of the fast-moving sample while maintaining the signal from the slower parts. This can be observed in figure 4.19.

While the region where the sample is traveling relatively slow is largely congruent to figure 4.18, the sample traveling fast shows - although hyperpolarized - no signal, thus appears completely dark.

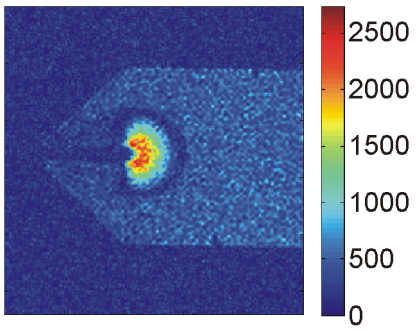

Figure 4.19: Single shot SE image of the same flat cell setup as in figure 4.18 at 30 $\frac{\text{ml}}{\text{h}}$ flow rate. One notices that the parts of the sample where it is traveling very fast are completely suppressed, due to their dephasing, while the slow moving parts appear hyperintense. No flow compensated gradients were used, making the dephasing particularly strong.

4.6 Conclusion and Outlook

These results demonstrate the ability to create a continuous flow of a hyperpolarized liquid sample by Overhauser DNP directly in the bore of a 1.5 T imaging magnet and to use it for MRI.

Compared to other liquid state DNP approaches, where the polarization is performed outside of the bore of the imaging magnet at X-band, the advantages are at hand: Since the distance between polarizer and imaging object is short, relaxation losses are minimal and losses from shuttling through field gradients are nonexistent. Additionally, performing the DNP experiment at X-band has the disadvantage of starting with a lower thermal equilibrium polarization to begin with. This "Boltzmann penalty", which for an X-band polarizer to 1.5 T imaging magnet sums up to a factor of approximately 5, is avoided in our approach altogether. In spite of the increased field weakening the DNP effect, an enhancement of -98 for proton spins could be achieved, compared to -170 at X-band (for ^{15}N-TEMPONE-D[38]). Therefore, the overall polarization achieved is larger in our approach, at the cost of more sophisticated microwave equipment and smaller sample volumes. Also, our setup lacks the flexibility of an external system, which can more easily be adapted to an imaging magnet of another field strength, e.g. 2 T.[103]

A limiting factor of the current setup is the amount of hyperpolarized sample which can be produced in a given amount of time: Depending on the desired flow speed, sample production is in the range of 3 to 8 $\frac{\mu\text{l}}{\text{s}}$, falling short of 8 to 25 $\frac{\mu\text{l}}{\text{s}}$ which have been achieved at X-band.[88] Therefore, a manifest improvement step is to enlarge the polarizer cavity. This could be achieved by using a higher mode cavity, i.e. making the polarizer cavity

longer. Sample flow speed could be greatly increased while maintaining residence time, hence a higher flow rate could be achieved without sacrificing DNP performance. Another option is the "brute force" approach of using parallel microwave resonators and combining their output. Admittedly, both these approaches would require larger microwave power.
Also, the fast nuclear spin relaxation time, induced by the radicals in the solution, prove to be a bottleneck: While using higher concentrations is beneficial for the DNP effect and the buildup time, they are detrimental for the transport of the hyperpolarization, since they enhance relaxation losses during flow.

A method to circumvent this is to *immobilize* the radicals, making them available for the DNP process in the cavity while keeping them out of the sample. This approach has been introduced for flow-through DNP applications as "SLIT" (solid-liquid intermolecular transfer) using nitroxides bound to silica gel or polymer beads and studied extensively for various target solvents.[104–108] More closely related it has been applied for an imaging application similar to ours at X-band.[88] In the latter case nitroxide radicals were covalently bound to agarose gel, the target solvent being water. The water can percolate through this matrix, being exposed to the nitroxide radicals without solving them. As a result, the sample output is pure, hyperpolarized water, which makes the method particularly interesting for medical applications. The T_{1n} times in pure water range from ≈ 3 s at room temperature up to ≈ 10 s at ≈ 90 °C.[109] Also, this renders the issue of inhomogeneous residence time of microwave exposure in the resonator cavity for a Hagen-Poiseuille flow pattern moot, since the percolation through the gel is homogeneous, rendering rather a plug flow.
Alternatively to immobilizing the radicals one can attempt to extract the radicals after the hyperpolarization process.[110] For instance, ascorbic acid reduces TEMPOL radicals rather quickly.[111–114]
Since neither Overhauser DNP nor MRI is limited to proton spins, hyperpolarization of other nuclei, e.g. ^{13}C or ^{15}N, is an attractive option making relaxation times longer and applications more versatile. For instance, the in vivo T_{1n} value of the $^{13}C_1$ of pyruvate, lactate, and alanine shows that they are all within 15 ± 5 s in a rat and 20 ± 5 s in a pig, opening the possibility for metabolic imaging with these substances using hyperpolarization.[31]
Compared to protons, ^{13}C not only yields longer relaxation times but also the advantage of a negligible background signal, making it even more valuable as a hyperpolarized compound.
The hyperpolarization of these nuclei by Overhauser DNP can be envisioned to be direct, via a coupling to the electronic spins, or indirect, by hyperpo-

larizing protons on the target molecule first and then transferring the polarization e.g. in an INEPT-type experiment. In the latter case, the first step of hyperpolarizing protons would then be similar to the DNP experiments on metabolites at 9.2 T.[70]
The limitation of the hyperpolarization decaying with the respective T_{1n} can also be addressed by another method that allows the storage of nuclear spin polarization in liquids much longer than T_{1n}.[115–117] This method relies on the creating of nuclear spin singlet states by RF pulsing. These singlet states are immune to the dominant source of nuclear relaxation in liquid samples, the intramolecular dipole-dipole relaxation, because of their symmetry.[43] Subsequently, the singlet states have to be isolated by appropriate pulse sequences. Applying this method, decay time constants on the order of minutes, rather than seconds, can be achieved.

An extension of the in-bore system to a higher magnetic field, such as a 3 T MRI scanner, is in principle possible while bringing about several issues: On the technical side increasing the field and thus the resonance frequencies (e.g. 84 GHz EPR frequency in a 3 T field) results in shorter wavelengths and therefore smaller, more challenging structures and smaller sample volumes. On the physical side, increasing the field will generally decrease the DNP efficiency; an example being 3.4 T ("W-band"), where enhancements on water protons have been reported ranging from -43[38] to -125[37] and -165[36] at highly elevated temperatures.
Considering an application in microfluidics rather than medical imaging opens even more possibilities. In lieu of water, xenobiotic, organic solvents such as toluene, DMSO or acetone can be used in this application as well. Among those, particularly toluene has lower dielectric losses compared to water. As a result, heating is less of an issue and the sample size and hence the flow rate can be increased more easily.

Overall, our approach allows to substantially increase contrast and sensitivity for flow applications in medical oriented MRI or in microfluidic applications.

Chapter 5

Conclusion

In this thesis, the development of an in-bore liquid state DNP polarizer for MRI applications operating in flow through mode at a magnetic field strength of 1.5 T was described. After an introductory chapter 1 and a chapter 2 on the theoretical background, chapter 3 dealt chiefly with the challenge of performing liquid state DNP at a high magnetic field of 9.2 T. The feasibility of performing liquid state DNP at this field was demonstrated for various solvents, as well as for metabolites in solution. Chapter 4 then moved to the aim of this work, the application of liquid state DNP for MRI experiments. It introduced the rationale of our approach, the hardware that was developed and demonstrated its performance in a clinical MRI tomograph.

5.1 Liquid State DNP at High Fields

At a magnetic field strength of 9.2 T, liquid state DNP enhancements up to ≈ -80 were observed on water protons in aqueous solutions of TEMPOL radicals at elevated temperatures. The sample temperature during a DNP experiment was extracted via the chemical shift of a heating reference. The saturation factor was extracted using the paramagnetic shift of the NMR line in samples with high radical concentration. This allows an extraction of the coupling factor ξ.
Additionally, DNP experiments were performed on solutions of TEMPOL radicals in acetone, DMSO and toluene. The experiments showed that contrary to predictions from simple force-free models describing the Overhauser effect well at low magnetic fields, enhancements of ≈ -30, ≈ -20 and ≈ -15 could be achieved for acetone, DMSO and toluene, respectively. This might show, that local dynamics of the DNP radical-target molecule system play an important role for the DNP enhancement at high magnetic fields.

DNP experiments on the metabolites pyruvate, lactate and alanine in aqueous solution were performed for the first time. The experiments revealed a DNP enhancement on their respective methyl protons resulting from their direct dipolar coupling to the radicals, independently of the solvent proton polarization. Using this, the ratio of the respective high field coupling factors between water protons and the methyl protons of the metabolites were extracted. Again, the simple force-free model does not render these numbers. These experiments show that considerable enhancements can not only be expected on water protons, but on metabolites as target molecules as well.

5.2 In-bore DNP for MRI

Motivated by the considerable DNP enhancements achieved at 9.2 T, a 42 GHz polarizer designed to be operated in a clinical 1.5 T MRI magnet, was developed. The DNP polarizer consists of an appropriate 42 GHz microwave source with 2 W output power, a microwave transmission system, an EPR resonator and a pump system to flow the sample continuously through the EPR resonator.
With this system, a DNP enhancement of -98 was observed for water protons of a resting sample inside the EPR resonator using TEMPOL radicals. By operating the polarizer in flow-through mode, the hyperpolarization can be transported out of the polarizer. The polarizer system was incorporated into a commercial 1.5 T MRI tomograph, where its hyperpolarized sample output was used in imaging experiments. Two imaging phantoms, a capillary and a flat cell, were used. The hyperpolarized sample was shown to create a significant signal increase > 10 in images, while flow rates up to 30 $\frac{\mathrm{ml}}{\mathrm{h}}$ were achieved.
The two major limitations of the current setup are the flow rate, i.e. the amount of hyperpolarized sample that can be produced in a given amount of time, and the fast nuclear spin relaxation time, induced by the radicals in the solution.

5.3 Outlook

This work has shown that the approach of operating a liquid state DNP polarizer at 1.5 T is feasible. To be able to better employ it in microfluidic or medical applications, it should be optimized and its shortcomings have to be

tackled.
Because of the limitations in the flow rate a manifest improvement step is to enlarge the polarizer cavity. This would allow a larger sample volume and a higher flow rate. This can be realized by a higher mode cylindrical resonator or an entirely new resonator design.
A huge prospective improvement is the prolongation of the relaxation time of the hyperpolarization. Because the immobilization of the radicals in the polarizer cavity can boost the relaxation time by an order of magnitude and has been shown to work at lower fields, it is a very promising attempt. As well, much longer relaxation times can be achieved by the use of ^{13}C as target nuclei. Consequently, the Overhauser DNP enhancement on ^{13}C will be investigated. This is particularly interesting with metabolites as target molecules considering metabolic imaging applications.

Appendix A

Supplementary Material

A.1 NMRD data

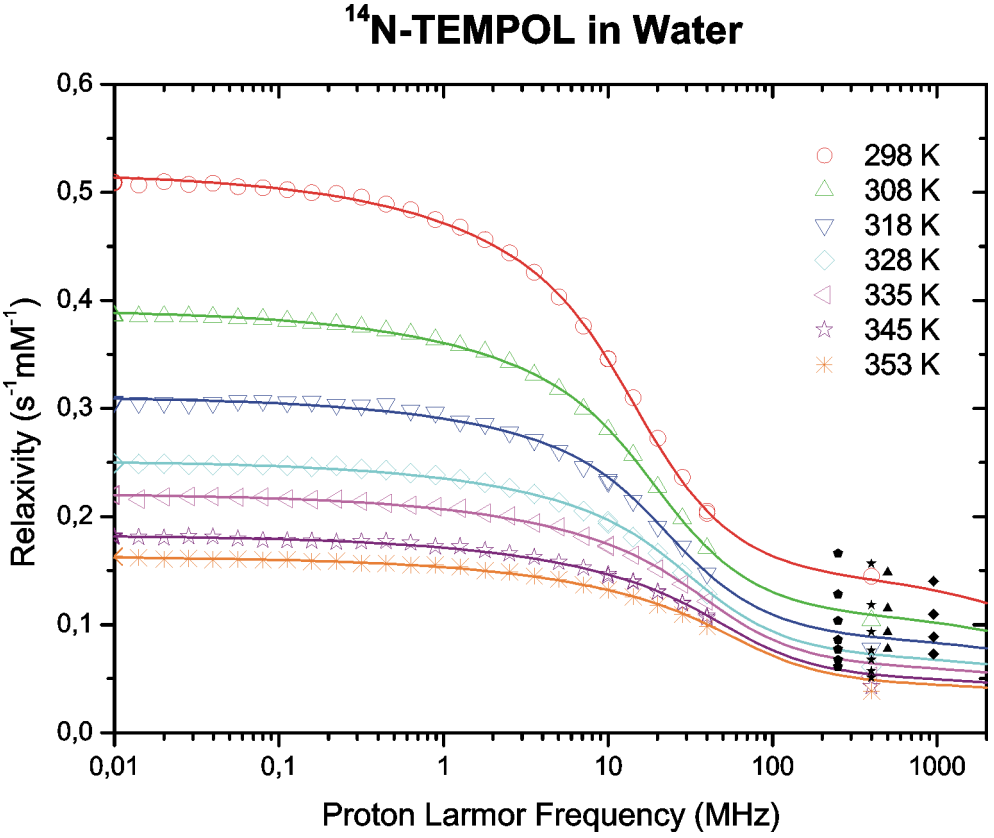

Figure A.1: Relaxivity measurements of a 100 mM ^{14}N-TEMPOL in water solution for magnetic fields up to 20 T.

The coupling factor was extracted from relaxivity measurements of the protons in a DNP sample over a wide field range up to 20 T.
NMRD data by courtesy of Giacomo Parigi (CERN, Florence, Italy).

A.2 Determination of the DNP Buildup Time

The determination of the DNP buildup time can in principle be determined in two ways:
The first option is to switch on the microwave source at the desired power and frequency, wait for a time τ and then acquire the NMR spectrum. This scheme is depicted in figure A.2.

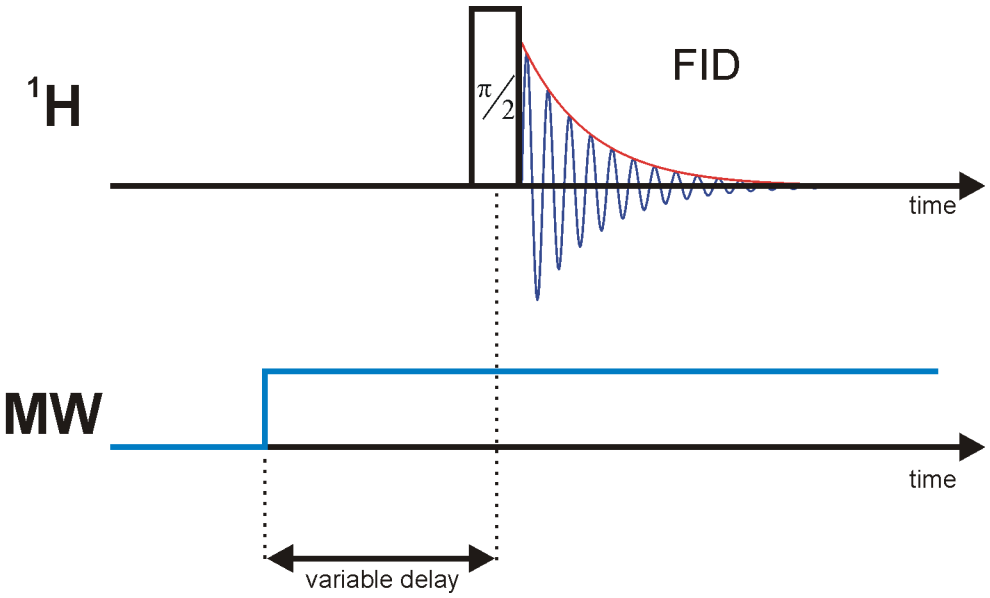

Figure A.2: Pulse scheme for measuring the DNP buildup time constant by switching on the source. This figure is not drawn to scale.

For $\tau = 0$, the spectrum is yet unperturbed by the DNP effect, so it corresponds to the spectrum without DNP. Varying τ will varies the time the system can evolve under DNP conditions, i.e. the time in which the polarization can build up before the detection. For $\tau \to \infty$, i.e. $\tau \gg T_{buildup}$, the spectrum corresponds to the spectrum under CW irradiation.
Subsequently, the NMR signal strength is determined by integrating the respective NMR peak, and the results are plotted versus the respective value

of τ, yielding a buildup diagram, which can then be fitted by an exponential. However, this method requires a microwave source that can be switched on a faster timescale than τ.
Additionally and more troublesome, switching on the microwave will not only induce the DNP process, but also the dielectric microwave heating of the sample. Consequently, varying τ also varies the temperature, making this a bad approach at $T_{buildup}$.

The second option does not require switching of the microwave source: More elegantly, the microwave is kept on in CW mode, pumping the EPR transition and driving the DNP effect. The NMR signal is now diminished by a suppression pulse scheme (e.g. a "picket fence" pattern). After waiting for a variable τ, the NMR spectrum is recorded, as depicted in figure A.3.

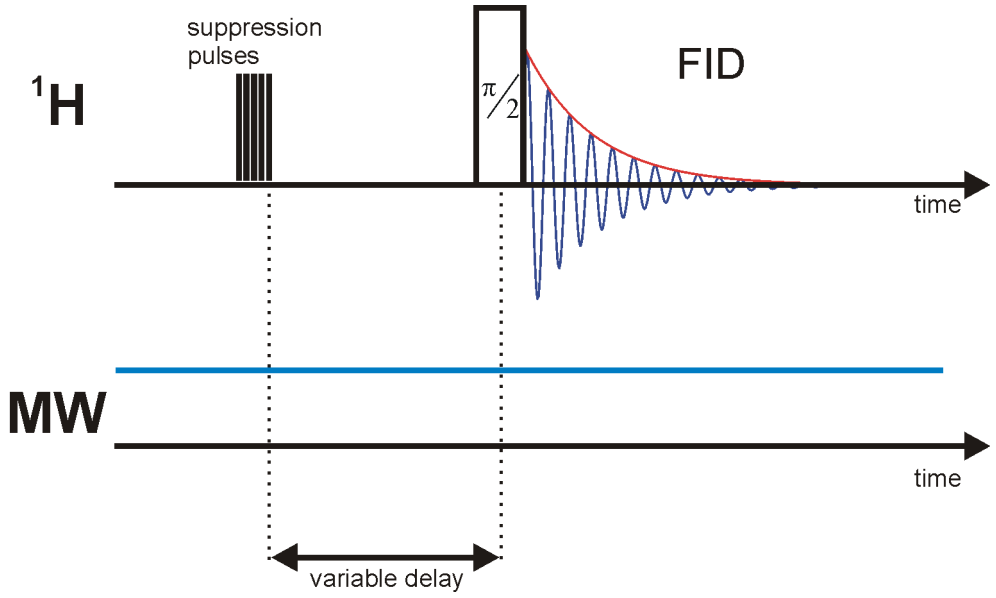

Figure A.3: Pulse scheme for measuring the DNP buildup time constant by suppressing the NMR peak. This figure is not drawn to scale.

Again, this gives a buildup curve, from which $T_{buildup}$ can be extracted by fitting it with an exponential. This is shown in figure A.4.

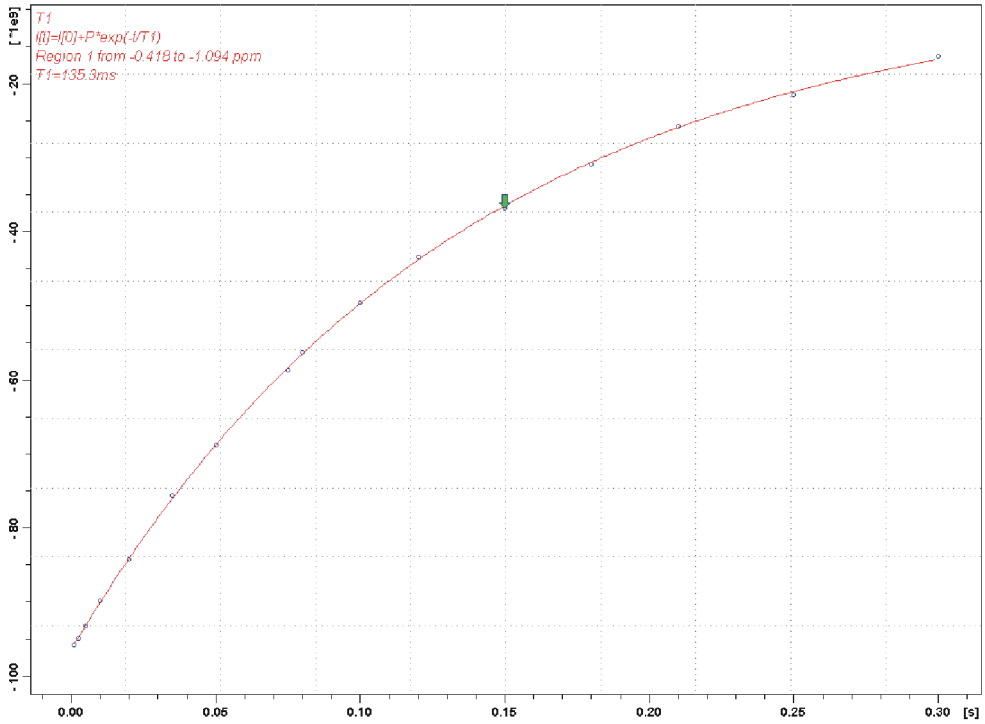

Figure A.4: Integrated NMR signal intensities of the water peak of a 100 mM ^{14}N-TEMPOL in water DNP sample versus the time delay τ. The buildup can be fitted with an exponential, with time constant $T_{buildup} \approx 135.3$ ms in this particular case.

Because this method does not switch the microwave source on and off it does not suffer from the same problems as the first method, hence capturing the DNP buildup under CW conditions.

A.3 Enhancement Drop Modeling under Flow

The enhancement drop inside of the resonator cavity under flow through conditions *inside* the resonator is modeled the following way:

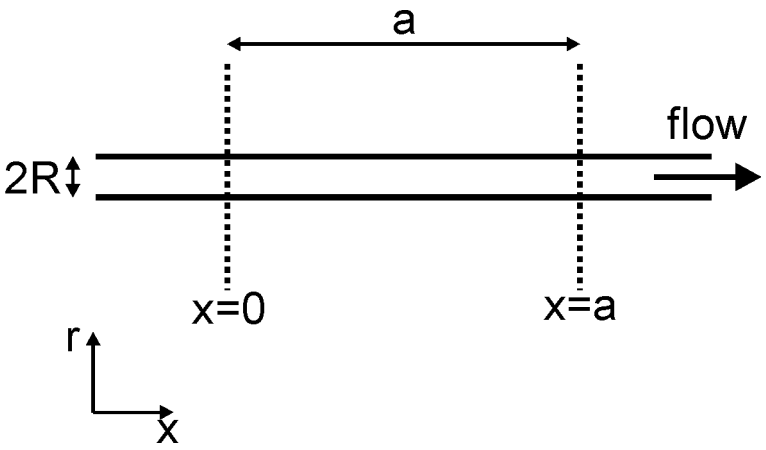

Figure A.5: Schematic model of the resonator - capillary system.

Due to the cylindrical symmetry of the setup, cylinder coordinates are convenient: x, r, φ.
Let the sample capillary be of diameter $2 \cdot R = 0.3$ mm, running through the resonator cavity in x-direction from its entry point at $x = 0$ to $x = a = 14$ mm, where it exits the cavity (figure A.5). The NMR signal detection volume is considered identical to the sample inside the resonator.
Suppose the sample flow is laminar inside the capillary and the flow direction is the positive x-direction. Assuming no-slip-conditions on the capillary walls renders the familiar Hagen-Poiseuille flow pattern with the flow speed:

$$\mathbf{v}(r) = v \cdot \mathbf{e}_x \quad , \tag{A.1}$$

with

$$v(r) = \underbrace{\frac{\Delta p}{4\eta l}}_{=:\alpha} \left(R^2 - r^2\right) \quad . \tag{A.2}$$

Integration renders the average flow speed

$$\overline{v} = \frac{1}{2} \cdot \frac{\Delta p}{4\eta l} \cdot R^2 = \frac{1}{2} \cdot \alpha \cdot R^2 \quad . \tag{A.3}$$

Now $v(r)$ can be conveniently written:

$$\begin{aligned} v(r) &= 2 \cdot \overline{v} \left(1 - \frac{r^2}{R^2}\right) \\ &= 2 \cdot \frac{\dot{V}}{\pi R^2} \left(1 - \frac{r^2}{R^2}\right) \quad , \end{aligned} \tag{A.4}$$

by using the flow rate $\dot{V} = \pi R^2 \overline{v}$, which is available as an experimental value.

In such a Hagen-Poiseuille flow, a nucleus at the site (x, r, φ), $x \in [0; a]$ has been in the resonator for the time

$$t(x, r, \varphi) = \frac{x}{v(r)} \quad . \tag{A.5}$$

Let's assume that any nucleus enters the cavity with the thermal equilibrium polarization P_{eq} and is then homogeneously hyperpolarized to the DNP polarization P_{MW}, i.e. independently of its position in the resonator. This assumption is equivalent to a *homogeneous* DNP effect, i.e. a homogeneous B_1 field in the resonator cavity and no temperature gradients causing gradients in the saturation, leakage or coupling factor. The hyperpolarization process shall have the characteristic time constant T_{bu}, the buildup time, so basically it is treated like a relaxation from P_{eq} to P_{MW}. The buildup time T_{bu} and the enhancement without flow $\epsilon = \frac{P_{MW}}{P_{eq}} - 1$ are our model parameters, while all other constants are given by the flow rate $\dot{V}$ and the geometry, i.e. R and a.
This approach renders for the polarization of a nucleus at the site (x, r, φ), $x \in [0; a]$:

$$\begin{aligned} P(x, r, \varphi) &= (P_{eq} - P_{MW}) e^{-\frac{t(x,r,\varphi)}{T_{bu}}} + P_{MW} \\ &= (P_{eq} - P_{MW}) e^{-\frac{x}{v(r) \cdot T_{bu}}} + P_{MW} \quad . \end{aligned} \tag{A.6}$$

Being proportional to the net polarization $\overline{P}$, the NMR signal strength can now be calculated by integrating over the entire sample in the cavity:

$$\overline{P} = \int_0^a dx \int_0^{2\pi} d\varphi \int_0^R r \cdot dr P(x, r, \varphi). \tag{A.7}$$

This model was implemented in Maple® (Waterloo Maple Inc.), to match the experimental results that were achieved in an equivalent setup: A 24 mM ^{14}N-TEMPOL in water sample in a 0.3 mm ID capillary and a resonator cavity $\approx$ 14 mm long. Using resonator R3 and the saddle coil setup, the DNP

enhancement was measured inside of the resonator for sample flow rates ranging from 0 to 15 $\frac{\text{ml}}{\text{h}}$. Approximately 1 W power was applied, to prevent boiling effects. For the modeing, the ratio $\frac{P_{MW}}{P_{eq}} = \epsilon + 1 \stackrel{!}{=} -38$ was chosen. Because $T_{1n} \approx 150$ ms for this sample, the modeling was performed for $T_{bu} \stackrel{!}{=} 100$, 150 and 200 ms The result is depicted in figure A.6. The experimental data points (blue) are matched well by the curves obtained for $T_{bu} \stackrel{!}{=} 100$ ms (green line), $T_{bu} \stackrel{!}{=} 150$ ms (black line) and $T_{bu} \stackrel{!}{=} 200$ ms (red line).

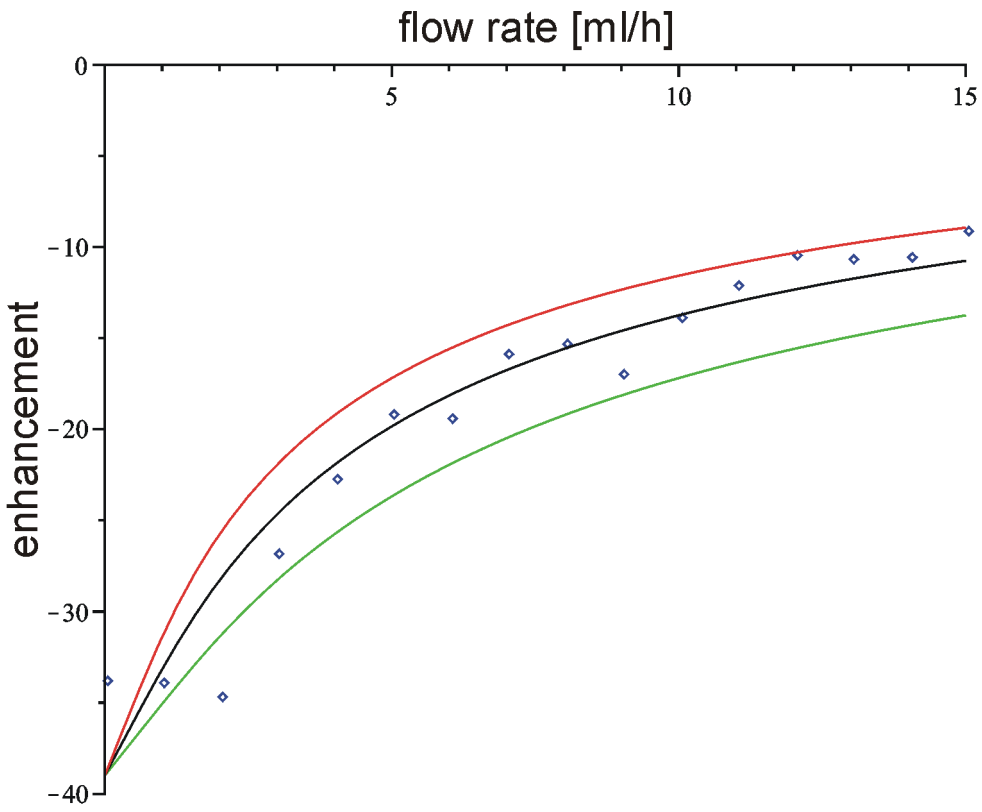

Figure A.6: DNP enhancement vs. flow rate for a 24 mM ^{14}N-TEMPOL in water sample in a 0.3 mm ID capillary. The experimental data points (blue) are matched well by by the curves obtained by the calculation for $T_{bu} \stackrel{!}{=} 100$ ms (green line), $T_{bu} \stackrel{!}{=} 150$ ms (black line) and $T_{bu} \stackrel{!}{=} 200$ ms (red line).

The MAPLE code for the calculation is as follows:

$restart;$
$with(plots);$
$R := .15;$
$P := -38;$
$a := 14;$
$v := (r, F) \to 2 * F * (R^2 - r^2)/(Pi * 3.6 * R^4);$
$p := (t, T) \to (1 - P) * exp(-t/T) + P;$
$t := (h, r, F) \to (1/2) * Pi * h * R^4/(F * (R^2 - r^2));$
$f := (h, r, F, T) \to p(t(h, r, F), T);$
$int(f(h, r, F, T) - 1, h = 0..a);$
$gt := (r, F, T) \to int(f(h, r, F, T) - 1, h = 0..a);$
$g := (T, F) \to evalf((int(2 * Pi * r * gt(r, F, T), r = 0..R))/(Pi * R^2 * a));$
$points := [[0, -33.6], [1, -33.8], [2, -34.5], [3, -26.7], [4, -22.6], [5, -19.0],$
$[6, -19.2], [7, -15.7], [8, -15.2], [9, -16.8], [10, -13.7], [11, -12.0], [12, -10.3],$
$[13, -10.5], [14, -10.4], [15, -9.0]];$
$plot1 := plot(points, style = POINT);$
$plot2 := plot(g(.1, F), F = 0.1e - 2..15);$
$plot3 := plot(g(.15, F), F = 0.1e - 2..15);$
$plot4 := plot(g(.2, F), F = 0.1e - 2..15);$
$display(plot1, plot2, plot3, plot4, view = [0..15, -40..0])$

Appendix B

Lists

B.1 List of Publications and Patents

- Mar 2012:
  Jan G. Krummenacker, Vasyl P. Denysenkov and Thomas F. Prisner.
  Liquid State DNP on Metabolites at 260 GHz EPR/400 MHz NMR Frequency.
  article under review

- Jan 2012:
  Jan G. Krummenacker, Vasyl P. Denysenkov, Maxim Terekhov, Laura M. Schreiber and Thomas F. Prisner.
  DNP in MRI: An in-bore approach at 1.5 T.
  Journal of Magnetic Resonance, 215: 94-99, 2012

- Jun 2011:
  partent application Application number: WO2011160853
  Hyperpolarization device and method for administering hyperpolarized liquid contrast agent
  Inventors: Jan Krummenacker, Thomas Prisner, Vasyl Denysenkov, Laura Maria Schreiber and Kerstin Münnemann

- Jun 2010:
  partent application Application number: DE201010017568
  Hyperpolarisationseinrichtung und Verfahren zur Verabreichung eines hyperpolarisierten flüssigen Kontrastmittels
  Inventors: Jan Krummenacker, Thomas Prisner, Vasyl Denysenkov, Laura Maria Schreiber and Kerstin Münnemann

B.2 List of Public Talks and Conference Contributions

- Feb 2012:
  talk: *"Dynamic Nuclear Polarization for Magnetic Resonance Imaging"*
  Max-Planck-Institut für Polymerforschung, Mainz, Germany

- Jan 2012:
  talk: *"Dynamic Nuclear Polarization for Magnetic Resonance Imaging"*
  Institut für theoretische und physikalische Chemie, Goethe Universität Frankfurt, Germany

- Sep. 2011:
  poster: *"Liquid State Dynamic Nuclear Polarization for MRI at 42 GHz EPR Frequency"*
  poster: *"400 MHz High Field Liquid State Dynamic Nuclear Polarization"*
  3rd international DNP Symposium, École Polytechnique Fédérale de Lausanne, Lausanne, Switzerland

- Aug. 2011:
  poster: *"Liquid State Dynamic Nuclear Polarization for MRI at 42 GHz EPR Frequency"*
  poster: *"400 MHz High Field Liquid State Dynamic Nuclear Polarization"*
  EUROMAR 2011, Goethe Universität Frankfurt, Germany

- May 2011:
  talk: *"Dynamic Nuclear Polarization for Magnetic Resonance Imaging"*
  BMRZ seminar, Bad Homburg, Germany

- Oct. 2010:
  poster: *"Dynamic Nuclear Polarization for Magnetic Resonance Imaging"*
  DNP workshop, Warwick, UK

- Jul. 2010:
  poster: *"Liquid State Dynamic Nuclear Polarization for MRI at 42 GHz EPR Frequency"*
  EUROMAR 2010, Florence, Italy

- Oct 2009:
  poster: *"Liquid State DNP on Metabolites at 260GHz EPR/ 400MHz NMR Frequency"*
  COST P15 Training School on DNP at high magnetic fields, theory and applications, Safed, Israel

- Sep. 2008:
  poster: *"The Application of the Overhauser Effect to High-Field NMR in Aqueous Solutions"*
  EU-project Bio-DNP final meeting, Florence, Italy

- Aug. 2008:
  poster: *"High-Field DNP at 260 GHz / 400 MHz Frequencies in Liquid State Water Samples"*
  EUROMAR 2008, St. Petersburg, Russia

- Apr 2008:
  talk: *"DNP at Room Temperature via the Overhauser Effect: Recent Results at 400 MHz/260 GHz"*
  BMRZ seminar, Frankfurt a. M., Germany

B.3 List of Abbreviations

CE	**C**ross **E**ffect
CW	**C**ontinuous **W**ave
DKP	**D**ynamische **K**ernspin **P**olarisation
DMSO	**Di**ethyl**s**ulf**o**xide
DNP	**D**ynamic **N**uclear **P**olarization
EDS	**E**lectron **D**ipolar **S**ystem
ELDOR	**El**ectron **Do**uble **R**esonance
EMPA	**E**lectron **M**icro **P**robe **A**nalysis
EPR	**E**lectron **P**aramagnetic **R**esonance
EZS	**E**lectron **Z**eeman **S**ystem
FA	**F**lip **A**ngle
FID	**F**ree **I**nduction **D**ecay
FOV	**F**ield **o**f **V**iew
FT	**F**ourier **T**ransform
FWHM	**F**ull **W**idth at **H**alf **M**aximum
HSE	**H**eisenberg **S**pin **E**xchange
ID	**I**nner **D**iameter
INEPT	**I**nsensitive **N**uclei **E**nhancement by **P**olarisation **T**ransfer
MAS	**M**agic **A**angle **S**pinning
MD	**M**olecular **D**ynamics
MEOP	**M**etastability **E**xchange **O**ptical **P**umping
MRI	**M**agnetic **R**esonance **I**maging
MW	**M**icro**w**ave
NMR	**N**uclear **M**agnetic **R**esonance
NMRD	**N**uclear **M**agnetic **R**elaxation **D**ispersion
NZS	**N**uclear **Z**eeman **S**ystem
OD	**O**uter **D**iameter
PHIP	**P**ara-**H**ydrogen **I**nduced **P**olarization
Photo-CIDNP	**Photoc**hemically **I**nduced **D**ynamic **N**uclear **P**olarization
PTFE	**P**oly**t**etra**f**luoro**e**thylene
RF	**R**adio **F**requency
SE	**S**olid **E**ffect (DNP mechanism) **S**pin **E**cho (MRI sequence)
SEM	**S**canning **E**lectron **M**icroscopy
SEOP	**S**pin **E**xchange with **O**ptically **P**umped alkali metal vapor
SGRE	**S**poiled **G**radient **R**ecalled **E**cho
SLIT	**S**olid **L**iquid **I**ntermolecular **T**ransfer
SMPS	**S**witching **M**ode **P**ower **S**upply
SNR	**S**ignal-to-**N**oise-**R**atio

TEMPOL	4-hydroxy-2,2,6,6-**te**tra**m**ethyl-**p**iperidine-1-**o**xy**l**
TE	**E**cho **T**ime (MRI parameter)
	Transverse **E**lectric (mode)
TM	**T**hermal **M**ixing (DNP mechanism)
	Transverse **M**agnetic (mode)
TR	**R**epetition **T**ime
UV	**U**ltra**v**iolet
YIG	**Y**ttrium **I**ron **G**arnet

Appendix C

Deutsche Zusammenfassung

Kernspinresonanzverfahren, wie die NMR-Spektroskopie (von engl. ***n**uclear **m**agnetic **r**esonance*), spielen aufgrund ihrer Leistungsfähigkeit und Vielseitigkeit eine wichtige Rolle auf dem Gebiet der Physik, Chemie, Biologie und Medizin. Die Magnetresonanztomographie (MRT), die ebenfalls auf der Kernspinresonanz basiert, nimmt als nichtinvasives und enorm flexibles bildgebendes Verfahren vor allem in der Medizin eine herausragende Stellung ein.
Eine der größten Schwächen dieser Verfahren ist ihr inhärenter Mangel an Empfindlichkeit. So basieren alle diese Verfahren auf der Boltzmann-Besetzung von Spinzuständen, die durch die Zeemanwechselwirkung mit einem externen Magnetfeld energetisch aufgespalten sind. Da die daraus resultierende Energiedifferenz und damit die Besetzungsunterschiede sehr klein sind, wird insbesondere bei Raumtemperatur nur eine sehr kleine thermische Polarisation erreicht. Infolge dessen werden zur Kernspinresonanz immer stärkere Magnetfelder eingesetzt, was mit enormem technischem Aufwand verbunden ist. Trotzdem beträgt die thermische Polarisation von Protonenspins, die das größte magnetische Moment aller Kerne besitzen, im z. Zt. stärksten verfügbaren NMR-Magneten ($\approx$ 24 T) bei Raumtemperatur lediglich $\approx 8 \cdot 10^{-5}$. Folglich ist hier theoretisch eine Verbesserung der Polarisation und damit der Empfindlichkeit um vier Größenordnungen möglich.
Diese konzeptionelle Schwäche kann durch die Verwendung hyperpolarisierter Substanzen abgemildert werden, d.h. durch Erreichen einer Spinpolarisation, die größer ist, als die thermische. Ein solcher hyperpolarisierter Stoff gibt ein verstärktes MRT-Signal, ist also markiert, ohne weiter physikalisch oder chemisch verändert worden zu sein.

Eine mögliche Hyperpolarisationsmethode für Kernspins ist die **D**ynamische **K**ernspin**p**olarisation ("DKP", auch "DNP" für engl. ***D**ynamic **N**uclear*

***P**olarization*). Bei der DKP wird die Hyperpolarisation dadurch erreicht, dass die Übergänge ungepaarter Elektronenspins in stabilen Radikalen durch resonante Mikrowelleneinstrahlung angeregt werden. Folglich wird die Polarisation der Elektronenspins, die mehrere Größenordnungen über der der Kerne liegt, gestört. Da die Kernspins mit denen der Elektronen wechselwirken, wird auch deren Polarisation beeinflusst und die hohe Polarisation der Elektronenspins auf die Kernspins übertragen.
Der Verstärkungsfaktor, der mit DKP maximal erreicht werden kann, beträgt 660 für Protonenspins, während er für ^{13}C sogar 2600 betragen kann.

Diese Arbeit beschäftigt sich mit der Entwicklung eines DKP-Polarisators, der eine flüssige Probe im kontinuierlichen Fluss hyperpolarisiert, um sie anschließend zur MRT einzusetzen. Zur Vermeidung langer Transportwege geschieht dies direkt im Magnetfeld eines gewöhnlichen MRT Tomographen mit einer Feldstärke von 1.5 T, was eine Einstrahlungsfrequenz der Mikrowellen von 42 GHz ergibt.

C.1 DKP in Flüssigkeiten bei hohen Feldern

Da der DKP-Mechanismus, der in Flüssigkeiten vorliegt, mit steigender Feldstärke an Effizienz verliert, wurde zunächst gezeigt, dass die DKP auch bei hohen Feldern wirkungsvoll ist.
Bei einer Feldstärke von 9.2 T wurden Verstärkungsfaktoren von bis zu ≈ -80 für Protonen von Wassermolekülen in wässrigen Lösungen des stabilen Radikals TEMPOL bei erhöhter Temperatur erreicht. Es wurde ein Verfahren aufgezeigt, um die Probentemperatur im DKP Experiment über die chemische Verschiebung der NMR Resonanzlinie einer entsprechenden Eichprobe zu bestimmen. Außerdem wurde ein Verfahren entwickelt um den Sättigungsfaktor aus der paramagnetischen Verschiebung der NMR Linie bei hohen Radikalkonzentrationen abzuleiten. Dies erlaubt die Errechnung des Kopplungsfaktors, der experimentell bei diesen Feldern schwer zugänglich ist.
Außerdem wurde die Wirksamkeit der DKP bei Lösungen von TEMPOL in den organischen Lösungsmitteln Aceton, DMSO und Toluol nachgewiesen. Entgegen der Vorhersage einfacher Modelle, welche die DKP bei kleinen Feldern gut beschreiben, wurden Verstärkungsfaktoren von ≈ -30, ≈ -20 und ≈ -15 für Aceton, DMSO und Toluol erreicht.
Des Weiteren wurden erstmalig DKP-Experimente an wässrigen Lösungen der Metaboliten Pyruvat, Laktat und Alanin durchgeführt. Hierbei konnte gezeigt werden, dass die Methylprotonen der jeweiligen Metaboliten einen

Verstärkungsfaktor zeigen, der auf ihre direkte Kopplung an die Elektronenspins zurückzuführen ist und unabhängig von der Polarisation der Protonen der Wassermoleküle ist. Diese Experimente zeigen, dass eine Verstärkung der Kernpolarisation nicht nur für Wassermoleküle, sondern auch für größere Hyperpolarisationsziele zu erwarten ist. Dies ist insbesondere mit Hinblick auf die metabolische Bildgebung von Interesse, bei der Metaboliten durch Hyperpolarisation markiert werden.

C.2 DKP in der MRT

Motiviert durch die beträchtlichen Verstärkungsfaktoren, die bei 9.2 T erreicht werden konnten, wurde ein DKP-Polarisator für Flüssigkeiten entworfen, der in einem klinischen MRT Magneten bei 42 GHz arbeitet. Der Polarisator besteht aus einer entsprechenden 42 GHz Mikrowellenquelle, einem System zur Übertragung der Mikrowellenleistung, einem Elektronenspinresonanz-Resonator und einem Durchflusssystem, um die flüssige Probe durch den Resonator zu pumpen.
Mit diesem System konnte ein Verstärkungsfaktor von -98 für die Protonen von Wassermolekülen in einer unbewegten Probe erreicht werden. Über eine Pumpe konnte die Probe und damit die Hyperpolarisation aus dem Polarisator transportiert werden. In einem zweiten Schritt wurde nun der Polarisator in einen gewöhnlichen 1.5 T MRT Tomographen verbaut, um dann die hyperpolarisierte Probe für MRT Experimente zu nutzen. An zwei unterschiedlichen Phantomen, einer Kapillare und einer Flachzelle, wurden Verstärkungen in MRT Bildsignalen > 10 erzeugt, wobei Flussraten bis zu $30\ \frac{\mathrm{ml}}{\mathrm{h}}$ erreicht wurden.
Die beiden größten Schwachpunkte des derzeitigen Systems sind die Flussrate, die für die klinische Bildgebung noch unzureichend ist und die schnelle Relaxationszeit der Hyperpolarisation, die durch die gelösten Radikale in der Probe hervorgerufen wird.

C.3 Ausblick

In dieser Arbeit wurde gezeigt, dass der Ansatz einen DKP-Polarisator für Flüssigkeiten in einem Tomographen bei 1.5 T zu betreiben, praktikabel ist. Der in dieser Arbeit entwickelte Polarisator liefert einen kontinuierlichen Strom hyperpolarisierter Probenflüssigkeit. Um das System für eine klinische

Anwendung oder Mikrofluiditätsuntersuchungen besser einsetzen zu können, müssen jedoch seine Schwachpunkte bewältigt werden.
Eine naheliegende Lösung zur Verbesserung der Durchflussrate ist mit einer Vergrößerung des Resonators gegeben. So würde diese Maßnahme das Probenvolumen vergrößern und damit den möglichen Durchfluss erhöhen. Realisiert werden kann dies beispielsweise durch Verwendung einer höheren Mode eines Zylinderresonators oder durch einen gänzlich neuen Resonatorenentwurf.
Ein riesiges Verbesserungspotential birgt die Verlängerung der Relaxationszeit der Hyperpolarisation. Durch eine Immobilisierung der Radikale im Resonator kann diese Relaxationszeit um eine Größenordnung verlängert werden. Für kleinere Felder konnte bereits gezeigt werden, dass dies für die DKP funktioniert, so dass dieser Ansatz sehr vielversprechend ist. Eine weitere Möglichkeit liegt in der Ausnutzung der längeren Relaxationszeiten von ^{13}C Kernen. Da dies in Verbindung mit der Verwendung von Metaboliten mit Hinblick auf metabolische Bildgebung besonders interessant ist, wird diese Möglichkeit weiter verfolgt.

Bibliography

[1] I. I. Rabi, J. R. Zacharias, S. Millman, and P. Kusch. A New Method of Measuring Nuclear Magnetic Moment. *Phys. Rev.*, 53:318–318, Feb 1938.

[2] E. M. Purcell, H. C. Torrey, and R. V. Pound. Resonance Absorption by Nuclear Magnetic Moments in a Solid. *Phys. Rev.*, 69:37–38, Jan 1946.

[3] F. Bloch. Nuclear Induction. *Phys. Rev.*, 70:460–474, Oct 1946.

[4] `http://www.nobelprize.org/nobel_prizes/lists/all/index.html`.

[5] Robert A. Bell. Economics of MRI technology. *Journal of Magnetic Resonance Imaging*, 6(1):10–25, 1996.

[6] `http://www.siemens.com/investor/de/finanzberichte/geschaeftsberichte.htm`.

[7] C. Russell Bowers and D. P. Weitekamp. Parahydrogen and synthesis allow dramatically enhanced nuclear alignment. *Journal of the American Chemical Society*, 109(18):5541–5542, 1987.

[8] Johannes Natterer and Joachim Bargon. Parahydrogen induced polarization. *Progress in Nuclear Magnetic Resonance Spectroscopy*, 31(4):293–315, 1997.

[9] Ralph W. Adams, Juan A. Aguilar, Kevin D. Atkinson, Michael J. Cowley, Paul I. P. Elliott, Simon B. Duckett, Gary G. R. Green, Iman G. Khazal, Joaquin Lopez-Serrano, and David C. Williamson. Reversible Interactions with para-Hydrogen Enhance NMR Sensitivity by Polarization Transfer. *Science*, 323(5922):1708–1711, 2009.

[10] R. Kaptein, K. Dijkstra, and K. Nicolay. Laser photo-CIDNP as a surface probe for proteins in solution. *Nature*, 274:293–294, 1978.

[11] J. Hore and R.W. Broadhurst. Photo-CIDNP of biopolymers. *Progress in Nuclear Magnetic Resonance Spectroscopy*, 25(4):345–402, 1993.

[12] Eugenio Daviso, Anna Diller, A. Alia, Jörg Matysik, and Gunnar Jeschke. Photo-CIDNP MAS NMR beyond the T_1 limit by fast cycles of polarization extinction and polarization generation. *Journal of Magnetic Resonance*, 190(1):43–51, 2008.

[13] Alfred Kastler. Quelques suggestions concernant la production optique et la détection optique d'une inégalité de population des niveaux de quantifigation spatiale des atomes. Application à l'expérience de Stern et Gerlach et à la résonance magnétique. *J. Phys. Radium*, 11(6):255–265, 1950.

[14] M. A. Bouchiat, T. R. Carver, and C. M. Varnum. Nuclear Polarization in ^{3}He Gas Induced by Optical Pumping and Dipolar Exchange. *Phys. Rev. Lett.*, 5:373–375, Oct 1960.

[15] Albert W. Overhauser. Polarization of Nuclei in Metals. *Phys. Rev.*, 92:411–415, Oct 1953.

[16] T. R. Carver and C. P. Slichter. Polarization of Nuclear Spins in Metals. *Phys. Rev.*, 92:212–213, Oct 1953.

[17] Thomas R. Carver and Charles P. Slichter. Experimental Verification of the Overhauser Nuclear Polarization Effect. *Phys. Rev.*, 102:975–980, May 1956.

[18] K. H. Hausser. Bestimmung der Hochfeldgrenze der dynami-schen Kernpolarisation aus der Dispersion der Kernrelaxation. *Zeitschrift für Physik A: Hadrons and Nuclei*, 183:265–273, 1965.

[19] R.A. Dwek, O.W. Howarth, D.F.S. Natusch, and R.E. Richards. Proton-electron double resonance in organic compounds. *Molecular Physics*, 13(5):457–460, 1967.

[20] Stehlik D. Hausser, K. H. Dynamic Nuclear Polarization in Liquids. *Adv. Magn. Res.*, 12:79–139, 1968.

[21] W. Müller-Warmuth and Erol Öztekin. Study of hydrogen bridge formation in free radical solutions via dynamic nuclear polarization. *Molecular Physics*, 17(1):105–107, 1969.

[22] C. D. Jeffries. Polarization of Nuclei by Resonance Saturation in Paramagnetic Crystals. *Phys. Rev.*, 106:164–165, Apr 1957.

[23] C. D. Jeffries. Dynamic Orientation of Nuclei by Forbidden Transitions in Paramagnetic Resonance. *Phys. Rev.*, 117:1056–1069, Feb 1960.

[24] Chester F. Hwang and D. A. Hill. New Effect in Dynamic Polarization. *Phys. Rev. Lett.*, 18:110–112, Jan 1967.

[25] David S. Wollan. Dynamic nuclear polarization with an inhomogeneously broadened ESR line. I. Theory. *Phys. Rev. B*, 13:3671–3685, May 1976.

[26] M. Goldman. *Spin Temperature and Nuclear Magnetic Resonance in Solids*. Clarendon Press, Oxford, 1970.

[27] R.A. Wind, M.J. Duijvestijn, C. van der Lugt, A. Manenschijn, and J. Vriend. Applications of dynamic nuclear polarization in ^{13}C NMR in solids. *Progress in Nuclear Magnetic Resonance Spectroscopy*, 17(0):33–67, 1985.

[28] R. G. Griffin and T. F. Prisner. High field dynamic nuclear polarization-the renaissance. *Phys. Chem. Chem. Phys.*, 12:5737–5740, 2010.

[29] Lino R. Becerra, Gary J. Gerfen, Richard J. Temkin, David J. Singel, and Robert G. Griffin. Dynamic nuclear polarization with a cyclotron resonance maser at 5 T. *Phys. Rev. Lett.*, 71:3561–3564, Nov 1993.

[30] G. J. Gerfen, L. R. Becerra, D. A. Hall, R. G. Griffin, R. J. Temkin, and D. J. Singel. High frequency (140 GHz) dynamic nuclear polarization: Polarization transfer to a solute in frozen aqueous solution. *The Journal of Chemical Physics*, 102(24):9494–9497, 1995.

[31] Klaes Golman, René in 't Zandt, and Mikkel Thaning. Real-time metabolic imaging. *Proceedings of the National Academy of Sciences*, 103(30):11270–11275, 2006.

[32] Changsik Song, Kan-Nian Hu, Chan-Gyu Joo, Timothy M. Swager, and Robert G. Griffin. TOTAPOL: A Biradical Polarizing Agent for Dynamic Nuclear Polarization Experiments in Aqueous Media. *Journal of the American Chemical Society*, 128(35):11385–11390, 2006.

[33] M. Reese, D. Lennartz, T. Marquardsen, P. Höfer, A. Tavernier, P. Carl, T. Schippmann, M. Bennati, T. Carlomagno, F. Engelke, and C. Griesinger. Construction of a Liquid-State NMR DNP Shuttle Spectrometer: First Experimental Results and Evaluation of Optimal Performance Characteristics. *Applied Magnetic Resonance*, 34:301–311, 2008.

[34] Simon Hu, Minhua Zhu, Hikari A.I. Yoshihara, David M. Wilson, Kayvan R. Keshari, Peter Shin, Galen Reed, Cornelius von Morze, Robert Bok, Peder E.Z. Larson, John Kurhanewicz, and Daniel B. Vigneron. In vivo measurement of normal rat intracellular pyruvate and lactate levels after injection of hyperpolarized [1-^{13}C]alanine. *Magnetic Resonance Imaging*, 29(8):1035 –1040, 2011.

[35] Peter Höfer, Giacomo Parigi, Claudio Luchinat, Patrick Carl, Gisela Guthausen, Marcel Reese, Teresa Carlomagno, Christian Griesinger, and Marina Bennati. Field Dependent Dynamic Nuclear Polarization with Radicals in Aqueous Solution. *Journal of the American Chemical Society*, 130(11):3254–3255, 2008.

[36] P. J. M. van Bentum, G. H. A. van der Heijden, J. A. Villanueva-Garibay, and A. P. M. Kentgens. Quantitative analysis of high field liquid state dynamic nuclear polarization. *Phys. Chem. Chem. Phys.*, 13:17831–17840, 2011.

[37] Eugeny V. Kryukov, Kevin J. Pike, Thomas K. Y. Tam, Mark E. Newton, Mark E. Smith, and Ray Dupree. Determination of the temperature dependence of the dynamic nuclear polarisation enhancement of water protons at 3.4 Tesla. *Phys. Chem. Chem. Phys.*, 13:4372–4380, 2011.

[38] Maria-Teresa Türke, Igor Tkach, Marcel Reese, Peter Höfer, and Marina Bennati. Optimization of dynamic nuclear polarization experiments in aqueous solution at 15 MHz/9.7 GHz: a comparative study with DNP at 140 MHz/94 GHz. *Phys. Chem. Chem. Phys.*, 12:5893–5901, 2010.

[39] M. J. Prandolini, V. P. Denysenkov, M. Gafurov, S. Lyubenova, B. Endeward, M. Bennati, and T. F. Prisner. First DNP Results from a Liquid Water-TEMPOL Sample at 400 MHz and 260 GHz. *Applied Magnetic Resonance*, 34:399–407, 2008.

[40] M J Prandolini, V P Denysenkov, M Gafurov, B Endeward, and T F Prisner. High-field dynamic nuclear polarization in aqueous solutions. *Journal of the American Chemical Society*, 131(17):6090–6092, 2009.

[41] Vasyl Denysenkov, Mark J. Prandolini, Marat Gafurov, Deniz Sezer, Burkhard Endeward, and Thomas F. Prisner. Liquid state DNP using a 260 GHz high power gyrotron. *Phys. Chem. Chem. Phys.*, 12:5786–5790, 2010.

[42] Malcolm H. Levitt. *Spin Dynamics*. John Wiley & Sons, Ltd., 2001.

[43] Anatoli Abragam. *Principles of Nuclear Magnetism*. Oxford University Press, 1961.

[44] Anatoli Abragam and Maurice Goldman. *Nuclear Magnetism: Order and Disorder*. Clarendon Press, Oxford, 1982.

[45] A Abragam and M Goldman. Principles of dynamic nuclear polarisation. *Reports on Progress in Physics*, 41(3):395, 1978.

[46] Arthur Schweiger and Gunnar Jeschke. *Principles of Pulse Electron Paramagnetic Resonance*. Oxford University Press, 2001.

[47] Tao Wu, Kurtis R. Kendell, Joel P. Felmlee, Bradley D. Lewis, and Richard L. Ehman. Reliability of water proton chemical shift temperature calibration for focused ultrasound ablation therapy. *Medical Physics*, 27(1):221–224, 2000.

[48] I. Solomon. Relaxation Processes in a System of Two Spins. *Phys. Rev.*, 99:559–565, Jul 1955.

[49] James S. Hyde, James C. W. Chien, and Jack H. Freed. Electron-Electron Double Resonance of Free Radicals in Solution. *The Journal of Chemical Physics*, 48(9):4211–4226, 1968.

[50] Jack H. Freed. Theory of saturation and double resonance effects in electron spin resonance spectra. II. Exchange vs. dipolar mechanisms. *The Journal of Physical Chemistry*, 71(1):38–51, 1967.

[51] Maria-Teresa Türke and Marina Bennati. Saturation factor of nitroxide radicals in liquid DNP by pulsed ELDOR experiments. *Phys. Chem. Chem. Phys.*, 13:3630–3633, 2011.

[52] Babul Borah and Robert G. Bryant. NMR relaxation dispersion in an aqueous nitroxide system. *The Journal of Chemical Physics*, 75(7):3297–3300, 1981.

[53] Claudio Luchinat and Giacomo Parigi. Collective Relaxation of Protein Protons at Very Low Magnetic Field: A New Window on Protein Dynamics and Aggregation. *Journal of the American Chemical Society*, 129(5):1055–1064, 2007.

[54] C. Luchinat and G. Parigi. Nuclear Relaxometry Helps Designing Systems for Solution DNP on Proteins. *Applied Magnetic Resonance*, 34:379–392, 2008.

[55] Werner Müller-Warmuth and Karin Meise-Gresch. Molecular Motions and Interactions as Studied by Dynamic Nuclear Polarization (DNP) in Free Radical Solutions. *Adv. Magn. Res.*, 11:1–45, 1983.

[56] Deniz Sezer, M. J. Prandolini, and Thomas F. Prisner. Dynamic nuclear polarization coupling factors calculated from molecular dynamics simulations of a nitroxide radical in water. *Phys. Chem. Chem. Phys.*, 11:6626–6637, 2009.

[57] Y. Ayant, E. Belorizky, J. Aluzon, and J. Gallice. Calcul des densités spectrales résultant d'un mouvement aléatoire de translation en relaxation par interaction dipolaire magnétique dans les liquides. *J. Phys. France*, 36:991–1004, 1975.

[58] W. T. Wenckebach. The Solid Effect. *Applied Magnetic Resonance*, 34:227–235, 2008.

[59] A Abragam and M Goldman. Principles of dynamic nuclear polarisation. *Reports on Progress in Physics*, 41(3):395, 1978.

[60] Kan-Nian Hu, Hsiao-hua Yu, Timothy M. Swager, and Robert G. Griffin. Dynamic Nuclear Polarization with Biradicals. *Journal of the American Chemical Society*, 126(35):10844–10845, 2004.

[61] Thorsten Maly, Galia T. Debelouchina, Vikram S. Bajaj, Kan-Nian Hu, Chan-Gyu Joo, Melody L. MakJurkauskas, Jagadishwar R. Sirigiri, Patrick C. A. van der Wel, Judith Herzfeld, Richard J. Temkin, and Robert G. Griffin. Dynamic nuclear polarization at high magnetic fields. *The Journal of Chemical Physics*, 128(5):052211, 2008.

[62] C. T. Farrar, D. A. Hall, G. J. Gerfen, S. J. Inati, and R. G. Griffin. Mechanism of dynamic nuclear polarization in high magnetic fields. *The Journal of Chemical Physics*, 114(11):4922–4933, 2001.

[63] V. P. Denysenkov, M. J. Prandolini, A. Krahn, M. Gafurov, B. Endeward, and T. F. Prisner. High-Field DNP Spectrometer for Liquids. *Applied Magnetic Resonance*, 34:289–299, 2008.

[64] Roy E. Hoffman. Standardization of chemical shifts of TMS and solvent signals in NMR solvents. *Magnetic Resonance in Chemistry*, 44(6):606–616, 2006.

[65] Roy E. Hoffman. Measurement of magnetic susceptibility and calculation of shape factor of NMR samples. *Journal of Magnetic Resonance*, 178(2):237 – 247, 2006.

[66] J. A. Riddick, W. B. Bunger, and T. K. Sakano. *Techniques of Chemistry. Vol. II, Organic Solvents*. Wiley, 1986.

[67] Bruker Almanac 2012.

[68] Malgorzata Marjanska, Isabelle Iltis, Alexander A. Shestov, Dinesh K. Deelchand, Christopher Nelson, Kamil Ugurbil, and Pierre-Gilles Henry. In vivo ^{13}C spectroscopy in the rat brain using hyperpolarized [1-^{13}C]pyruvate and [2-^{13}C]pyruvate. *Journal of Magnetic Resonance*, 206(2):210–218, 2010.

[69] Mark J. Albers, Robert Bok, Albert P. Chen, Charles H. Cunningham, Matt L. Zierhut, Vickie Yi Zhang, Susan J. Kohler, James Tropp, Ralph E. Hurd, Yi-Fen Yen, Sarah J. Nelson, Daniel B. Vigneron, and John Kurhanewicz. Hyperpolarized ^{13}C Lactate, Pyruvate, and Alanine: Noninvasive Biomarkers for Prostate Cancer Detection and Grading. *Cancer Research*, 68(20):8607–8615, 2008.

[70] Jan G. Krummenacker, Vasyl P. Denysenkov, and Thomas F. Prisner. Liquid State DNP on Metabolites at 260 GHz EPR/400 MHz NMR Frequency. *Applied Magnetic Resonance*, 43:139–146, 2012. 10.1007/s00723-012-0351-8.

[71] K. Tsai and H. Dorn. A model for establishing the ultimate enhancements (A_∞) in the low to high magnetic field transfer dynamic nuclear polarization experiment. *Applied Magnetic Resonance*, 1:231–254, 1990. 10.1007/BF03166157.

[72] Karl-Heinz Herrmann, Andreas Pohlmeier, Daniel Gembris, and Harry Vereecken. Three-dimensional imaging of pore water diffusion and motion in porous media by nuclear magnetic resonance imaging. *Journal of Hydrology*, 267(3-4):244–257, 2002.

[73] Paul Delahay. Theory of Kinetic Polarographic Currents and Conversion of Rate Constants. *Journal of the American Chemical Society*, 74(14):3506–3508, 1952.

[74] Brandon D. Armstrong and Songi Han. Overhauser Dynamic Nuclear Polarization To Study Local Water Dynamics. *Journal of the American Chemical Society*, 131(13):4641–4647, 2009.

[75] Mathias Haake, Johannes Natterer, and Joachim Bargon. Efficient NMR Pulse Sequences to Transfer the Parahydrogen-Induced Polarization to Hetero Nuclei. *Journal of the American Chemical Society*, 118(36):8688–8691, 1996.

[76] M. S. Albert, G. D. Cates, B. Driehuys, W. Happer, B. Saam, C. S. Springer, and Wishnia A. Biological magnetic resonance imaging using laser-polarized ^{129}Xe. *Nature*, 370:199–201, 1994.

[77] Hunter Middleton, Robert D. Black, Brian Saam, Gordon D. Cates, Gary P. Cofer, Robert Guenther, William Happer, Lawrence W. Hedlund, G. Alan Johnson, Kim Juvan, and John Swartz. MR Imaging with Hyperpolarized ^{3}He Gas. *Magnetic Resonance in Medicine*, 33(2):271–275, 1995.

[78] W. Happer, E. Miron, S. Schaefer, D. Schreiber, W. A. van Wijngaarden, and X. Zeng. Polarization of the nuclear spins of noble-gas atoms by spin exchange with optically pumped alkali-metal atoms. *Phys. Rev. A*, 29:3092–3110, Jun 1984.

[79] F. D. Colegrove, L. D. Schearer, and G. K. Walters. Polarization of He^3 Gas by Optical Pumping. *Phys. Rev.*, 132:2561–2572, Dec 1963.

[80] Peter Bachert, Lothar R. Schad, Michael Bock, Michael V. Knopp, Michael Ebert, Tino Grobmann, Werner Heil, Dirk Hofmann, Reinhard Surkau, and Ernst W. Otten. Nuclear magnetic resonance imaging of airways in humans with use of hyperpolarized ^{3}He. *Magnetic Resonance in Medicine*, 36(2):192–196, 1996.

[81] M. Batz, S. Baessler, W. Heil, E. W. Otten, D. Rudersdorf, J. Schmiedeskamp, Y. Sobolev, and M. Wolf. ^{3}He Spin Filter for Neutrons. *Journal of Research of the National Institute of Standards and Technology*, 110:293–298, 2005.

[82] N. R. Newbury, A. S. Barton, G. D. Cates, W. Happer, and H. Middleton. Gaseous ^{3}He $-^3$ He magnetic dipolar spin relaxation. *Phys. Rev. A*, 48:4411–4420, Dec 1993.

[83] M. Gatzke, G. D. Cates, B. Driehuys, D. Fox, W. Happer, and B. Saam. Extraordinarily slow nuclear spin relaxation in frozen laser-polarized ^{129}Xe. *Phys. Rev. Lett.*, 70:690–693, Feb 1993.

[84] Ruiliang Wang, Gene-Jack Wang, Rita Z. Goldstein, Elisabeth C. Caparelli, Nora D. Volkow, Joanna S. Fowler, and Dardo Tomasi. Induced

magnetic force in human heads exposed to 4 T MRI. *Journal of Magnetic Resonance Imaging*, 31(4):815–820, 2010.

[85] P.M. Glover, I. Cavin, W. Qian, R. Bowtell, and P.A. Gowland. Magnetic-field-induced vertigo: A theoretical and experimental investigation. *Bioelectromagnetics*, 28(5):349–361, 2007.

[86] Christian Hilty, Erin E. McDonnell, Josef Granwehr, Kimberly L. Pierce, Song-I Han, and Alexander Pines. Microfluidic gas-flow profiling using remote-detection NMR. *Proceedings of the National Academy of Sciences of the United States of America*, 102(42):14960–14963, 2005.

[87] Jan H. Ardenkjaer-Larsen, Bjoern Fridlund, Andreas Gram, Georg Hansson, Lennart Hansson, Mathilde H. Lerche, Rolf Servin, Mikkel Thaning, and Klaes Golman. Increase in signal-to-noise ratio of > 10,000 times in liquid-state NMR. *Proceedings of the National Academy of Sciences*, 100(18):10158–10163, 2003.

[88] Evan R. McCarney, Brandon D. Armstrong, Mark D. Lingwood, and Songi Han. Hyperpolarized water as an authentic magnetic resonance imaging contrast agent. *Proceedings of the National Academy of Sciences*, 104(6):1754–1759, 2007.

[89] Talia Harris, Galit Eliyahu, Lucio Frydman, and Hadassa Degani. Kinetics of Hyperpolarized ^{13}C-Pyruvate Transport and Metabolism in Living Human Breast Cancer Cells. *Proceedings of the National Academy of Sciences of the United States of America*, 106(43):18131–18136, 2009.

[90] A. Comment, B. van den Brandt, K. Uffmann, F. Kurdzesau, S. Jannin, J.A. Konter, P. Hautle, W.Th. Wenckebach, R. Gruetter, and J.J. van der Klink. Design and performance of a DNP prepolarizer coupled to a rodent MRI scanner. *Concepts in Magnetic Resonance Part B: Magnetic Resonance Engineering*, 31B(4):255–269, 2007.

[91] A. Comment, B. van den Brandt, K. Uffmann, F. Kurdzesau, S. Jannin, J. A. Konter, P. Hautle, W. T. Wenckebach, R. Gruetter, and J. J. van der Klink. Principles of Operation of a DNP Prepolarizer Coupled to a Rodent MRI Scanner. *Applied Magnetic Resonance*, 34(3-4):313–319, 2008.

[92] A. Comment, J. Rentsch, F. Kurdzesau, S. Jannin, K. Uffmann, R. B. van Heeswijk, P. Hautle, J. A. Konter, B. van den Brandt, and J. J.

van der Klink. Producing over 100 ml of highly concentrated hyperpolarized solution by means of dissolution DNP. *Journal Of Magnetic Resonance*, 194:152–155, 2008.

[93] S. J. Nelson, D. Vigneron, J. Kurhanewicz, A. Chen, R. Bok, and R. Hurd. DNP-Hyperpolarized ^{13}C Magnetic Resonance Metabolic Imaging for Cancer Applications. *Applied Magnetic Resonance*, 34:533–544, 2008.

[94] K. Münnemann, C. Bauer, J. Schmiedeskamp, H. W. Spiess, W. G. Schreiber, and D. Hinderberger. A Mobile DNP Polarizer for Clinical Applications. *Applied Magnetic Resonance*, 34:321–330, 2008. 10.1007/s00723-008-0130-8.

[95] Mark D. Lingwood, Ting Ann Siaw, Napapon Sailasuta, Brian D. Ross, Pratip Bhattacharya, and Songi Han. Continuous flow Overhauser dynamic nuclear polarization of water in the fringe field of a clinical magnetic resonance imaging system for authentic image contrast. *Journal of Magnetic Resonance*, 205(2):247–254, 2010.

[96] K. Miesel, K. L. Ivanov, T. Köchling, A. V. Yurkovskaya, and H.-M. Vieth. Field-Cycling Effects on Dynamic Nuclear Polarization. *Applied Magnetic Resonance*, 34:423–437, 2008. 10.1007/s00723-008-0126-4.

[97] patent pending DE 102010017568.

[98] patent pending WO 2011160853.

[99] Jan G. Krummenacker, Vasyl P. Denysenkov, Maxim Terekhov, Laura M. Schreiber, and Thomas F. Prisner. DNP in MRI: An in-bore approach at 1.5 T. *Journal of Magnetic Resonance*, 215(0):94–99, 2012.

[100] Technical Manual Siemens Sonata 1.5 T.

[101] Robert E. Collin. *Foundations for Microwave Engineering*. McGraw-Hill, 1992.

[102] P.T. Callaghan. *Principles of Nuclear Magnetic Resonance Microscopy*. Clarendon Press, Oxford, 1991.

[103] Mark D. Lingwood, Andrew J. Sederman, Mick D. Mantle, Lynn F. Gladden, and Songi Han. Overhauser dynamic nuclear polarization amplification of NMR flow imaging. *Journal of Magnetic Resonance*, 216(0):94 – 100, 2012.

[104] H.C Dorn, J Wang, L Allen, D Sweeney, and T.E Glass. Flow dynamic nuclear polarization, a novel method for enhancing NMR signals in flowing fluids. *Journal of Magnetic Resonance (1969)*, 79(3):404–412, 1988.

[105] R. Gitti, C. Wild, C. Tsiao, K. Zimmer, T. E. Glass, and Harry C. Dorn. Solid/liquid intermolecular transfer of dynamic nuclear polarization. Enhanced flowing fluid proton NMR signals via immobilized spin labels. *Journal of the American Chemical Society*, 110(7):2294–2296, 1988.

[106] H.C. Dorn, R. Gitti, K.H. Tsai, and T.E. Glass. The flow transfer of a bolus with ^{1}H dynamic nuclear polarization from low to high magnetic fields. *Chemical Physics Letters*, 155(2):227–232, 1989.

[107] H. Dorn, T. Glass, R. Gitti, and K. Tsai. Transfer of ^{1}H and ^{13}C dynamic nuclear polarization from immobilized nitroxide radicals to flowing liquids. *Applied Magnetic Resonance*, 2:9–27, 1991. 10.1007/BF03166265.

[108] S. Stevenson and H. C. Dorn. ^{13}C Dynamic Nuclear Polarization: A Detector for Continuous-Flow, Online Chromatography. *Analytical Chemistry*, 66(19):2993–2999, 1994.

[109] J. H. Simpson and H. Y. Carr. Diffusion and Nuclear Spin Relaxation in Water. *Phys. Rev.*, 111:1201–1202, Sep 1958.

[110] Talia Harris, Christian Bretschneider, and Lucio Frydman. Dissolution DNP NMR with solvent mixtures: Substrate concentration and radical extraction. *Journal of Magnetic Resonance*, 211(1):96–100, 2011.

[111] W.R. Couet, R.C. Brasch, G. Sosnovsky, and T.N. Tozer. Factors affecting nitroxide reduction in ascorbate solution and tissue homogenates. *Magnetic Resonance Imaging*, 3(1):83–88, 1985.

[112] W.R. Couet, R.C. Brasch, C. Sosnovsky, J. Lukszo, I. Prakash, C.T. Gnewech, and T.N. Tozer. Influerce of chemical structure of nitroxyl spin labels on their reduction by ascorbic acid. *Tetrahedron*, 41(7):1165–1172, 1985.

[113] N. Kocherginsky and HM Swartz. *Nitroxide spin labels: Reactions in biology and chemistry*. CRC Press, Boca Raton, 1995.

[114] Marina Kveder, Greta Pifat, Slavko Pecar, Milan Schara, Pilar Ramos, and Hermann Esterbauer. Nitroxide reduction with ascorbic acid in spin labeled human plasma LDL and VLDL. *Chemistry and Physics of Lipids*, 85(1):1–12, 1997.

[115] Marina Carravetta, Ole G. Johannessen, and Malcolm H. Levitt. Beyond the T_1 Limit: Singlet Nuclear Spin States in Low Magnetic Fields. *Phys. Rev. Lett.*, 92:153003, Apr 2004.

[116] Marina Carravetta and Malcolm H. Levitt. Long-Lived Nuclear Spin States in High-Field Solution NMR. *Journal of the American Chemical Society*, 126(20):6228–6229, 2004. PMID: 15149209.

[117] Giuseppe Pileio, Marina Carravetta, Eric Hughes, and Malcolm H. Levitt. The Long-Lived Nuclear Singlet State of ^{15}N-Nitrous Oxide in Solution. *Journal of the American Chemical Society*, 130(38):12582–12583, 2008.

Acknowledgments

I am deeply indebted to **Prof. Thomas Prisner** and **Prof. Laura Schreiber** for launching this project, giving me the opportunity to work on it and supporting me all the way through. I was given plenty of freedom on my approach and I greatly appreciate that. I profited a great deal from their scientific input.
In particular Thomas' feedback in many DNP related discussions was extremely valuable, as well as his profound knowledge of the subject.

I would like to express my gratitude to **Vasyl Denysenkov**, who contributed immensely to this project. His guidance, help and advice are priceless, from hardware to manuscripts. Vasyl contributed to the correction of this manuscript as well.
I would like to thank **Petr Neugebauer**, with whom I spent countless hours in the underground NMR facilities, running the DNP spectrometer and the gyrotron. He also contributed to the correction of this thesis.

I would like to acknowledge the "DNP subgroup" of the Prisner workgroup. Its weekly meetings have been the frame for many fruitful - and at times very lively - discussions. Beside the members already mentioned above, they are namely:
Burkhard Endeward introduced me to our Q-band spectrometer, which I took my first steps with. As well, his support, help and of course contributions in numerous discussions is acknowledged.
Marat Gafurov and **Mark Prandolini** were the driving force behind our high field DNP project during the early stages of my project. They introduced me to the high field DNP spectrometer and provided help and advice many times. All of their input is greatly appreciated.
Sevdalina Lyubenova is acknowledged not only for her scientific input, but also for being such a great office mate and friend.
I would like to thank **Deniz Sezer**, who performed the MD studies mentioned in this thesis, for his contribution, in particular for the discussions he

sparked and fueled throughout his time with us.

Ivan Krstić and **Philipp Spindler** are thanked for their help and corrections of this thesis, **Jörn Plackmeyer** for all his chemical expertise that he was always happy to share.
Bernhard Thiem in thanked for the technical support he provided, in particular with the power supply and the control of the 42 GHz source.
Also, I would like to thank all Prisner workgroup members not mentioned before for providing the work environment that made this work possible: **Charlotte Börner**, **Reza Dastvan**, **Claudia Grytz**, **Haleh Haeri**, **Sigrid Kämmerer**, **Bisera Krstić**, **Dominik Margraf**, **Andriy Marko** and **Denise Schütz**.

Concordantly, I found a good working atmosphere in the Schreiber group at the Johannes Gutenberg University Medical Center in Mainz. I am thankful to **Maxim Terekhov** for all the effort he put into our project and all the help he provided. It was a pleasure - and very fruitful as well - to work with him. Maxim contributed to the correction of this thesis as well.
Also, I would like to thank **Kathrin Gerz** for her contribution to this project, as well as the wonderfully illuminated flat cell photo.
Falk Dechent, **Dirk Graafen** and **Julien Rivoire** are acknowledged for their help with first tests on the tomograph. Additionally, I would like to thank Julien for having me in his ^{3}He lung study and providing me with the wonderful images.
Stefan Fischer is thanked for his technical support, for putting up with "my" DNP equipment in "his" lab and loaning his tools. He also introduced me to the smelly but wonderfully efficient ACRIFIX® glue.
I am indebted to **Mrs. Dieringer** in the administrative staff in Mainz for her friendly support and for helping me working out the problems with my contract so well.

The **mechanical workshop** in Frankfurt did an outstanding job, especially on machining the fine structures of the microwave equipment that was built. Their exemplary work is a keystone of making this project work.

I would like to thank **Johanna Baldus** (AK Glaubitz) for all her support with the NMR spectrometer and its periphery. She saved Petr and me a great deal of time and stress.

Doris Ceglarek and **Robert Heide** (AK Terfort) are acknowledged for the help and advice with the silver coating of the resonator and the SEM

pictures.

I would like to thank **Tobias Lehnert**, **Karsten Schwarz** and **Katrin Wirtz** who contributed to the correction of this thesis.

Frank Löhr and **Christian Richter** (BMRZ) are acknowledged for their support with the relaxivity measurements at various fields and temperatures.

Ilja Müller (Institut für angewandte Physik, Frankfurt) is thanked for his help with repairing our gyrotron high voltage power supply. His exemplary helpfulness brought us back on track as fast as possible.

I would like to thank **Kerstin Münnemann** (MPI Mainz) for her effort in planning this project and of course her support and help in the early stages of the DFG application and the patent filing process.

Giacomo Parigi (CERN, Florence, Italy) is acknowledged for providing the NMRD data presented in this work.

Manfred Strupf (BMRZ) is acknowledged for his helpfulness and technical support in the NMR lab.

Funding of this project was provided by the **Deutsche Forschungsgemeinschaft** (DFG), the **European Commission** (EU Design Study BioDNP) and the **Biomolecular Magnetic Resonance Center** (BMRZ) in Frankfurt. Travel grants were generously provided by the **COST P15** program.